UNIVERSITÀ DEGLI STUDI DI ROMA "TOR VERGATA"

FACOLTA' DI INGEGNERIA

DOTTORATO DI RICERCA IN
ELETTRONICA QUANTISTICA E PLASMI

CICLO DEL CORSO DI DOTTORATO. XXI

Laser-induced plasma underwater: spectroscopic applications, enhancement of the emission and bubble cavitation

Violeta Lazic

Docente Guida/Tutor: Prof. Maria Richetta

Coordinatore: Prof. Carlo Bellecci

2008

Table of contents

Chapter 1

INTRODUCTION

Laser-induced plasma in liquids exhibits a number of important effects beside the luminous emission, among them there are: cavitation bubble formation, bubble collapse, generation of the shock waves and acoustics waves [1]. In the past decades, an extended research has been performed relative to the laser-induced plasma formation and its effects in liquids, mainly motivated by the medical laser applications, such as ophthalmic laser surgery, tissue cutting, laser angioplasty, laser lithotripsy etc. [1-2]. A number of the industrial applications have been also developed concerning the laser-processing in liquids through the plasma formation, including: wet etching and cutting, then welding, cladding, cleaning, laser shock peening and deposition of thin films [3]. Laser ablation of a solid target in a confining liquid provides an effective means to synthesize nanoparticles, especially for the metastable nanocrystals such as diamond and carbon related materials, immiscible alloys, etc [4]. On the other hand, the gas bubble produced by the laser formed breakdown in liquids (in absence of solid material ablation) might experience a quasi symmetrical collapse [5]. The final phase of the bubble compression leads to generation of extremely high local temperatures and pressures [1, 5-7]. This process is accompanied by a burst light emission called sonoluminescence [5-7]. The extreme conditions present at a moment of the maximum bubble compression can be also exploited for synthesis of new types of nanomaterials and biomaterials [8], as well as for treatments of the waste waters [9]. These processes were mainly studied for the gas bubbles in liquids produced by ultrasonic waves. However, the bubbles with analogue properties can be also produced after laser-induced breakdown in liquids [7], but in such case the cavitation can be controlled better than in the case of ultrasonic excitation [5, 7].

One of the emerging applications of the laser formed plasma in liquids is Laser Induced Breakdown Spectroscopy – LIBS (Chapter 2), where the spectral emission of the plasma is exploited for elemental sample analysis. LIBS applications for analyses of different materials in gas surrounding or vacuum have been studied and developed in the last two decades. A very few papers report such analyses underwater, which regard liquid impurities or immersed solid samples with flat surface only.

One of the main characteristics of laser-induced plasma inside liquids is fast quenching due to a dense medium (Chapter 3). This short-living, high density plasma has a relatively weak spectral emission with extremely broadened lines, thus limiting a possibility of LIBS detection only to main sample (liquids or immersed solids) constituents. These limits had been partially overcome by applying a Double-Pulse (DP) laser excitation. In this case the first pulse creates a gas bubble, which represents a less dense medium before applying the second (analytical) laser pulse. In this way, the LIBS detection limits were generally reduced to an order of magnitude of 1-10 ppm, except for alkali elements, for which some better sensibility was achieved.

This dissertation covers an extended field of research relative to underwater laser-induced plasmas, mainly aimed to its spectroscopic applications, and includes:

1) LIBS studies of immersed solid materials, both with flat and rough surfaces (Chapter 4)
2) Data processing for manifold LIBS signal increase in presence of important signal oscillations, which appear in underwater plasmas and/or during measurements on rough surfaces also in other surroundings (Chapter 5)
3) LIBS analyzes of soft materials underwater (Chapter 6), reported for the first time
4) LIBS spectroscopy for bulk water analyses (Chapter 7)
5) Studies of different laser excitation conditions applied on bulk liquids, and their consequences on the plasma and inherent gas bubble formation (Chapter 8)

In all here reported experiments, a single laser source was used. Double pulses are obtained by applying two external Q-Switch (QS) triggers, during a single lamp flashing. A multi-pulse sequence was also tested and it was obtained by reducing the first QS trigger delay. In this way, the first QS aperture corresponds to a low population inversion, giving rise to the relaxation oscillations. Transformation of these oscillations to the output multi-pulse sequence was made by employing KDP* crystal inside the QS . This crystal is known to exhibit a piezo-voltaic effect, responsible for periodically incomplete attenuation after the QS [10].

Contents of the present dissertation is a result of about three years work conducted at ENEA Frascati, group FIS-LAS. These studies were funded by different funded projects: TECSIS – dealing also with in-situ analyses of materials inside marine archaeological park; MIAO and

PANDORA (points 2-5) – related to studies of the prototype instruments, including LIBS, for exploration of subglacial lakes, also in Antarctica.

The results of here described research were presented at next international conferences: LIBS 2004 (Malaga, Spain), EMSLIBS 2005 (Aachen, Germany), PACIFICHEM 2005 (Honolulu, USA) and LIBS 2006 (Montreal, Canada). They leaded to the following publications:

- V. Lazic, , F. Colao, R. Fantoni and V. Spizzicchino, Recognition of archaeological materials underwater by laser induced breakdown spectroscopy, Spectrochim. Acta Part B 60 (2005) 1014-1024.
- V. Lazic, F. Colao, R. Fantoni and V. Spizzicchino, Laser-induced breakdown spectroscopy in water: Improvement of the detection threshold by signal processing, Spectrochim. Acta Part B 60 (2005) 1002-1013.
- V. Lazic, F. Colao, R. Fantoni, V. Spizzichino, S. Jovićević, Underwater sediment analyses by laser induced breakdown spectroscopy and calibration procedure for fluctuating plasma parameters, Spectrochim. Acta Part B 62 (2007) 30-39.
- V. Lazic, S. Jovicevic, R. Fantoni, F. Colao, Efficient plasma and bubble generation underwater by an optimized laser excitation and its application for liquid analyses by laser-induced breakdown spectroscopy, Spectrochim. Acta Part B 62 (2007) 1433-1442.

A part of the results published in the last paper from above, and some other not discussed in the present dissertation, are included into the next patent requested:

“Metodo laser per una produzione efficiente del plasma e delle onde d’urto nei liquidi” (laser method for efficient plasma and shock wave generation in liquids), request B02006A000755.

1.1 References

[1] P. K. Kennedy, D. X. Hammer, B. A. Rockwell, Laser-induced breakdown in aqueous media, Prog. Quant. Electr. 21, (1997) 155-248.

[2] F. Javier Gonzalez, Applied Laser Medicine, Hans-Peter Berlien and Gerhard J. Müller, eds. Springer-Verlag, Berlin, Heidelberg, New York, 2003.

[3] A. Kruusing, HANDBOOK OF LIQUIDS-ASSISTED LASER PROCESSING, Elsevier 2007.

[4] G.W. Yang, Laser ablation in liquids: Applications in the synthesis of nanocrystals, Progress in Materials Science 52 (2007) 648–698.

[5] C. D. Ohl, O. Lindau, W. Lauterborn, Luminescence from spherically and aspherically collapsing laser induced bubbles, Phys. Rev. Lett. 80 (1998) 393-396.

[6] D. Lohse, Sonoluminescence: inside a microreactor, Nature 418 (2002) 381-383.

[7] O. Baghdassarian, B. Tabbert, G. A. Williams, Luminescence Characteristics of Laser-Induced Bubbles in Water, Phys. Rev. Lett. 83 (1999) 2437- 2440.

[8] K. S. Suslick, G. J. Price, Applications of ultrasound to material chemistry, Annu. Rev. Mater. Sci. 29 (1999) 295–326.

[9] P. R. Gogate, Cavitation: an auxiliary technique in wastewater treatment schemes, Adv. Environment. Res. 6 (2002) 335-358.

[10] W. Koechner, Solid-State Laser Engineering, Springer (6th Rev 2006).

Chapter 2

LASER INDUCED BREAKDOWN SPECTROSCOPY (LIBS)

Abstract
Principles of LIBS technique are given together with its advantages and limitations. The LIBS instruments with their principal components and typical configurations are also reported. The main characteristics of the laser-produced plasma and the methods for obtaining the information about the sample from the spectrally resolved plasma emission, is discussed.

2.1 Principles of LIBS

LIBS technique [1] is a powerful tool for in-situ elemental measurements in different surroundings such as vacuum, then gas and liquids at different ambient pressures. The technique is based on plasma generation by an intense laser pulse, which duration is in nanosecond range or shorter. When analyzing the gasses or bulk liquids, the laser pulse generates a breakdown in the media. In the case of solid samples, the plasma is produced through laser-induced evaporation of the surface layer [2]. In both the cases, the intense laser pulse is also responsible for atomization and ionization of the material.

The plasma growth and decay leads to different processes such as: expansion; shock waves formation; continuum (bremsstrahlung) emission and light absorption by free electrons (inverse bremsstrahlung); collisions in the gas with excitation and relaxation of atoms/ions; chemical recombination and, as important for LIBS, de-excitation of the species (atoms, ions and molecules) through optical emission. Detection of the latter emission, obtained after laser-induced plasma formation, is a principle of LIBS technique. This radiation is usually detected in the spectral range covering near UV, visible and near IR.

Initially, the plasma temperature is very high, typically above 15 000 K, and its radiation is dominated by the continuum component (Fig. 2.1) due to bremsstrahlung emission from free electrons and ion-electron recombination [3]. The continuum emission intensity is higher for the measurements in more dense medium (high gas pressure or inside liquids), and has a relatively fast decay. It is followed by appearance of the ionic and atomic lines, where the ionic lines are more intense in the early plasma stage characterized with a high temperature. Due to a denser electron cloud in the early plasma, the emission lines are strongly collisionaly broadened thus preventing to resolve many of them. Often, the progressively decaying plasma emission can be still detected after few tens of microseconds from the laser pulse. In sufficiently cooled plasma, the emission from the molecules, formed from the species initially present in the plasma, can be also detected. Some molecules or fragments such as CN and C_2, can be observed also for the shorter acquisition delays. In order to avoid that the initial strong continuum masks emission lines, and/or that the strong initially broadened lines cover the weaker lines, it is preferable to delay the spectral acquisition with respect to the laser pulses. The acquisition gate and delay in certain experimental conditions can be optimized for obtaining maximum Signal-to-Noise Ratio (SNR) for a range of the analytical lines [4-5].

The atomic and ionic lines, once assigned to specific transitions given in databases [6-7], allow for a qualitative identification of the species present in plasma and consequently of the elements initially present in the sample (section 2.4). The relative intensities of the emission lines can be used for quantitative determination of the corresponding elements (see section 2.5).

A growing interest in LIBS technique and its rapid development in the past two decades can be attributed to its numerous advantages such as:

- Possibility to perform in-situ measurements with minimum or none sample preparation, and in different surroundings
- Theoretically, all the elements could be contemporary analyzed, both in traces and for the concentrations up to 100%. Development the of a wide range, high-resolution spectrometers allowed to capture the whole spectra necessary for the sample characterization, which often can be obtained by applying even a single laser shot
- The technique is essentially non destructive i.e. micro-destructive: as for example, ablation of less than one microgram of the sample could be sufficient for the analysis.
- The measurements can be applied both for a single point analyses and for the extended surface mapping
- Through the material removal rate (typically less than 1 μm per pulse) it is possible to measure the vertical element distributions in a small scale. Laser ablation can be used also for removal of the unwanted surface layers prior to the analyses.
- The instrument needs only an optical access to the sample, which does not induce the sample contamination, and it is possible to implement the measurements also in hostile environments.
- Data analyses can be completely automatic and the instrument can be implemented for on-line analyses
- The cost of the instrumentation is relatively low and it is possible to achieve the system miniaturization
- Using an UV laser excitation, the system could be easily switched from LIBS to LIF (Laser Induced Fluorescence) measurements, the latter are important for biological studies.

A wide range of LIBS applications has been developed in recent period [1, 8-9], including: monitoring of environmental contaminations (soils, water, aerosols and biological tissues), control of material processing - particularly developed for steel industry, sorting of materials, monitoring of traditional and nuclear power plants, detection of explosives [10] and other hazardous materials, characterization of archaeological materials and artworks [11] etc. Recently, LIBS instruments have been also proposed for planetary exploration [5, 12-13].

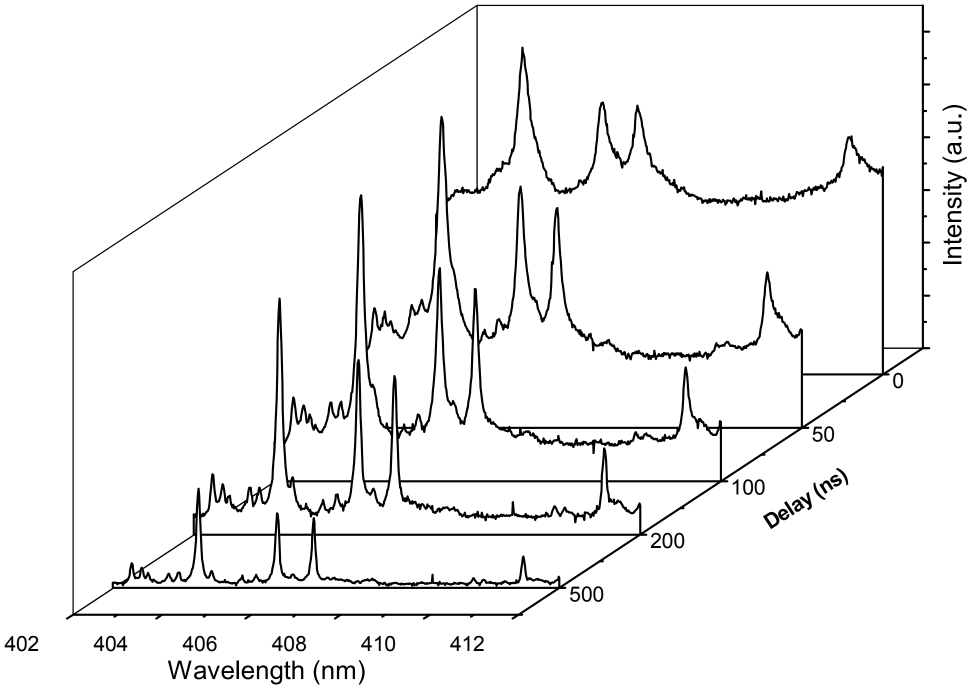

Figure 2.1: Example of LIBS spectra from stainless steel as a function of acquisition delay from the laser pulse. The signal acquisition gate is 50 ns.

2.2 Instrumentation

A typical LIBS apparatus is shown schematically in Fig. 2.2, and its main components are:

- Pulsed laser that generates plasma
- Focusing optics for the laser beam
- Sample holder (if used)
- Optical system for collecting the plasma emission and for transporting it to a spectrometer entrance. It can contain lenses, mirrors and fibre optic.
- Spectrometer for light dispersion, equipped with a detector – usually a CCD device is used without or with an intensifier (ICCD).

- Computer and electronics for triggering the laser, synchronization with the detector, eventual gating of the detector (for ICCD), then for the data acquisition and storage.

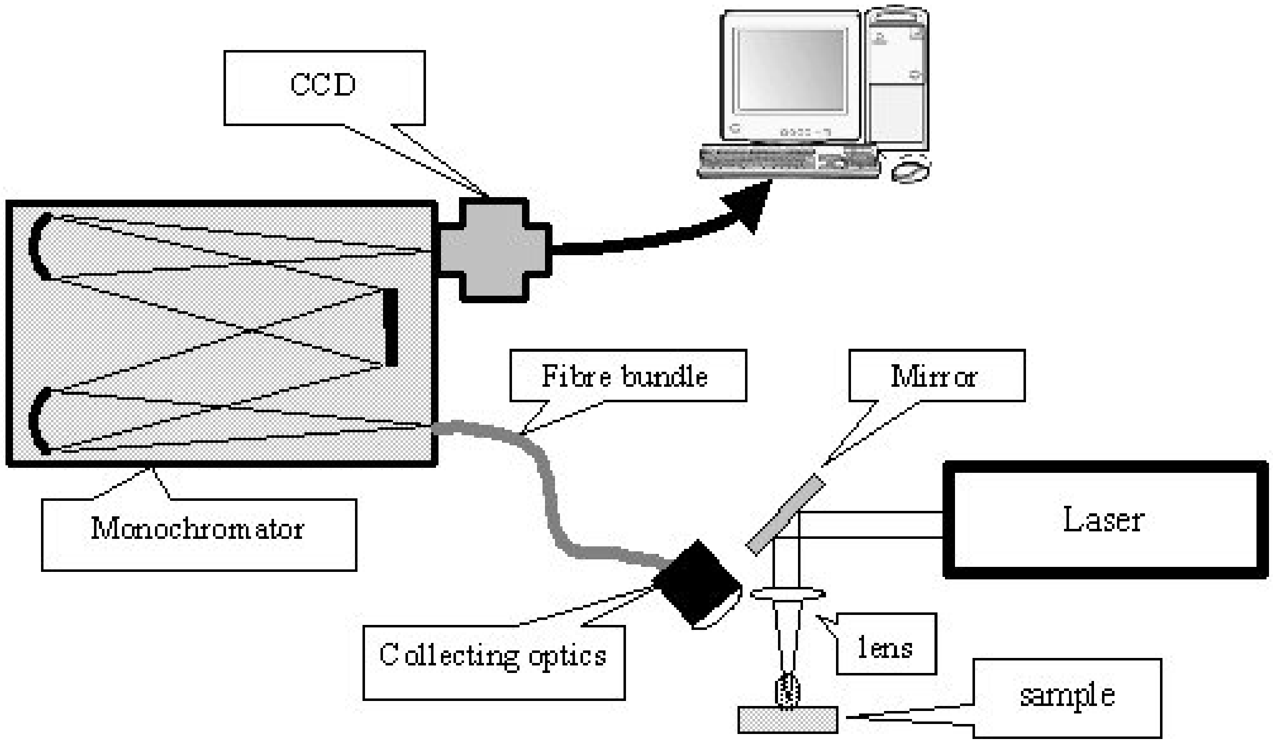

Figure 2.2: A common LIBS lay-out: bi-axial configuration

2.2.1 Lasers

For LIBS it is necessary to apply laser pulses with a high peak power, typically of 5 MW or more. Such a peak power can be obtained with moderate laser pulse energies (in order of 1 mJ) which have duration in nanosecond range. More efficient plasma generation is obtained with shorter pulses, as for example of femtosecond duration. However, the complexity and costs of femtosecond lasers make them less attractive for in-field applications.

Monochromacity of the laser source for LIBS is not critical. Regarding the laser wavelength choice, the following considerations must be taken into account:

- Sample absorption at a given laser wavelength.
- The surrounding medium should be transparent for the laser radiation: for example in underwater analyses it is preferable to use green wavelengths where water has a transmission window
- For shorter laser wavelengths, the continuum component of the LIBS plasma is lower due to reduced (inverse Bremsstrahlung) absorption of the laser radiation by free electrons in plasma.

Lower continuum emission is favourable when using a compact and cheaper CCD detector without gating option.

Beam quality of the laser is important for obtaining small spot sizes (micro-sampling) and it is particularly critical for long-range (stand-off) measurements where the beam is focused at distances up to 100 m [14]. In the latter case, also the beam directionality becomes very important.

Pulse-to-pulse laser stability is not critical for the signal accumulation over a sufficient number of laser shots. It becomes more critical in the case of single shot quantitative analyses without applying some signal normalization (see section 2.5).

In the majority of LIBS measurements a flash-lamp pumped, Q-Switched Nd:YAG laser is used. This type of laser is well commercially established and has many advantages over the other laser sources. Among them, there is also the possibility to operate at different wavelengths (1064 nm, 532 nm, 355 nm and 255 nm). Often, all these wavelengths could be changed inside the single laser source, by an appropriate insertion of the frequency conversion elements. Beside, two or more laser pulses can be also extracted during a single lamp flashing [15], with advantages for the analytical LIBS performance [16].

Research on the LIBS system miniaturization and with reduced power consumption has brought to the implementation of diode pumped lasers containing a passive QS [17-18]. In absence of the amplification stage, these lasers can produce the nanosecond pulses with energy up to 2 mJ. Due to low pulse energy, a tighter focusing is required in order to achieve sufficient SNR.

2.2.2 Optical system

Laser beam, sometimes expanded, is focused onto a sample by means of one or more focusing lenses. In some cases, instead of lenses a telescopic system containing the mirrors is employed [14]. Focal length of the system must provide a sufficiently small laser spot, i.e. the laser energy density high enough for the plasma generation. Using low energy lasers, such as microchip lasers [17], it could be necessary to employ a microscopic objective for the beam focusing. For underwater LIBS applications, a lens (or lenses system) with a short focal length must be used (example 20-30 mm) due to water absorption and light scattering by the eventual suspended particles [19], bubbles and hydro-aerosols.

Beside a bi-axial configuration for the laser beam focusing and plasma light collection (Fig. 2.2), a mono-axial system is often used (Fig. 2.3). This configuration is less sensible to misalignment and particularly recommended for analyses of irregular surfaces.

For most of the sample types, the elemental emission lines in UV spectra supply a lot of analytical information, so the collecting optical system should be transparent in this spectral range. In these cases quartz optics is usually employed.

Typical collecting system contains an optical fibre or a fibre bundle. In the latter case, the exit of the bundle can be arranged into a line, to match or to replace the monochromator entrance slit. If an array of the compact spectrometers is used, a fibre bundle serves to split the optical signal towards the entrances of different spectrometers.

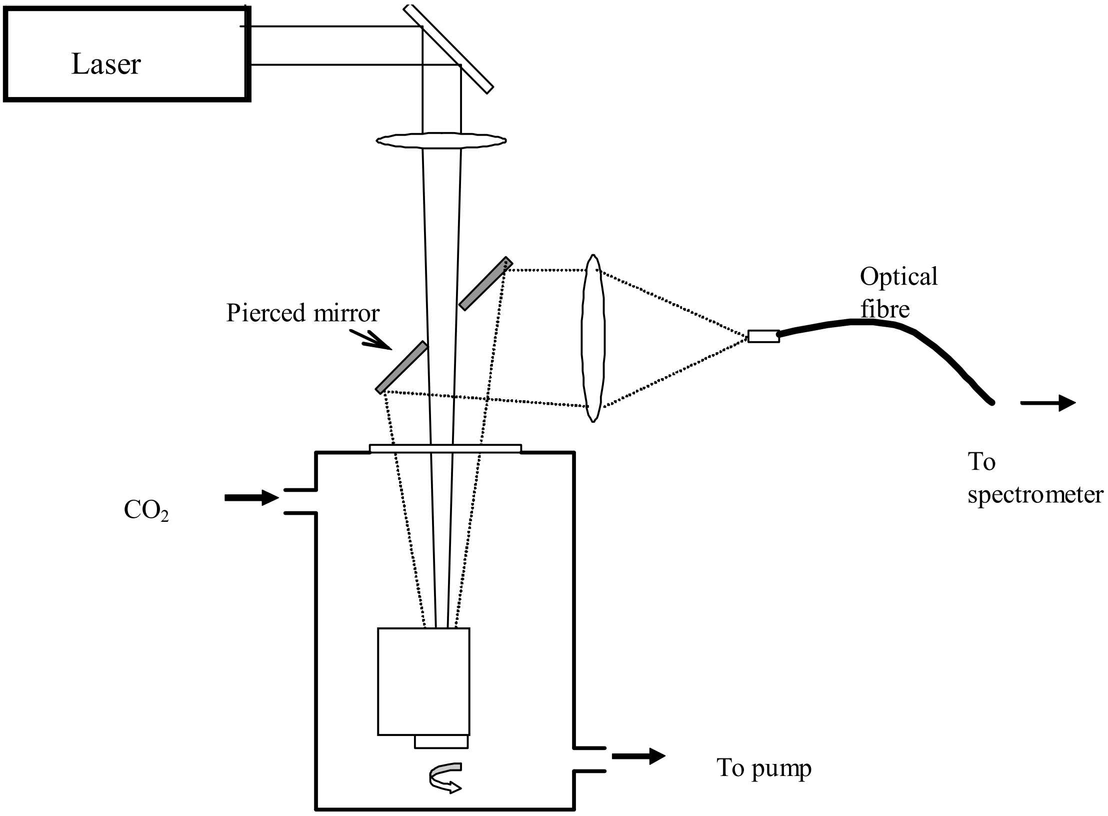

Figure 2.3: Example of mono-axial LIBS system configuration, here used for measurements inside a low pressure chamber

2.2.3 Spectrometers and detectors

Due to spectral interferences, it is important to use High Resolution (HR) spectrometers, a 0.1 nm or better resolution is typical for the LIBS systems. In Fig. 2.4 there is an example of LIBS spectra obtained by a Low Resolution (LR) compact spectrometer and by a HR system (0.55 m monochromator, grating 1200 gr/mm). The loss of the analytical information is clear in the case of a LR system, which generally allows for the detection of the main sample constituents but rarely of minor and trace elements. This fact is not only caused by the spectral overlap of different lines, but also by reduced SNR, critical for the weak emission lines such as expected for the elements present in the low concentrations .

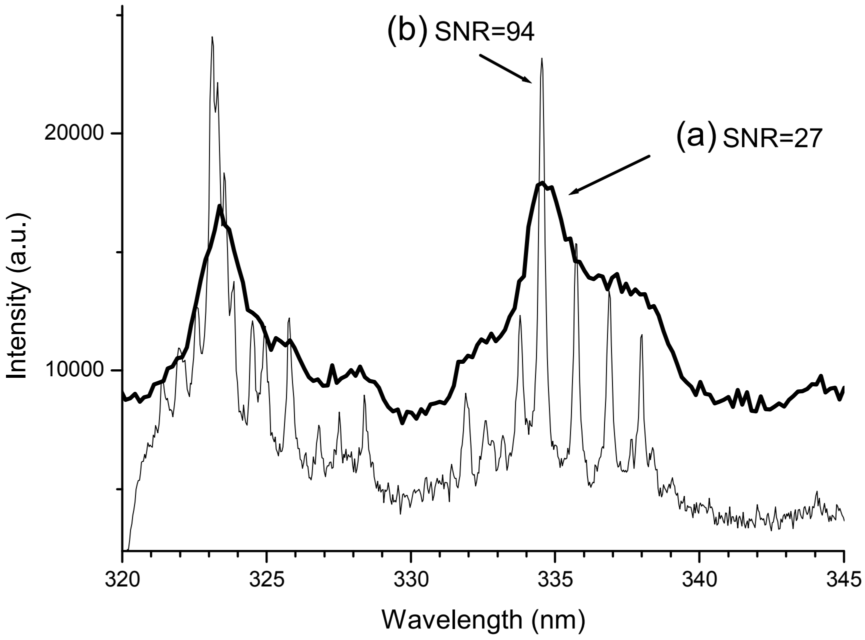

Figure 2.4: A single-shot LIBS spectrum from a sediment recorded: (a) by a Low-Resolution system (0.3 nm); (b) by a High-Resolution system (0.1 nm)

New designs of the HR spectrometers have been developed for LIBS, in particular the compact spectrometers [20-21] and Echelle [22-23].

Compact spectrometers (Fig. 2.5) usually incorporate a CCD array or Photo-Diode Array (PDA) detectors, and up to eight modules are used to cover the spectral range between 200 nm and 1000 nm. These modules are synchronized between them and with the laser pulse. The detectors employed here (CCD or PDA) do not allow for controlling the acquisition gate width, and the integration time is of order of 1 ms. This fact is disadvantageous in several cases:

- In presence of an intense background illumination (daily light): the long integrated continuum light partially masks the LIBS signal of a relatively short duration (in order of 1-10 μs).
- For detection of short living species, which recombine in the plasma
- For detection of the plasma in Local Thermal Equilibrium (LTE), often necessary for the plasma modelling (section 2.3).
- For underwater measurements if a sonoluminescence emission occurs following the collapse of a vapour bubble formed after the breakdown. The bubble collapse appears later than the LIBS signal and a very strong and broad sonoluminescence sometimes completely masks the LIBS emission [19].

Conventional Czerny-Turner spectrometers often have a CCD (or ICCD) for recording of the dispersed light. Although CCD operation as an image detector can be used for measuring the spectrally resolved light distribution along the slit, for LIBS analyzes the CCD is usually operated in full vertical binning.

Figure 2.5: Example of a compact, high-resolution spectrometer [20]

Echelle spectrometer (Fig. 2.6) employs square CCD (example 1024x1024 pixels), usually with an intensifier. This spectrometer contains cross-dispersive elements to produce highly resolved spectrum in one direction and then to separate different grating orders along the perpendicular axis [22]. The image recorded at the exit plane, contains various orders corresponding to different wavelength ranges. For spectral analyses, specific software is required to transform so formed image to the spectral light distribution. With the commercial Echelle spectrograph, the full spectra can be recorded in the range of 200-800 nm or 200-1000 nm, and with a resolution of 0.05-0.1 nm. Contemporary recording of the full spectra drastically reduces the measuring time for multi-elemental analyses. Single-shot full spectra are necessary for a single sample point characterization, as for example: during the multi-elemental surface mapping or vertical sample profiling, then for characterization of small targets (example droplets) and for micro-destructive analysis as is the case of artistic and historical objects. However, Echelle spectrometer have some disadvantages, the most important beside a high cost, is a relatively low signal.

The most advanced and flexible LIBS detection is based on an ICCD sensor, which allows both for the measurements of the spatial and temporal distribution of the spectra. The detector can be gated down to a few nanoseconds and is used for determining of the temporal plasma behaviour. A main disadvantage of an ICCD is a relatively high cost and larger dimensions, so it is not used for the compact LIBS systems. Comparison of the CCD and ICCD based system for LIBS is reported in [24].

For a limited number of analyzed emission lines, which are free of spectral interferences, instead of spectrometers it is possible to use also narrow band-pass filters coupled with other detectors such as a photomultiplier (PMT), photodiode (PD), avalanche PD etc. Such types of detection systems are generally implemented for some very specific applications.

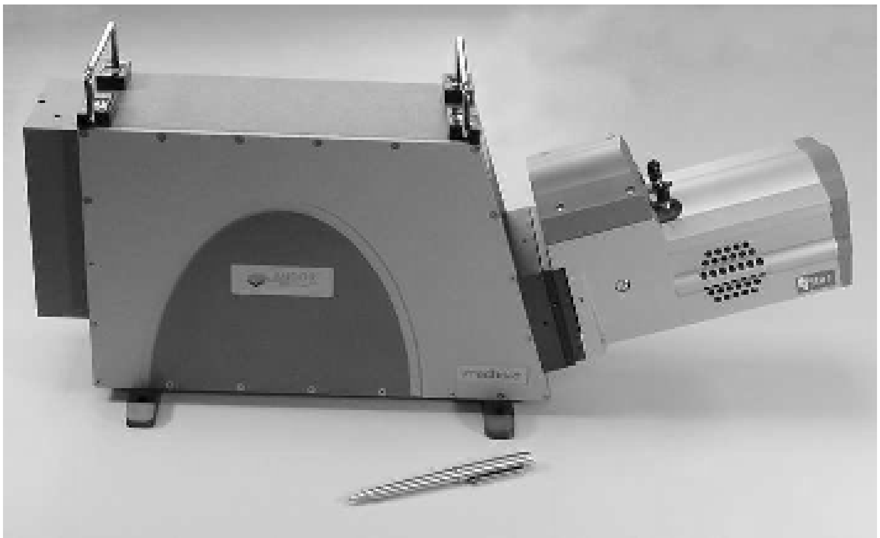

Figure 2.6: Echelle spectrometer [23]

2.3 Plasma properties

LIBS diagnostics, and in particular quantitative LIBS analysis, are often based on some assumptions, the most common are that the detected plasma is optically thin and in LTE. Starting from these assumptions, the plasma parameters (temperature and electron density) can be determined from the measured LIBS spectra and used for further data processing.

2.3.1 Plasma in equilibrium

For a partially ionized gas in a closed system, Complete Thermal Equilibrium (CTE) requires a presence of the following distributions and that these distributions are characterized by the same temperature T [3]:

1) Velocity of the particles have Maxwell distribution
2) Population of bound states has Boltzmann distribution
3) Population distribution among ionization states is described by Saha equation
4) Dissociation product have Guldberg-Waage distribution
5) Distribution of radiation is described by Planck's law.

In laboratory conditions the plasmas are usually characterized by the low optical density and by temperature gradients, which prevent establishment of CTE. The most prevalent deviation from CTE regards Planck's distribution, which is rarely fulfilled due to loss of radiative energy that is not reabsorbed within the plasma boundaries. However, even in the systems with density and temperature gradients, the temperature equivalence of other distributions (excluding the Planck's) can remain locally valid if the electron density is sufficiently high. Plasmas in which equilibrium is maintained for all distributions (except Planck's function) at any spatial point are said to be in Local Thermal Equilibrium (LTE).

If the plasma is in equilibrium, the ionization depends only on the plasma conditions (density and temperature). LTE occurs in high-density plasma where collisions dominate over radiative processes. Differently, low density plasmas have often a charge state which is significantly lower than the equilibrium value. In the case of LIBS plasmas, it is often assumed that observed plasma volume, cantered to the hot plasma core, is in LTE. However, the external plasma regions are known to be cooler and less dense and part of their emission is also collected together with the emission coming from the plasma core.

Let's assume that the plasma contains only electrons (*e*), atoms and their first ionization stages, as it is usually case in LIBS plasmas during the detection window. Both heavy particles and electrons have Maxwell distribution corresponding to their temperatures: T_h and T_e respectively, where T_h depends on the particle mass. If the plasma is in LTE, the electron temperature and the temperature of heavy particles are identical ($T_h = T_e \equiv T$), and the level population for all atoms/ions is given by Boltzmann formula, which includes the unique plasma temperature:

$$\frac{N_k}{N_i} = \frac{g_k}{g_i} e^{-(E_k - E_i)/KT} \tag{2.1}$$

Where k, i refer to two levels with the corresponding populations N_k and N_i, which energies are E_k and E_i respectively. The corresponding level degeneracy's are g_k and g_i, which are given in the atomic data-bases. Here, K is Boltzmann constant and $U(T)$ is partition function for a single species (tabulated values).

For the plasma in LTE, neglecting re-absorption effects of the emission, the recorded spectrally integrated line intensity I^{ki} corresponding to the atomic or ionic transition between energy levels E_k and E_i of the species α (atomic or ionic) is given by:

$$I^{ki}{}_{\alpha} = a'_{\alpha .} N_{\alpha} \frac{g_k A_{ki} e^{-E_k/\mathrm{k}T}}{U_{\alpha}(T)} \tag{2.2}$$

where a'_{α} is a constant depending on the experimental conditions, N_{α} is species number density in the plasma, A_{ki} is the transition probability. If the LIBS instrument is corrected for the spectral response, the atomic data accurate and complete, and the whole plasma volume imaged into detector or the species have the same distribution in the plasma, the constant a'_{α} is the same for all the species.

For plasma in LTE the relative populations among ion stages are given by the Saha equation [3]. In typical LIBS plasmas during the observation window, a presence of the second and higher ionization stages could be neglected. Accordingly to the Saha equation, the number density ratio of neutral (N_α^I) and first ionized species (N_α^{II}) of each element α in the plasma depends on plasma temperature and electron density N_e:

$$\frac{N_\alpha^{II}}{N_\alpha^{I}} = \frac{1}{N_e} \cdot \frac{U_\alpha^{II}(T)}{U_\alpha^{I}(T)} B(\mathrm{k}T)^{3/2} e^{-\frac{E_\infty}{\mathrm{k}T}} \equiv f_{2\alpha}(N_e, T) \tag{2.3}$$

where: $U_\alpha^I(T)$ and $U_\alpha^{II}(T)$ are partition functions of atomic and the first ionization stage respectively; E_∞ is the effective ionization energy in the plasma surrounding; B is a constant with a value of 6.05E+21 cm^{-3}

LTE requires that collisional excitation and de-excitation rates dominate over radiative processes, a condition achieved if the plasma electron density is sufficiently high thus to allow the rapid energy exchange [25]:

$$N_e(cm^{-3}) \geq 1.6 \cdot 10^{12} \cdot \sqrt{T(K)} \cdot \Delta E^3 \tag{2.4}$$

where ΔE (eV) is the largest energy gap for which LTE conditions hold. An existence of LTE requires high electron densities in plasma (typically 10^{17} cm^{-3} or higher) to involve both the atom and their ions in the LTE. Such high electron densities are often achieved in LIBS plasma generated at atmospheric or higher ambient pressures.

Beside this condition (eqn. 4), LTE requires that local gradients of plasma properties (temperature, density, thermal conductivity) are low enough to let a particle in plasma to reach equilibrium. In fast expanding LIBS plasmas immediately after its formation or expanding into a low pressure surrounding, LTE is often missing as collisions and particle diffusions can not equilibrate rapid temperature/density variations. Usually, the LIBS plasmas at atmospheric pressures reach LTE after a time interval in order of 0.1-1 μs from its formation, and passes through successive states of LTE until the electron density becomes too low to satisfy criterion (2.4).

2.3.2 Plasma temperature

There are different methods for measuring the plasma temperature from its spectral emission [3], and the most used approach is based on the intensity ratio between two or more lines belonging to the same species. Starting from the eqn. (2.2), the measured intensity ratio of two lines from the same species α (atomic or ionic) is:

$$\frac{I'}{I} = \frac{g'A'}{gA} e^{-(E'-E)/KT} \tag{2.5}$$

Here, the indexes k, i are omitted from the expression.

By measuring the integral line intensities obtained by the instrument previously corrected for the spectral response, and for the lines with known values of A, g and E, it is possible to calculate the plasma temperature. The chosen lines must not be self absorbed; otherwise the calculated values could be quite erroneous. The two lines method for the temperature determination is not precise, and the accuracy can be improved by including simultaneously more lines of the same species into the calculation. To evaluate the plasma temperature, we take the natural logarithm of equation (2.2) obtaining:

$$\ln\left(\frac{I^{ki}{}_{\alpha}}{g_k A_{ki}}\right) = -\frac{E_k}{\mathrm{k}T} + \ln\left(\frac{N_\alpha a_\alpha}{U_\alpha(T)}\right) \tag{2.6}$$

By plotting the left hand term of equation (2.6) as a function of E_k , different emission lines intensities belonging to the same element lie along a straight line with a slope of *-1/kT*. This is called Boltzmann plot and for obtaining a good accuracy in the temperature calculation it is crucial that the line constants, given in the data bases, are accurate, that the upper levels are sufficiently spaced and inside limits of LTE (see eqn. 2.4) and that the considered lines are not saturated. An example of Boltzmann plot is shown in Fig. 2.7, obtained from a LIBS spectra of one copper alloy in air. The temperature calculation was performed automatically, after fitting the whole spectra (240-750 nm) and the details are given in [26].

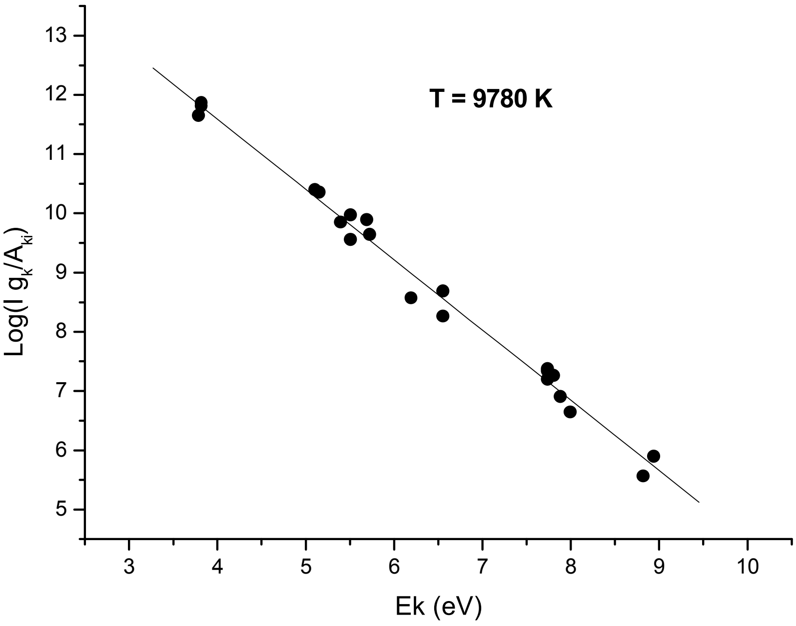

Figure 2.7: Example of the Boltzmann plot and the calculated plasma temperature [26]

Initially, the LIBS plasma temperature is very high, and auto-ionization is dominant. The fast collisionaly processes bring the plasma to the conditions of LTE where the electrons have Maxwell distribution, all the species have the same temperature, the population of energy levels corresponds to Boltzmann distribution, and the Saha equation describes the concentration ratio between two successive ionization stages. Further plasma cooling, expansion and recombination cause plasma departure from LTE. One of the indicators for missing LTE conditions is the Boltzmann plot. In Fig. 2.8 there is an example of the Boltzmann plot measured at different delays from the laser pulse [27]. A straight line, indicating the Boltzmann population, fits well the data point only for delays between 100 ns and 1500 ns. For other delays, there is a loss of LTE over the considered energy span (3-7 eV).

In the early plasma stage, the ionic temperature is higher than the atomic one, and by comparing them an indication about LTE existence can be obtained.

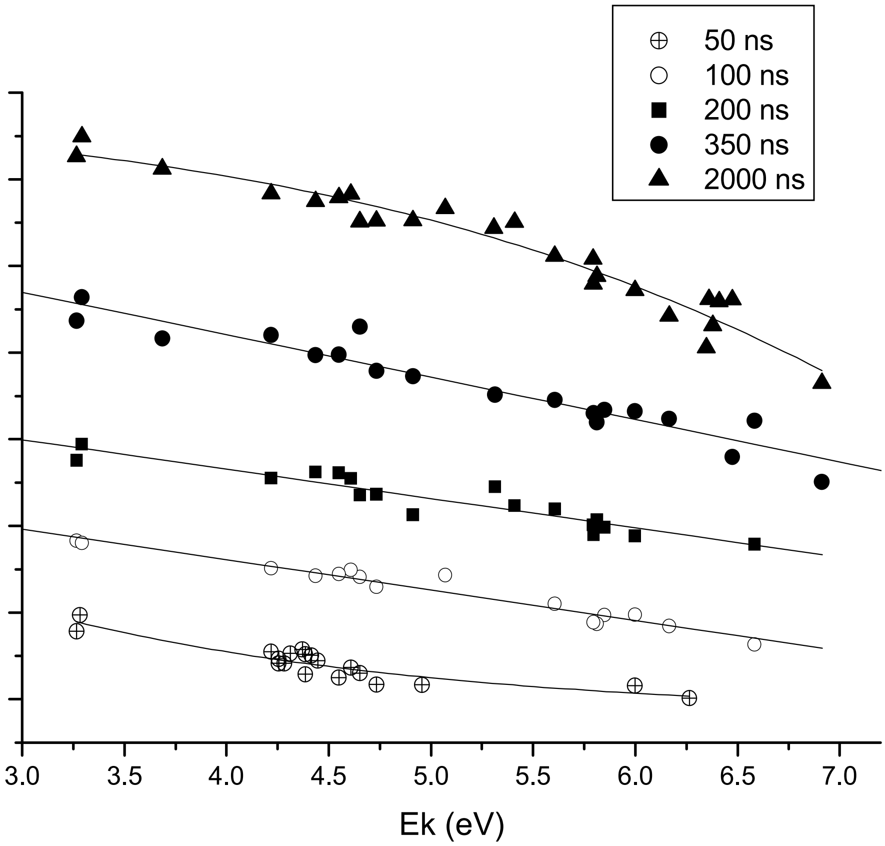

Figure 2.8: Boltzmann plot measured over Fe atomic lines at different delays from the laser pulse; the sample is stainless steal in air [27]

2.3.3 Electron density

Once the plasma temperature is known, the electron density can be calculated from the spectrum: one way to calculate it is through the Saha equation (eqn. 2.3). From the line intensities of an atomic and its first ionization degree, their concentrations N_α^I and N_α^{II} respectively can be retrieved from eqn. 2.2. Then the electron density can be derived from eqn. 2.3:

$$N_e = \frac{N_\alpha^I}{N_\alpha^{II}} \frac{U_{II}(T)}{U_I(T)} B(\mathrm{k}T)^{3/2} e^{-\frac{E_\infty}{\mathrm{k}T}} \tag{2.7}$$

These calculations require an existence of LTE over a large span of the level energies, which includes both the atomic and ionic levels.

Under usual LIBS conditions, the line widths are mainly determined by the instrument and by the Stark broadening. The latter is caused primarily by collisions with the free electrons, although there is a smaller contribution of the collisions with ions. The most common method for determining of the electron density in LIBS plasmas is based on measurement of the Stark halfwidths of the atomic or ionic lines, for which the broadening coefficients are known in the literature [28]. Except for hydrogen lines, for which the formula is different, the electron density could be calculated from the measured Stark width $\Delta\lambda_s$ of the line [29]:

$$\Delta\lambda_s \cong 2w(T)\cdot[1+1.75\cdot 10^{-4} N_e^{1/4} A(T)(1-0.068\cdot N_e^{1/6} T^{-1/2})]\cdot 10^{-16} N_e \tag{2.8}$$

where *w(T)* is electron impact half-width, N_e is electron density (cm^{-3}) and *A(T)* is ion-broadening parameter. The second and the third term in the brackets often can be neglected in the case of LIBS plasmas, so the expression from above is simplified and rewritten as:

$$N_e \cong \frac{\Delta\lambda_s}{2w(T)}\cdot 10^{16} \tag{2.9}$$

If the other types of line broadening, such as Doppler, Wan der Waals and resonant broadening can be neglected [29], as common for the LIBS plasmas [5], the Stark broadening can be obtained from deconvolution of the considered spectral line. For ionic lines and for atomic lines in absence of significant ion broadening, the line profile is described by Voigt function. The Gaussian component is due to the instrumental broadening, to be determined experimentally, and remaining FWHM is attributed to the Stark broadening described by Lorentz's function.

2.3.4 Self-absorption

Plasma is optically thin when the emitted radiation traverses it and escapes from the plasma without significant absorption. In the case of strongly emitting atomic lines from the main sample constituents, the approximation of optically thin plasma often is not applicable. As a consequence, the relationship between the integrated line intensity and the species concentration (eqn. 2.2) is not valid. Self-absorption of an analytical line also leads to a non-linear behaviour of the calibration curves (see section 2.5), showing a saturation at high element concentrations.

Optical thickness at a certain transition wavelength causes the line broadening due to self-absorption, and sometimes, even the line self-reversal (Fig. 2.9). In the case of multiplet transitions, the existence of self-absorption for these lines can be checked by comparing their intensity ratios. In the presence of the line absorption, the stronger lines when compared to those less intense from the multiplet have lower values than those given in the data-bases. Self-absorption of the lines have negative effects in the calculation of the plasma parameters, and a careful choice of the emission lines for such calculation must be performed [5, 30].

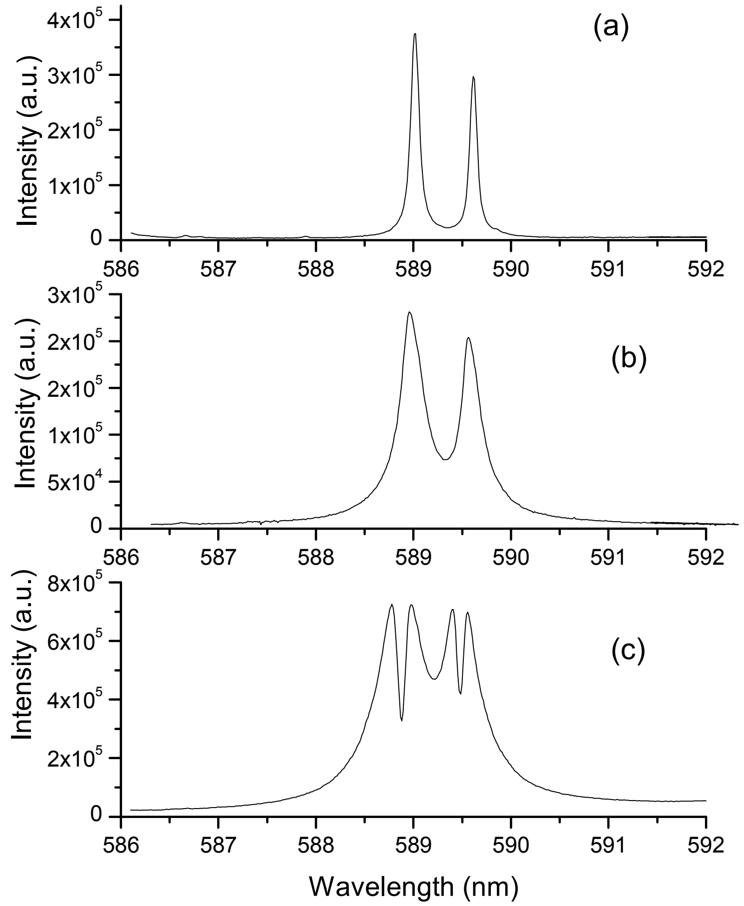

Figure 2.9: Na resonant lines detected by LIBS: (a) optically thin plasma at these transitions; (b) in presence of self-absorption; (c) self-reversal due to a strong self-absorption

2.4 QUALITATIVE LIBS ANALYSES

Qualitative analyzes are aimed to establish the elements present in the sample, by exploiting the information from the registered spectrum. This information include: the wavelength of the emission lines, their intensities and relative intensities of the lines belonging to a single element at a certain ionization stage. The main problem in LIBS analyses of unknown samples is related to the overlap of the emission lines from different elements, both atomic and ionic, given in the data bases. In order to assign the emission lines from the LIBS spectrum and thus to determine the elements present in the sample, it is necessary to consider the next:

- The LIBS spectra, in typical time detection interval, have the detectable lines only from the atoms and single ionized species. Emission from higher ionization stages can be generally neglected.
- When using a relatively long acquisition delays (in order of μs), except for some strong ionic lines belonging to the elements with a low ionization energy, the ionic emission becomes rather weak and the spectrum is dominated by the atomic lines.
- Dynamic of the emission lines also depend on the composition and pressure of surrounding atmosphere.
- *A priori* knowledge of the sample type is very useful for assignment of the emission lines.
- Relative line intensities given in the databases can be exploited for the line assignment. Particularly, multiplet lines of one element are useful for the identification – if one of them is present and relatively strong (quiet above the detection threshold), also the others must be observed.

2.5 Quantitative analyzes

Quantitative analyses are aimed to determine the concentrations of different elements in the sample. LIBS technique applied for measurements of the element concentrations is not considered a very accurate and highly sensible technique as for example ICP-OES. Typically, LIBS analyses of solid samples with *a priori* known matrix have uncertainty 5-10%. The Limits Of Detection (LOD's) are in ppm range and at fixed experimental conditions, they depend on the element analyzed. The analytical accuracy is also influenced by the experimental conditions, where some of the parameters, such as the laser energy fluctuations, can be controlled and corrected. The measurement error also depends on the sample physical and chemical properties [4, 31]. The latter is related to the so-called matrix effect [32-33] i.e. to the strong influence of the material composition on the produced plasma emission and therefore on the final analytical results.

2.5.1 Variables affecting the quantitative analyzes

2.5.1.1. Sample properties

Sample overall chemical composition has a great influence on the relative emission line intensities in the plasma. If the sample contains a higher amount of easily ionized elements, such as alkali elements, the laser produced plasma has a higher density of the electrons. The increase of the electron density leads to a more efficient electron-ion recombination. As a result, the ratio of neutral to ionic species in the plasma increases (see eqn. 2.3) and this affects the concentration measurements [33].

In addition to the chemical composition, the physical properties of the sample, such as: absorption at the laser wavelength, heat capacity, vaporization temperature, grain size and material compactness (some of these properties are chemically dependent), influence the laser ablation rate and also the plasma parameters. The grain size is related to the persistence of the laser generated aerosol above the sample surface, with consequences on the signal intensity (see the next section) [4, 34]

2.5.1.2. Sampling geometry

The laser energy density on the sample surface, which is determinant for the ablation rate per pulse and for the signal intensity as well, depends on the focal length. If this one is shorter, the system is more sensible to defocusing i.e. to the variations of the Distance Lens-Surface (DLS). This factor becomes critical when analyzing the rough surfaces. With the changes of the energy density on the sample, both plasma shape and plasma parameters vary [35], as well as a fraction of the atomized material with respect to the material removed mechanically from the surface (by shock-waves end eventual splashing). The optimal sample position for obtaining the highest signal by laser-induced ablation of solids is slightly above the focal plane [36-37]. At analogue energy densities on the sample, the ablation rate (so the signal), behaves differently with defocusing way when employing a spherical or a cylindrical lens [36].

The laser ablation also produces an aerosol, composed of substrate material. The aerosol persistence above the sample surface depends on the ambient pressure. When a dense aerosol formed by the previous laser pulse persists and relative long focal lengths are used, the energy density needed for plasma formation can be reached already much above of the analyzed surface [36]. This causes a partial absorption of the laser energy before reaching the sample. Consequently the sample ablation rate and the LIBS signal, is considerably reduced. On the other hand, the same aerosol presence, although scatters the incoming laser radiation, can contribute to a signal increase for intermediate focusing distances. Here, the threshold for plasma formation on the aerosol can is reached close to the sample surface, in the volume occupied by the plasma produced by the sample ablation. In this case, the aerosol containing the target particles is excited in the hot plasma and can even increase the intensity of the analytical lines as the sample material is already available without spending the energy on surface ablation.

Other important factors are – the plasma shape and which portion of the plasma radiation is collected by the system and brought to the detection system. The plasma in a low pressure environment is more expanded, while at higher pressures it tends to elongate towards the focusing lens with increase of the laser energy [35]. If the collection system collinear with the focusing one (Fig. 2.3), a great amount of the emission generated closer to the sample surface can be lost due to absorption by the plasma volume nearer to the focusing lens.

The plasma also has a temperature distribution, with a hot core and colder external regions [38]. The species density distribution is not uniform [36], and there is a higher fraction of atoms in the plasma core [38-39] due to higher electron density and more efficient recombination. The ions are generated in the earlier plasma stage, and by the plasma expansion, brought before the atoms to the plasma edges [40]. All this determine a geometry dependent intensity of different emission lines even belonging to a single species [39].

2.5.1.3 Sampling method

As discussed before, the laser ablation produces a persistent aerosol above the sample, which might influence the LIBS signal. An aerosol amount increases with the laser repetition rate. At fixed laser energy, the optimal repetition rate regarding both the LIBS signal intensity and Relative Standard Deviation (RSD) is strongly matrix dependent [4].

Laser ablation creates small craters on the surface by laser-induced evaporation and material removal by the shock waves produced. On the compact materials such as metals, glasses, rocks etc., the crater diameter close to the laser beam diameter, while the depth depends on the ablation rate and on the number of the applied shots. When the laser pulses are applied to soft materials such as soils, the laser produced craters are much larger, because the material particles are easily removed by the shock waves. For sampling at a fixed position, a crater depth changes DLS and the distance between the plume and collecting optics. The plasma parameters also changes with the crater depth as the laterally confined plasma is denser and hotter than the plasma expanding semi-spherically into a free space [41].

Beside the crater effect and aerosol formation, which influence the LIBS signal, there is also a possible local surface enrichment with relatively large particles and heavier elements. This happens since the lighter particles are removed much easier by the shock waves. Then, the successive laser pulses find the surface containing different average particle size and with a different composition from the target.

All here mentioned matrix-dependent factors affect the measuring accuracy. However, they can be partially compensated by sampling at different, always fresh points [4]. This is practicable by moving the sample (example rotation) or the optical head containing both the focusing and collecting system. The aerosol itself can be removed by a slight gas flow above the solid sample.

2.5.1.4 Surrounding environment

The LIBS plasma is produced inside gaseous (or liquid) environment, which composition and pressure influences the plasma characteristics and the results of the measurement. [42]. Reducing the atmosphere pressure, the plasma generated at the leading edge of the laser pulse is less dense as it expands more effectively into a low pressure surrounding. A remaining (later) portion of the laser pulse is then less shielded by the plasma itself, i.e. better coupled to the target. This leads to an increase of the ablation rate with reducing of the surrounding gas pressure down to a few mbar. The fraction of the atoms in plasma decreases with lowering of the pressure due to reduced number of collisions in more expanded, less dense plasma. Both the plasma excitation and decay rate are determined by the collisions, which are pressure dependent. The overall influence of the gas pressure on the LIBS signal intensity is a result of the above mentioned factors and of the changes in the plasma geometry. The latter determines a portion of the plasma collected and brought to the detection system.

Ionization potential of the ambient gas is of a particular importance for the LIBS signal. A lower gas ionization potential means that is easier to produce the plasma and that its temperature is expected to be higher. Cooling processes in the plasma are more efficient for lighter gases (example He), and this leads to a faster plasma decay. In summary, the measured LIBS intensities are higher as the surrounding gas is heavier and with an ionization potential [4].

2.5.2 Different approaches in quantitative LIBS analysis

2.5.2.1 Calibration

Common approach for obtaining quantitative material analyses by LIBS is based on use of the calibration curves generated after measurements on the reference samples. The main limitation of this approach is related to the previously discussed matrix effect. Optimally, the initial calibration should be performed with standards having the matrices similar to that one of the samples to be characterized, and reliable concentration values can not be retrieved by LIBS on a priori unknown samples. Even for the well matched standard matrices, different sources of analytical errors could be present, such as slight variation of the experimental conditions, differences in the coupling of the laser radiation with the samples and on aerosol formation with respect to the standards used.

LIBS analytical accuracy can be improved by reducing the effects of variable experimental conditions and ablation rates. To this aim, different kinds of the LIBS signal normalization have been proposed. The examples include lines intensities normalization: on the acoustic plasma emission [43], on the continuum plasma emission [44-45], on the overall plasma emission [46] and on a line intensity of some major matrix element [47]. The latter type of normalization is often used in LIBS measurements on samples with unknown composition. In this way only the relative concentrations can be retrieved, except for well characterized matrices with a fixed content of the element used for the normalization. In Fig. 2.10 there is an example of the calibration graph obtained before and after the line intensity normalization on the integrated plasma emission [46]. In the latter case, the point scattering on the calibration graph is significantly reduced, as it can be seen form the reduced standard deviation (SD) and improved correlation factor R.

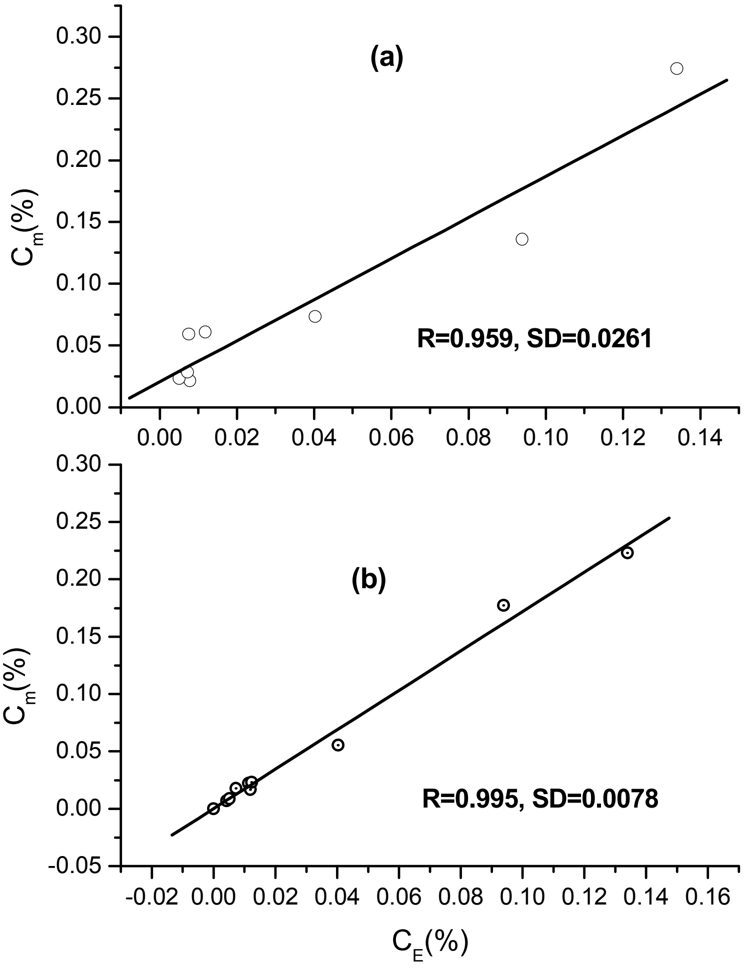

Figure 2.10: LIBS measured vs. certified Cr concentration for different soil-like reference samples (atomic transition at 425.43 nm) before (a) and after the line intensity normalization (b) on the integrated spectral emission (240-750 nm).

In order to analyze quantitatively the samples starting from calibration on reference materials whose LIBS plasmas have different temperature and electron density, correction coefficients for the element concentrations have been derived [44]. After generating the calibrations plots $I(C^{REF})$ for single elements by using standards with different concentrations C^{REF}, the calibration coefficients A^{REF} are determined for corresponding T^{REF} and N_e^{REF} i.e. temperature and electron density in the case of reference samples. For an unknown sample which plasma has T^X and N_e^X different than in the case of reference materials, the concentration C^{REF} found from the calibration graph should be corrected for the factor F^X that accounts for differences in plasma parameters:

$$C^X = F^X \cdot C^{REF} \tag{2.10}$$

The correction coefficient F^X for the concentration measurements through an atomic line emission was derived step-by-step and can be expressed as:

$$F^X = \frac{A^{REF}}{A^X} = \frac{1 + f_2(T^X, N_e^X)}{1 + f_2(T^{REF}, N_e^{REF})} \cdot \frac{U^I(T^X)}{U^I(T^{REF})} \cdot \frac{e^{-E_k/kT^{REF}}}{e^{-E_k/kT^X}} \tag{2.11}$$

where $f_2(T,N_e)$ corresponds to the number density ratio of ions and atoms in the plasma (see eqn. 2.3).

If an element concentration is measured through an ionic line emission, the derived correction factor F_i^X in eqn.2.10 results:

$$F_i^X = \frac{1 + 1/f_2(T^X, N_e^X)}{1 + 1/f_2(T^{REF}, N_e^{REF})} \cdot \frac{U^{II}(T^X)}{U^{II}(T^{REF})} \cdot \frac{e^{-E_k/kT^{REF}}}{e^{-E_k/kT^X}} \tag{2.12}$$

Although the correction factors were here derived neglecting the line self-absorption, the latter effect, whenever present, is partially compensated by a non-linear calibration curve.

2.5.2.2 Calibration-Free method

Calibration for the quantitative LIBS analysis is time consuming and limited to a certain class of the samples. Another approach for retrieving the element concentrations by LIBS is the so-called Calibration-Free (CF) procedure [48-49], which is based on a simultaneous detection of all major elements in the sample and on assumption of the plasma in LTE. Plasma temperature T can be determined from Boltzmann plot (see section 2.3) and then the plasma electron density can be also calculated. The species concentrations in the plasma could be determined from the emission of one neutral (or ionic) line (eqn. 2.2) and the number density of the corresponding ions (i.e. atoms) is then calculated from the Saha equation (eqn. 2.3). If the sample stochiometry is conserved in the LIBS plasma, the concentration of the element α in the sample is proportional to the sum of atomic and ionic (single ionized) particles:

$$C_\alpha = b_\alpha^{'}(N_\alpha^I + N_\alpha^{II}) \tag{2.13}$$

Where b_α' is an experimental constant for one element, which is assumed to be equal for all the elements in CF normalization:

$$\sum_{\alpha} C_{\alpha} = 1 \qquad (2.14)$$

CF procedure requires that all the major sample elements are simultaneously detected by LIBS and was successfully applied for analyses of aluminium and precious alloys [49]. However, there are elements that are difficult to be detected by LIBS, such as sulphur and chlorine, and the elements that suffer from interference from the surrounding atmosphere, such as oxygen for the measurements in air. CF-LIBS applied on unknown samples with a significant content of unidentified or interfering elements (example - on soils), could lead to large measurement errors, up to one order of magnitude [50]. Further limitation of CF-LIBS accuracy is due to uncertainty of the available databases for less studied elements. This in particular contributes to the analytical errors through the calculation of partition functions, included in eqns. 2.2-2.3. CF procedure assume the preservation of the sample stochiometry in the gas phase, which is often missing for some classes of materials, as for example copper alloys containing the zinc [51]. Finally, CF method does not consider losses of atom/ions through chemical reactions in the plasma, which might lead to the formation of molecules and fragments also during the observation time interval. The examples include formation of C_2 after ablation of carbon containing samples, as well as of CN in presence of nitrogen coming from the sample and/or air. The latter fragment might be detected also shortly (500 ns) after the laser pulse and its emission persists for different tenths of microseconds.

2.5.2.3 Hybrid approach

Beside the two above methods for obtaining quantitative LIBS results, a mixed approach including both the initial calibration and CF procedure have been also reported [26]. Here, the initial calibration was used to retrieve the coefficients b'_{α} for each analyzed element, which were supposed to be different from one element to another. Then the CF normalization was applied following the revised formula:

$$\sum_{\alpha} C_{\alpha} / b'_{\alpha} = 1 \qquad (2.15)$$

In this way, the uncertainties in the atomic data bases and matrix effect are partially compensated.

2.6 References

[1] D. A Cremers, L. J. Radziemsky, Handbook of Laser Induced Breakdown Spectroscopy, (2006) John Wiley & Sons Ltd.

[2] E. H. Piepmeier, Laser Ablation for Atomic Spectroscopy, in E.H. Piepmeier (Ed.), Analytical Application of Laser, (1986) John Wiley & Sons (New York)

[3] Griem H. R, 1964, Plasma Spectroscopy, McGraw-Hill, USA.

[4] R. Wisbrun, I. Schechter, R. Niessner, H. Schröder, K. L. Kompa, Detector for trace elemental analysis of solid environmental samples by laser plasma spectroscopy, Anal. Chem. 66 (1994) 2964-2975.

[5] F. Colao, V. Lazic, R. Fantoni, A. Paolini, LIBS application for analyses of martian crust analogues: search for the optimal experimental parameters in air and CO_2 atmosphere, Appl. Phys. A 79 (2004) 143-152.

[6] NIST electronic database, available at http://physlab.nist.gov/PhysRefData/contents-atomic.html

[7] Kurutz electronic database, available at http://www.pmp.uni-hannover.de/cgi-bin/ssi/test/kurucz/sekur.html

[8] D. Winefordner, I. B. Gornushkin, T. Correll, E. Gibb, B. W. Smith, N. Omenetto, Comparing several atomic spectrometric methods to the super stars: special emphasis on laser induced breakdown spectrometry, LIBS, a future super star, J. Anal. At. Spectrom. 19 (2004) 1061-1083.

[9] J. L. Radziemski, From LASER to LIBS, the path of technology development, Spectrochim. Acta Part B 57 (2002) 1109-1113.

[10] F. C. De Lucia, R. S. Harmon, K. L. McNesby, R. J. Winkel Jr, A. W. Miziolek, Laser-induced breakdown spectroscopy analysis of energetic materials, Appl. Optics 42 (2003) 6148- 6152.

[11] A. Giakoumaki, K. Melessanaki, D. Anglos, Laser-induced breakdown spectroscopy (LIBS) in archaeological science - applications and prospects, Anal. Bioanal. Chem. 387 (2007) 749-760.

[12] A. Del Bianco, I. Rauschenbach, V. Lazic, E. K. Jessberger, GENTNER – a miniaturised LIBS/Raman instrument for the comprehensive in situ analysis of the Martian surface, 4th NASA International Planetary Probe Workshop (2006).

[13] A. K. Knight, N. L. Scherbarth, D. A. Cremers, M. J. Ferris, Characterization of Laser-Induced Breakdown Spectroscopy for application to space exploration, Appl. Spectrosc. 54 (2000) 331-340.

[14] S. Palanco, C. Lòpez-Moreno, J. J. Laserna, Design, construction and assessment of a field-deployable laser-induced breakdown spectrometer for remote elemental sensing, Spectrochim. Acta Part B 61 (2006) 88 – 95 .

[15] H. Balzer, M. Hoehne, V. Sturm, R. Noll R, Online coating thickness measurement and depth profiling of zinc coated sheet steel by laser-induced breakdown spectroscopy, Spectrochimica Acta Part B 60 (2005) 1172 – 1178

[16] V. I. Babushok, F. C. De Lucia Jr., J. L. Gottfried, C. A. Munson, A. W. Miziolek, Double pulse laser ablation and plasma: Laser induced breakdown spectroscopy signal enhancement, Spectrochimica Acta Part B 61 (2006) 999–1014.

[17] I. B. Gornushkin, B. W. Smith, N. Omenetto, J. D. Winefordner, Microchip laser-induced breakdown spectroscopy: preliminary feasibility study, Appl. Spectrosc. 58 (2004), 763-769.

[18] J. J. Zayhowski, Passively Q-switched Nd:YAG microchip lasers and applications, J. of Alloys and Compounds, 303–304 (2000) 393–400

[19] V. Lazic, F. Colao, R. Fantoni, V. Spizzichino, S. Jovićević, Underwater sediment analyses by laser induced breakdown spectroscopy and calibration procedure for fluctuating plasma parameters, Spectrochim. Acta Part B 62 (2007) 30–39.

[20] Stellarnet Inc: http://www.stellarnet-inc.com/

[21] Ocen&Optics: http://www.oceanoptics.com

[22] S. Hamilton, R. Al-Wazzan, A. Hanvey, A. Varagnat, S. Devlin S, Fully integrated wide wavelength range LIBS system with high UV efficiency and resolution, J. of Anal. At. Spectrom. 19 (2004) 479–482.

[23] Andor: http://www.andor.com/products/spectrographs/?product=ME5000

[24] J. E. Carranza, E. Gibb, B. W. Smith, D. W. Hahn, J. D. Winefordner, Comparison of nonintensified and intensified CCD detectors for laser-induced breakdown spectroscopy, Appl. Optics 42 (2003) 6016-6021.

[25] T. Fujimoto, R.W. P. Whirter, Validity criteria for local thermodynamic equilibrium in plasma spectroscopy, Phys. Rev. A 42 (1990) 6588-6601.

[26] F. Colao, R. Fantoni, V. Lazic, V Spizzichino, 2002, Laser Induced Breakdown Spectroscopy for semi-quantitative analyses of artworks - application on multi-layered ceramics and copper based alloys, Spetrochim. Acta B 57, 1219-1234

[27] F. Colao, V. Lazic, R. Fantoni, LIBS as an analytical technique in non equilibrium plasmas, SPIE Special Issue on “Spectroscopy of non equilibrium plasma at elevated pressures”,Vol.4460 (2002) (Ockin V. N. Ed) 339-348.

[28] H. R. Griem, Spectral line broadening by plasmas, (1974) Academic press NY and London.

[29] N. Konjevic N, Plasma broadening and shifting of non-hydrogenic spectral lines: present status and applications, Phys. Reports 316 (1999) 339-401.

[30] C. Aragón, F. Peñalba, J. A. Aguilera, Curves of growth of neutral atom and ion lines emitted by a laser induced plasma, Spectrochim. Acta Part B 60 (2005) 879–887.

[31] M. Anzano, M. Villoria, A. Ruíz-Medina, R. J. Lasheras, Laser-induced breakdown spectroscopy for quantitative spectrochemical analysis of geological materials: effects of the matrix and simultaneous determination, Anal. Chim. Acta 575 (2006) 230-235.

[32] P. W. J. M. Boumans, Excitation of spectra, in Comprehensive Analytical Chemistry (G. Svehla Ed.), Wilson-Willson’s, Elsevier Pub. Co, Amsterdam (1976) 1-193.

[33] A. S. Eppler, D. A. Cremers, D. D. Hickmott, M. J. Ferris, A. C. Koskelo, Matrix effects in the detection of Pb and Ba in soils using laser-induced breakdown spectroscopy, Appl. Spectrosc. 50, (1996) 1175 – 1181.

[34] J. E. Carranza, D. W. Hahn, Assesment of the upper particle size limit for quantitative analyses of aerosols using laser induced breakdown spectroscopy, Anal. Chem. 74 (2002) 5450-5454.

[35] S. Yalcin, D. R. Crosley, G. P. Smith, G. W. Farris, Influence of ambient conditions on the laser air spark, Appl. Phys. B 68 (1999) 121-130

[36] V. Bulatov V, L. Xu, I. Schechter, Spectroscopic Imaging of Laser-Induced Plasma, Anal. Chem. 68 (1996) 2966-2973

[37] R. A. Multari, L. E. Forster, D. A. Cremers, M. J. Ferris, The effects of sampling geometry on elemental emissions in laser-induced breakdown spectroscopy, Appl. Spectrosc. 50 (1996) 1483-1499.

[38] J. A. Aguilera, C. Aragón, J. Begoechea, Spatial characterization of laser-induced plasmas by deconvolution of spatially resolved spectra, Appl. Optics 42 (2003) 5938-5946.

[39] B. C. Castle, K. Visser, B. W. Smith, J. D. Winefordner, Spatial and temporal dependence of lead emission in laser-induced breakdown spectroscopy, Appl. Spectrosc. 51 (1997) 1017-1024.

[40] J. Siegel, B. Epurescu, A. Perea, F. J. Gordillo-Vazquez, J. Gonzalo, C. N. Afonso, High spatial resolution in laser-induced breakdown spectroscopy of expanding plasmas, Spectrochim. Acta Part B 60 (2005) 915-919.

[41] S. S. Mao, X. Zeng, X. Mao, R. E. Russo, Laser-induced breakdown spectroscopy: flat surface vs. cavity Structures, J. Anal. Atom. Spectrometry 19 (2004) 1295–1301.

[42] W. Sdorra, K. Niemax, Basic investigations for laser microanalysis: III. Application of different buffer gases for laser-produced sample plumes, Mikrochim. Acta 107 (1992) 319-327.

[43] C. Chaleard, P. Mauchien, N. Andre, J. Uebbing, J. L. Lacour, C. Geertsen, Correction of Matrix effects in Quantitative Elemental Analyses With Laser Ablation Optical Emission Spectrometry, J. Anal. At. Spectrom. 12 (1997) 183-188.

[44] V. Lazic, R. Fantoni, F. Colao, A. Santagata, A. Morone, V. Spizzichino, Quantitative Laser Induced Breakdown Spectroscopy analysis of ancient marbles and corrections for the variability of plasma parameters and of ablation rate, J. Anal. At. Spectrom. 19 (2004) 429-436.

[45] D. Body, B. L. Chadwick, Optimization of the spectral data processing in a LIBS simultaneous elemental analyses system, Spectrochim. Acta B 56 (2001) 725-736

[46] V. Lazic, R. Barbini, F. Colao, R. Fantoni, A. Palucci, Self absorption model in quantitative Laser Induced Breakdown Spectroscopy measurements on soils and sediments, Spectrochim. Acta B 56 (2001) 808-820.

[47] L. St-Onge, M. Sabsabi, P. Cielo, Quantitative Analyses of Additives in Solid Zinc Alloys by Laser-Induced Plasma Spectrometry, J. Anal. At. Spectrom. 12 (1997) 997-1004.

[48] E. Tognoni, V. Palleschi, M. Corsi, G. Cristoforetti, Quantitative micro-analyses by laser-induced breakdown spectroscopy: a review of the experimental approaches, Spectrochim Acta B 57 (2002) 1115-1130.

[49] M. Corsi, G. Cristoforetti, V. Palleschi, A. Salvetti, E. Tognoni, A fast and accurate method for the determination of precious alloy carratage by Laser induced Plasma Spectroscopy, Eur. Phys. J., D13 (2001) 373-377.

[50] F. Colao, R. Fantoni, V. Lazic, A. Paolini, F. Fabbri, G. G. Ori, L. Marinangeli, A. Baliva, Investigation of LIBS feasibility for in situ planetary exploration: An analysis on Martian rock analogues, Planetary and Space Sci. 52 (2004) 117-123.

[51] L. Fornarini, F. Colao, R. Fantoni, V. Lazic, V. Spizzichino, Calibration for LIBS analyses of bronze materials by nanosecond laser excitation: a model and an experimental approach, Spectrochim. Acta B 60 (2005) 1186-1201.

Chapter 3

LASER INDUCED PLASMA UNDERWATER

Abstract
Laser-induced plasma formation inside liquids is discussed together with the plasma properties and effects, such as bubble cavitation, and their consequences on underwater LIBS analyses. Particular attention is devoted to double-pulse LIBS analyses in liquids and importance of the timing between the two pulses.

3.1 Laser initiated plasma inside liquids

Laser Induced Breakdown (LIB) by short pulse exposure (in the microsecond to femtosecond regime) can be result of two mechanisms: multiphoton absorption or cascade ionization [1-2]. These two processes can occur in gases, liquids and solids. Multiphoton ionization is a nonlinear process, which becomes significant only at high laser power densities and/or at short laser wavelengths. Each electron of a media is independently ionized by simultaneous multiphoton absorption, and initial presence of free seed electrons in a medium is not required. The process is fast and it is dominant in femtosecond pulse regime.

Differently, cascade ionization requires that free electrons are already present in the focal volume before the laser pulse arrival [3]. Except in the case of a pure media, such “seed” electrons” are normally present, usually coming from thermal ionization of the impurities. In absence of seed electrons, cascade ionization can build-up only if first, a number of free electrons is produced through multi-photon absorption, also by the starting edge of the laser pulse. Cascade ionization is then build-up through inverse bremsstrahlung absorption, where the free electrons which gained sufficient energy, may ionize a bound electron by collision. Repetition of these processes leads to a multiplications of free electrons, so to the plasma formation. Once initiated, the avalanche ionization continues until the end of the laser pulse. In order to obtain and sustain the breakdown, the rate of an energy gain of the free electrons must exceed the rate of the energy losses due to inelastic collisions. Also, the ionization rate by free electrons must be higher than the loss of free electrons caused by electron-ion recombination and diffusion of free electrons out of focal volume [3].

Cascade breakdown is a probabilistic process [4-6] as it depends on a number of initial free electrons in the focal volume, which is also influenced by liquid impurities. As a consequence, when focusing the laser pulses with duration of picoseconds or longer inside liquids, the breakdown threshold is influenced by the impurity concentrations and types [7]. This dependence vanishes for ultra-short (femtosecond pulses) where multiphoton ionization is dominant process.

The threshold for LIB, also in liquids, depends also on the laser beam properties, such as wavelength, pulsewidth, beam diameter and focusing geometry, the latter determining the plasma shape (see section 3.2).

Once the plasma is formed, it absorbs a significant portion of the remaining part of the laser pulse, mainly through inverse bremsstrahlung effect. The plasma is then rapidly heated, and for pulse durations in order of picoseconds or longer inside liquids, it can reach temperatures of 6000-16000 K [3, 8-9], while the measured plasma pressures are as high as 20-60 kbar [10-12]. The high temperatures and pressures lead to plasma expansion at supersonic velocities, thus generating an acoustic signal and cavitation effects. Visible plasma emission mainly comes from bremsstrahlung emission from free electrons and from electron-ion recombination. These processes produce a broadband spectrum, but this emission might not be detectable for very short laser pulses, which produces cooler plasma and of shorter duration. Following recombination, bound state electronic transitions produce spectral emission lines characteristic for medium.

Experimentally, a breakdown event in liquids is determined through a presence of some of above mentioned effects (visible plasma emission, shock waves and bubbles), and detection of the cavitation bubbles left after the breakdown is often used as endpoint in threshold measurements for short laser pulses [11, 13-14].

A minimum free electron density corresponding to breakdown is usually assumed to be 10^{18} cm^{-3} [15-16], which approximately represents a minimum density at which significant optical absorption occurs in the plasma.

Theoretical modelling of LIB threshold in aqueous media is difficult because the structure and physical properties of water are still not completely understood despite decades of study. Liquids have amorphous nature, with variation of localized potential, which determines a trapping of quasi-free electrons in potential wells, so called solvated states [17]. Molecules in liquid water also tend to associate or cluster on undetermined fashion [18-19], and all these makes difficult to determine the electron mobility in water. Different models for breakdown threshold in liquids have been developed, such as “lucky electron model” [4] and a simple first order model [7, 13, 15]. The numerical simulations indicate that for picosecond or shorter pulses, self-focusing becomes important in aqueous media [20]. Being these models quite complex, here only qualitative description is reported and with emphasis on nanosecond pulses.

In water containing impurities, the threshold for the cascade breakdown is proportional to the ionization energy of water, which is 6.5 eV [18-19]. This threshold decreases with a number of free electrons in focal volume, being the inverse bremsstrahlung absorption proportional to the square of the electron density ($\alpha_{IB} \propto \lambda^3 N_e^2$). Longer laser wavelengths have lower cascade breakdown threshold because this absorption is more efficient. Differently, for pure water carrier density can be neglected [19] and seed electrons must be supplied by multiphoton ionization, which threshold decreases with the laser wavelength.

Cascade breakdown threshold depends on the spot size both due to an initial number of free electrons in the focal volume and to electron diffusion during cascade build-up. However, diffusion effect becomes important only for very long pulses, starting from microsecond range [3].

In Fig. 3.1 there is theoretical simulation of the breakdown threshold in pure and impure water, as a function of the pulse duration for two wavelengths – 1064 nm and 532 nm [3]. Such a general behaviour was confirmed by number of experiments [3]. In the nanosecond pulse range, which is of interest for this dissertation, the LIB threshold for water containing impurities is about four time higher at 532 nm than at 1064 nm due to λ^3 dependence of the inverse bremsstrahlung absorption However, in pure water LIB threshold is much higher at 1064 nm because multiphoton ionization is necessary to produce seed electrons and this process needs 6 photons. Applying the laser excitation in visible, the multiphoton ionization requires only 3 photons and this process is likely to initiate the cascade breakdown in both pure and impure waters [3]. This explains an absence of impurity dependence on the LIB threshold in the case of visible or UV laser excitation. For long pulsewidths of infrared lasers, the LIB is exclusively cascade ionization process, which is multiphoton initiated only in pure media. At shorter pulsewidths, multiphoton initiation becomes more important and differences in LIB threshold between water with or without impurities tend to disappear.

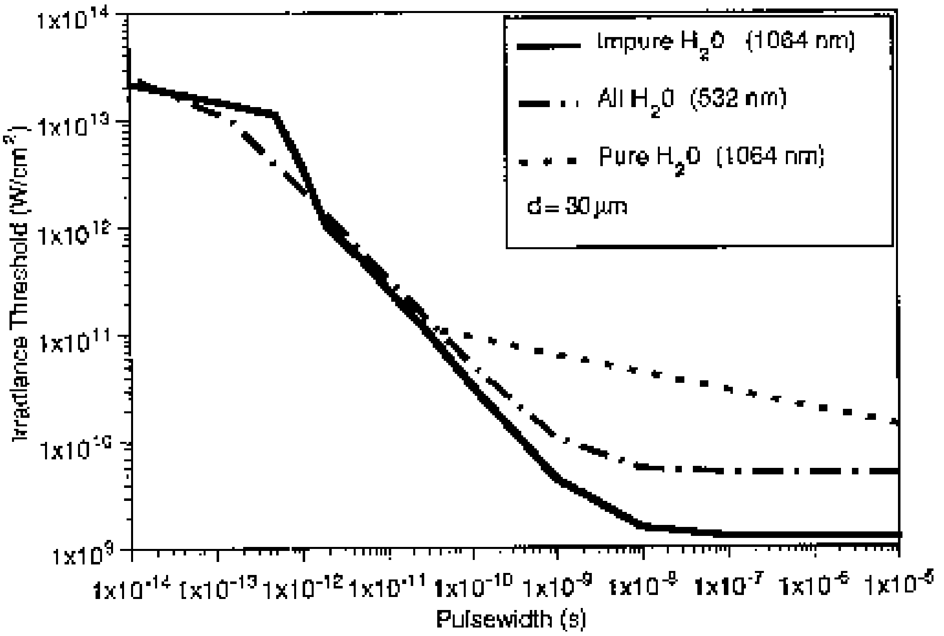

Figure 3.1: Pulsewidth and wavelength dependence of LIB threshold in pure and impure water [3]

Experimentally measured LIB threshold as an influence of the water impurity and the spot size for excitation with 1064 nm and pulse width of 7 ns is given in Tab. 3.1 [21]. These data show strong impurity dependence, where LIB threshold is 3-7 times higher for distilled water with respect to tap water. Saline water has much higher threshold than tap water, but these differences are reduced with increasing of the spot size. However, the decrease of the measured breakdown threshold with the spot size here calculated and not always observed by other authors, might also indicate a presence of self-focusing [22], which apparently decreases the calculated threshold irradiance for larger spot sizes.

Table 3.1: Experimental LIB threshold (I_{BD}) for 7 ns pulses at 1064 nm, measured for different water, corresponding to 100% and 50% breakdown probabilities [21]

Spot size [μm^2]	Medium	I_{BD} 100% [W/m^2]	I_{BD} 50% [W/m^2]
70.7	Distilled	2.1×10^{10}	2.5×10^{10}
	Saline	1.85×10^{10}	1.25×10^{10}
	Vitreous	1.5×10^{10}	1.02×10^{10}
	Tap water	3.0×10^{9}	2.0×10^{9}
132.9	Distilled	1.55×10^{10}	1.05×10^{10}
	Saline	1.35×10^{10}	7.2×10^{9}
	Vitreous	1.17×10^{10}	7.8×10^{9}
	Tap water	2.6×10^{9}	1.5×10^{9}
495.0	Distilled	5.3×10^{9}	2.5×10^{9}
	Saline	4.25×10^{9}	2.25×10^{9}
	Vitreous	3.5×10^{9}	2.0×10^{9}
	Tap water	1.5×10^{9}	0.9×10^{9}

3.2 Plasma expansion and emission

A portion of the plasma expanding towards the focusing lens preferentially absorbs the laser energy, and this leads to the plasma elongation in this direction [3, 23]. In the condensed media (liquids and solids), it is believed that the mentioned plasma elongation arises from independent breakdown in multiple sites [21, 24] and that in the case of liquid media this causes cylindrical cavitation. The plasma elongation towards the laser source is particularly pronounced in liquids for picoseconds and nanosecond regimes and this effect is called “moving breakdown” [21, 24]. When moving breakdown occurs, the plasma heating is reduced in the focal volume due to plasma shielding at points farther up the beam path. As a consequence, both the plasma emission intensity and decay time are reduced [21].

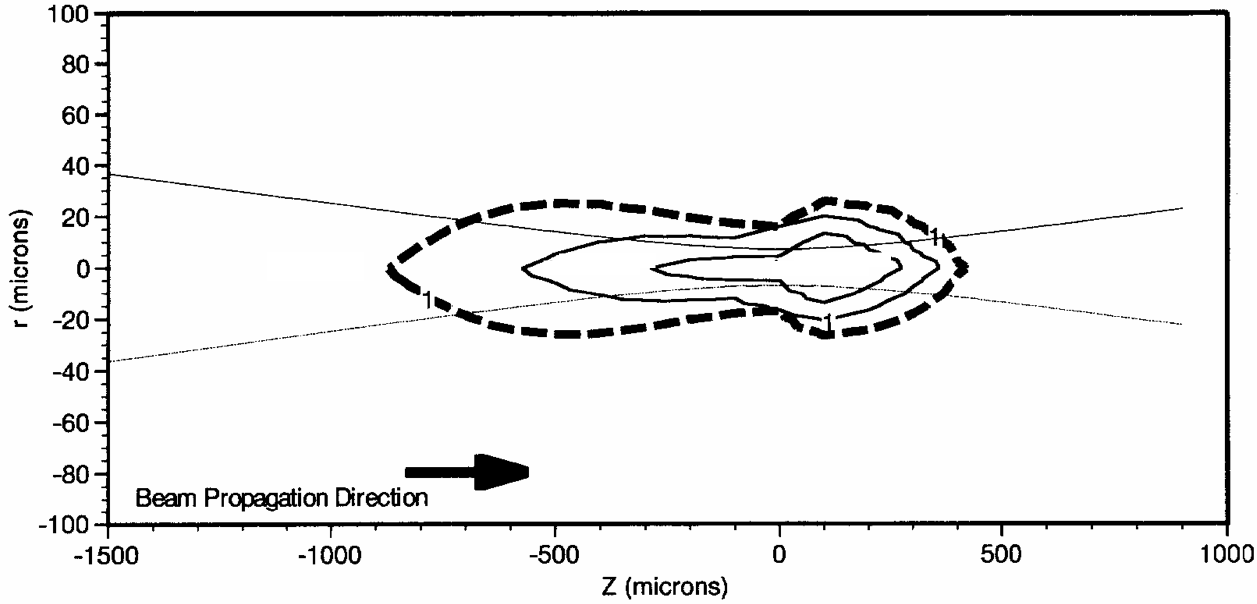

Figure 3.2: Simulated spatial plasma evolution for 10 ns, 532 nm laser pulse at delays 0 ns, 5 ns and 14 ns (dashed line) [3].

Larger focusing angle and smaller spot sizes produce smaller plasma but its transmission decreases down to a few percents [3].

In pure water, the laser exposure produces a single spark, while in tap water the formation of multiple, spatially distinct plasmas has been observed in nanosecond regime for irradiances far above the LIB threshold [21]. The plasma formation in multiple sites is considered to be triggered by impurities.

The continuum plasma emission in liquids exhibits approximately a blackbody spectrum [8, 25] described by formula:

$$I(\lambda,T)=\frac{I_0C_1}{\lambda^5\left[\exp(hc/\lambda kT)-1\right]} \tag{3.1}$$

Where T is the plasma temperature (K), h is Planck's constant, k is Boltzmann constant, C_1 is the constant with value 14388 µm^2. The position of the peak emission can be used to estimate approximately the plasma temperature, since the real temperature has spatial and temporal distribution. The external plasma layers have lower temperatures and also partially reabsorb the radiation from hotter plasma core. In the case of short laser pulses the plasma temperature is relatively low and the peak blackbody emission is shifted towards infrared.

Temporal behaviour of the broadband plasma emission can be described with a second order exponential decay function. It has been proposed [26] that the fast and slow components represent electron-ion recombination and electron attachment to neutral molecules, respectively. For nanosecond pulses in liquids, decay time of the slower component is in order of the pulse duration and increases with the applied pulse energy [11].

3.3 Bubble formation

High temperatures and pressures generated within the plasma cause the thermal adiabatically expansion in all the directions, which continues also after the end of the laser pulse. This expansion leads to a growth of a bubble containing water vapour and diffused gas at high temperature and pressure [3]. During the growth, the pressure inside the bubble decreases both due to the volume enlargement and to vapour condensation across the bubble-liquid interface. At the maximum bubble expansion the pressure is reduced at saturated vapour pressure of the liquid. Since the saturated vapour pressure is much lower than the pressure of surrounding liquid, the bubble starts to shrink until the rate of condensation can not offset the volumetric reduction. If enough energy is stored in the bubble, the collapse produces a rapid increase of the inside gas temperature and pressure, and this gives rise to a second shock-wave and to re-expansion of the bubble. The bubble oscillations may continue for many cycles of expansion and collapse [12]. The greatest loss of the bubble potential energy occurs during the collapse mainly because of the acoustic transient and heating of the surrounding liquid.

At the end of the collapse period the bubble might emit a short burst of light with duration in the picosecond to nanosecond range, called sonoluminescence [27-29]. It generally has a broad spectral emission [28-29] attributed to ion-electron recombinations occurring at the high temperature and pressure of the compressed bubble.

For nanosecond pulses LIB in liquids, the maximum measured bubble radius varied from 0.19 mm to 3 mm [3] with the expansion time from 15 μs to 325 μs. The time of the first bubble collapse is approximately twice larger. The maximum bubble radius increases with the laser energy and pulsewidths [25], and depends also on the focusing conditions [10, 30].

3.4 LIBS in liquids

Intensity of the plasma emission produced in bulk water is generally lower than at water-air interface due to several factors that include: water absorption of the laser and plasma emission and their scattering on suspended particles and micro-bubbles [31], radiation shielding by the high density plasma [21, 24] out of the focal volume and fast plasma quenching in the dense medium. The irradiance breakdown threshold is lower in air than for liquids [32] because a large amount of the input energy is required to vaporize liquids and a higher fraction of the incident laser energy is lost in mechanical effects [33]. The breakdown threshold for the submerged solid samples can be lower than for liquid itself and often the ablation rate of submerged solids is higher than in gas surrounding [34], explained by major mechanical scavenging. However, the LIBS signal at equivalent laser excitation still remains significantly lower than in the presence of sample-air interface. The emission lines from underwater plasma are strongly broadened by the high electron plasma density [35-36]. All the above mentioned effects lead to a relatively poor signal in a Single Pulse (SP) LIBS measurements [37-39], which does not allow for trace element detection.

Much better analytical performances of underwater LIBS could be obtained by applying a Double-Pulse (DP) laser excitation technique [35, 39-42]. In such case, the first laser pulse produces a cavitation bubble in water, while the second, probing pulse excites the plasma inside the bubble. After the second laser pulse, a relatively intense and narrow spectral emission can be observed due to gaseous state inside the bubble and consequently reduced plasma quenching and collisional broadening (Fig. 3.3) [42]. As a result, the LOD's below 1 ppm were obtained for some elements directly analyzed from bulk waters [39, 41], and in order of 100 ppm for different elements from submerged stainless steel samples [44].

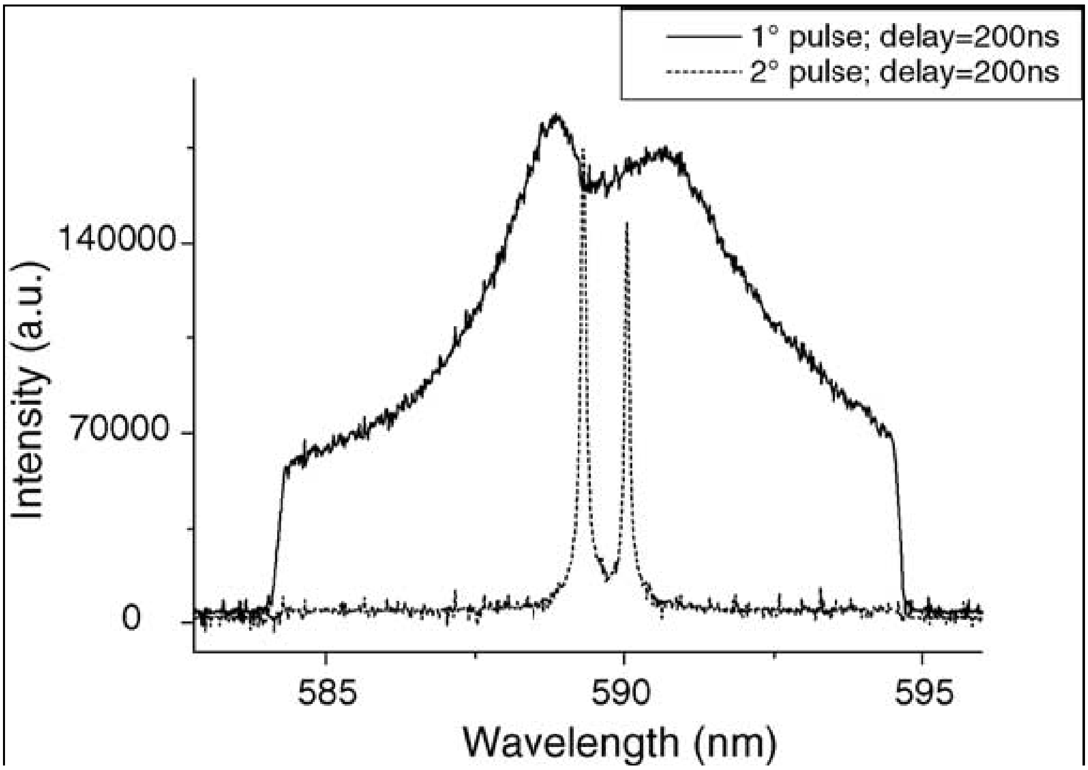

Figure 3.3: LIBS signal from sodium lines in tap water after applying single (solid line) and double pulse excitation [42]

An important factor to take into consideration for DP LIBS applied on bulk liquids or immersed samples, is the timing between the pulses. In ref. [9] the maximum LIBS signal was obtained if the second pulse irradiated the sample while the gas bubble produced by the first pulse, was at its expansion maximum. For this study the authors used two Nd:YAG lasers operated at 532 nm and performed ablation of Titanium metallic target underwater. The maximum bubble expansion was measured after 105 μs from the first laser pulse. For this interpulse delay, the LIBS signal after the second pulse was about two orders of magnitude higher than for delays corresponding to the smallest bubble radius (Fig. 3.4). Such behaviour of the LIBS signal has been attributed mainly to two factors: faster secondary plasma cooling and decay when triggered inside smaller bubbles with higher pressure, so with higher collision rates; to a lower transmission of the laser radiation to the target when the vapour pressure is higher i.e. the bubble is smaller. Measured spectral width of emission lines after the second pulse follows the gas pressure inside the bubble produced by the first laser pulse, where the minimum collision broadening corresponds to the maximum bubble expansion (Fig. 3.5). A similar behaviour was observed also for the plasma excitation temperature after the second laser pulse, where the spectra were integrated over 9 μs, so over the interval much longer than the continuum emission decay. This effect was explained by a more efficient late cooling of the secondary plasma through expansion in the case of large bubble above the sample surface.

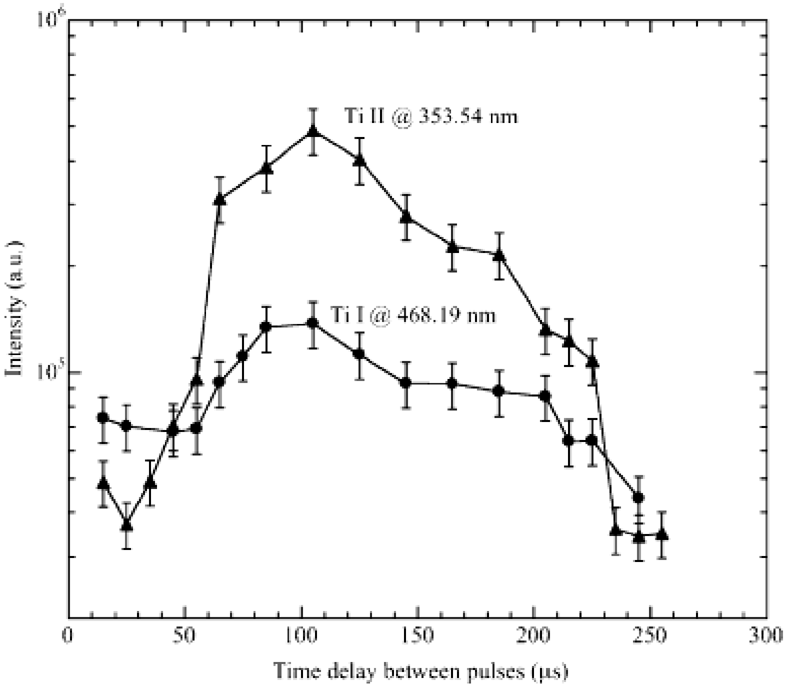

Figure 3.4: Intensity of Ti spectral lines after the second laser pulse as a function of delay between the two pulses [9]

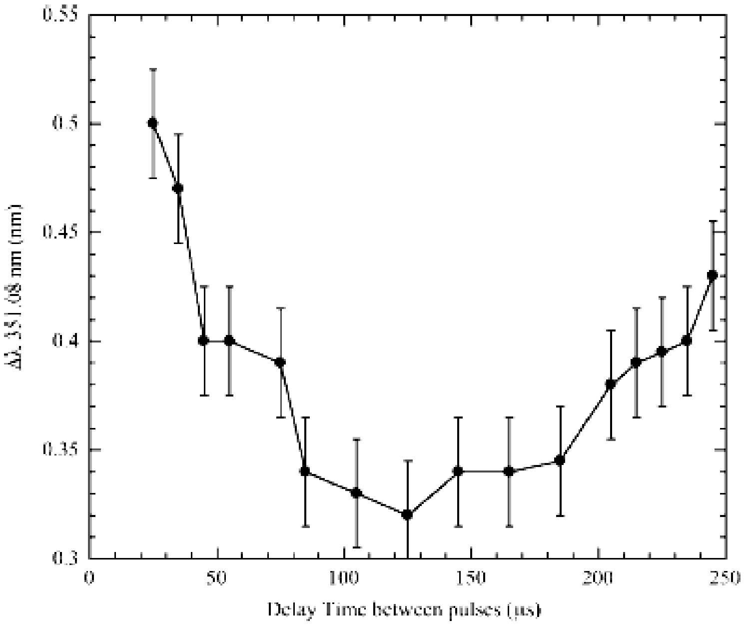

Figure 3.5: Width of Ti^+ spectral line as a function of delay between the two pulses [9]

3.5 References

[1] H. B. Bebb, A. Gold, Multiphoton ionization of hydrogen and rare-gas atoms, Phys. Rev. 143 (1966) 1-24.

[2] M. D. Perry, O. L. Landen, A. Szoke, E. M. Campbell, Multiphoton ionization of the noble gasses by an intense 10^{14} W/cm^2 dye laser, Phys. Rev. A 37 (1988) 747-760.

[3] P. K. Kennedy, D. X. Hammer, B. A. Rockwell, Laser-induced breakdown in aqueous media, Prog. Quant. Electr. 21 (1997) 155-248.

[4] M. Bass, H. H. Barrett, Avalanche breakdown and the probabilistic nature of laser induced damage, IEEE J. Quantum Electron. QE-8 (1972) 338-343.

[5] M. Bass, H. H. Barrett, Laser-induced damage probability at 1.06 micrometer and 0.69 micrometer, Appl. Opt. 12 (1973) 690-699.

[6] H. Schmidt-Kloiber, G. Paltauf, E. Reichel, Investigation of the probabilistic behaviour if laser-induced breakdown in pure water and in aqueous solutions of different concentrations, J. Appl. Phys. 66 (1989) 4149-4153.

[7] Q. Feng, J. V. Moloney, A. C. Newell, E. M. Wright, K. Cook, P. K. Kennedy, D. X. Hammer, B. A. Rockwell, C. R. Thompson, Theory and simulation on the threshold water breakdown induced by focused ultrashort laser pulses, IEEE J. Quantum Electron. QE-33 (1997) 127-137.

[8] P. A. Barnes, K. E. Reickhoff, Appl. Phys. Lett. 13 (1968) 282-284.

[9] A. Casavola, A. De Giacomo, M. Dell'Aglio, F. Taccagna, G. Colonna, O. De Pascale, S. Longo, Experimental investigation an modeling of double pulse laser induced plasma spectroscopy under water, Spectrochim. Acta Part B 60 (2005) 975-985.

[10] A. Vogel, S. Busch, K. Jungnickel, R. Birngruber, Mechanisms of intraocular photodisruption with picosecond and nanosecond laser pulses, Lasers Surgery Med. 15 (1994) 32-43.

[11] B. Zysset, J. G. Fujimoto, T. F. Deutch, Time-resolved measurements of picosecond optical breakdown, Appl. Phys. B 48 (1989) 139-147.

[12] A. Vogel, W. Lauterborn, Acoustic transient generation by laser-produced cavitation bubbles near solid boundaries, J. Acoust. Soc. Am. 84 (1988) 719-731.

[13] P. K. Kennedy, S. A. Boppart, D. X. Hammer, B. A. Rockwell, G. D. Noojin, W. P. Roach, A first-order model for the computation of laser-induced breakdown thresholds in ocular and aqueous media. II. Comparison to experiment. IEEE J. Quantum Electron. QE-31 (1995) 2250-2257.

[14] P. K. Kennedy, R. J. Thomas, G. D. Noojin, B. A. Rockwell, P. K. Kennedy, W. P. Roach, A first-order model for the computation of laser-induced breakdown thresholds in ocular and aqueous media. I. Theory, IEEE J. Quantum Electron. QE-32 (1996) 670-678.

[15] P. K. Kennedy, A first-order model for the computation of laser-induced breakdown thresholds in ocular and aqueous media. I. Theory, IEEE J. Quantum Electron. QE-31 (1995) 2241-2249.

[16] N. Bloembergen, Lser-induced breakdown in solids, IEEE J. Quantum Electron. QE-10 (1974) 375-386.

[17] A. Migus, Y. Gaudel, J. L. Martin, A. Antonetti, Excess electrons in liquid water: first evidence of a prehydrated state with femtosecond lifetime, Phys. Rev. Lett. 58 (1987) 1559-1562.

[18] D. Grand, A. Bernas, E. Amouyal, Photoionization of aqueous indole; conduction band edge and energy gap in liquid water, Chem. Phys. 64 (1979) 73-79.

[19] F. Williams, S. P. Varma, S. Hillenius, Liquid water as a lone-pair amorphous semiconductor, J. Chem. Phys. 64 (1976) 1549-1544.

[20] P. K. Kennedy, E. M. Wright, Q. Feng, K. Cook, D. X. Hammer, C. R. Thompson, J. V. Moloney, B. A. Rockwell, J. J. Druessel, A. C. Newell, Influence of pulse duration on mechanical effects after laser-induced breakdown in water, in "Laser-Tissue Interaction VII", S. L. Jacques Ed., SPIE Proc. 2681A (1996) 390-401.

[21] F. Docchio, P. Regondi, M. R. C. Capon, J. Mellerio, Study of temporal and spatial dynamics of plasmas induced in liquids by nanosecond laser pulses. 1: Analyses of the plasma starting times 2: Plasma luminescence amd shielding, Appl. Opt. 27 (1988) 3661-3668.

[22] A. Vogel, K. Nahen, D. Theisen, J. Noack, Plasma formation in water by picosecond and nanosecond Nd:YAG laser pulses – Part I: Optical breakdown at threshold and superthreshold irradiance, IEEE J. Selected Topics Quantum Electron. 2(4) (1996) 847-860.

[23] Y. R. Shen, The principles of Nonlinear Optics, John Wiley&Sons, New York (1984) 528-539.

[24] D. X. Hammer, E. D. Jansen, M. Frenz, G. D. Noojin, R. J. Thomas, J. Noack, A. Vogel, B. A. Rockwell, A. J. Welch, Shielding properties of laser-induced breakdown in water for pulse durations from 5 ns to 125 fs, Appl. Optics 36 (1997) 5630-5640.

[25] A. Vogel, J. Noack, K. Nahen, D. Theisen, S. Busch, U. Parlitz, D.X. Hammer, G.D. Noojin, B.A. Rockwell, R. Birngruber, Energy balance of optical breakdown in water at nanosecond to femtosecond time scales, Appl. Phys. B 68 (1999) 271-280.

[26] F. Docchio, Lifetimes of Plasmas Induced in Liquids and Ocular Media by Single Nd:YAG Laser Pulses of Different Duration, Europhys. Lett. 6 (1988) 407-412.

[27] D. Lohse, Sonoluminescence: inside a microreactor, Nature 418 (2002) 381-383.

[28] M. P. Brenner, Single-bubble sonoluminescence, Rev. of Modern Physics 74 (2002) 425-484.

[29] R. Hiller, S. J. Putterman, B. P. Barber, Spectrum of synchronous picosecond sonoluminescence, Phys. Rev. Lett. 69 (1992) 1182-1184.

[30] A. Vogel, S. Busch, U. Parlitz, J. Acoust. Soc. Am. 100 (1996) 148-165.

[31] N. F. Bunkin, A. V. Lobeyev, Influence of dissolved gas on optical breakdown and small-angle scattering of light in liquids, Phys. Letters A, 229 (1997) 327-333.

[32] D. A. Cremers, L. J. Radziemski, T. R. Loree, Spectrochemical analyses of liquids using the laser spark, Appl. Spectrosc., 38 (1984) 721-729.

[33] J. R. Wachter, D. A. Cremers, Appl. Spectroscopy 41 (1987) 1042-1048.

[34] S. Zhu, Y. F. Lu, M. H. Hong, X. Y. Chen, Laser ablation of solid substrates in water and ambient air, J. Appl. Phys. 89 (2001) 2400-2403.

[35] A. De Giacomo, M. dell'Aglio, F. Colao, R. Fantoni, Double pulse laser produced plasma on metallic target in seawater: basic aspects and analytical approach, Spectrochim. Acta Part B, 59 (2004) 1431-1438.

[36] A. Escarguel, B. Ferhat, A. Lesage, J. Richou, A single laser spark in acqueous medium, J. Quant. Spectrosc. Rad. Transfer, 64 (2000) 353-361.

[37] S. Koch, W. Garen, M. Müller, W. Neu, Detection of chromium in liquids by laser induced breakdown spectroscopy (LIBS), Appl. Phys. A 79 (2004) 1071-1073

[38] R. Knopp, F. J. Scherbaum, J. I. Kim, Laser induced breakdown spectroscopy (LIBS) as an analytical tool for the detection of metal ions in acqueous solutions, Fresenius J Anal. Chem. 355 (1996) 16-20.

[39] D. A. Cremers, L. J. Radziemski, T. R. Loree, Spectrochemical analyses of liquids using the laser spark, Appl. Spectrosc. 38 (1984) 721-729.

[40] L. St-Onge, E. Kwong, M. Sabsabi, E. B. Vadas, Rapid analysis of liquid formulations containing sodium chloride using laser-induced breakdown spectroscopy, J. of Pharmac. and Biomed. Analysis 36 (2004) 277–284.

[41] W. Pearman, J. Scaffidi, S. M. Angel, Dual-pulse laser-induced breakdown spectroscopy in bulk acqueous solution with an orthogonal beam geometry, Appl. Optics 42 (2003) 6085-6093.

[42] A. De Giacomo, M. Dell'Aglio, F. Colao, R. Fantoni, V. Lazic, Double-Pulse LIBS in water bulk and on submerged bronze samples, Appl. Surf. Sci. 247 (2005) 157-162.

[43] A. E. Pichahchy, D. A. Cremers, M. J. Ferris, Elemental analysis of metals under water using laser-induced breakdown spectroscopy, Spectrochim. Acta B 52 (1997) 25-39.

Chapter 4

LIBS ANALYSES OF IMMERSED SOLID SAMPLES

Abstract
Results of the LIBS feasibility studies for recognition of different solid materials immersed in seawater are presented here. The materials considered correspond to those that could be found in undersea archaeological sites. Data acquisition and processing were optimized for better signal control and in order to improve the detection threshold. Quantitative chemical analysis was also performed on submerged bronze samples.

4.1 Introduction

Since prehistoric times, the Mediterranean Sea coasts were densely populated, hosting numerous harbours and ports. In this area, ship traffic was intense from ancient times up to the modern age. Due to storms, accidents and naval battles, the Mediterranean Sea-bottom is rich in archaeological findings relevant to wrecked ships. To the richness of the underwater patrimony, submersed coastal small settlements and towns also contribute. Nowadays, modern acoustic instruments (e.g. scanning SONAR) are available and localization of the underwater relicts and ruins has become much easier than in the past. Nevertheless, the problem of recuperating only the most valuable findings and their discrimination from useless ballasts still remains and its solution necessitates a development of fast, in-situ screening techniques. An additional request for underwater recognition of the archaeological findings currently comes from the institution of numerous marine parks, where the submerged sites may be visited, either virtually or by diving. Also in this case, the objects present in the site must be catalogued and possibly restored underwater, especially when highly oxidized surfaces are encountered. Once again, analytical in situ techniques must be used to characterize the surfaces, preferentially during the cleaning action [1, 2].

The advantages LIBS [3–5] over other quantitative techniques for elemental analyses applicable on historical findings are mainly its low invasiveness, the possibility to perform in-situ measurements, and its high spatial discrimination and rapidity of analysis [6]. Development of new spectrometers with a sufficiently high spectral resolution and for simultaneous registering over wide spectral ranges (see section 2.2), enlarges a number of elements that can be contemporary detected. LIBS has been successfully applied to characterize different artwork surfaces in air, including marbles [7-8], pigments [6, 9-10], multi-layered ceramics [11-12] and metals [11]. The analytical capabilities of the technique when applied to underwater samples were significantly increased by the implementation of DP laser excitation (see section 3.5). Underwater detection of submerged metallic samples by DP LIBS has been demonstrated [13-14]. An alternative approach for a direct underwater recognition of some materials by LIBS has been proposed by Beddows et al. [15], where a gas flux was applied to create sample-air interface prior to the laser ablation. However, the described LIBS system is rather complex and can not be used for bulk water analysis or characterization of soft immersed materials (Chapter 6).

An Italian research project, named TECSIS (diagnostics and technologies and intelligent systems for a development of archaeological parks in Southern Italy) deals explicitly with development of innovative techniques suitable for submarine archaeology. In the framework of this project, laboratory experiments were carried out on various types of materials characterized by different levels of surface preservation, which were immersed in artificial seawater.

Different metals have been examined, since their qualitative analysis is of great importance to support the decision of recuperating the finding, namely the recognition of precious metals (gold, silver and their alloys) and to discriminate bronze artefacts from iron masses used for ballasts, working tools or ship construction. Quantitative underwater analyses of bronze samples were also attempted in view of the possibility of dating the objects, as the lead content varied along the ancient age [16]. Stone materials have also been considered, in particular the discrimination of marble from common calcareous stones, given the widespread use of marble both for architectonic elements and decorative objects in the classical period. Underwater recognition of wood has been also examined, considering that this type of material requires a special recovery procedure under controlled atmosphere in order to prevent fast destruction of the sample after its transfer in the air surrounding.

This chapter reports the results obtained on different kind of immersed solid samples, together with a discussion of the experimental laboratory set-up and the data analysis procedures. The optimization of the LIBS technique, aimed to increase the detection sensibility, has been performed both through the choice of experimental parameters and by an appropriate signal post-processing (Chapter 5). The results are also discussed in view of the specific problems relevant to submarine archaeology.

4.2 Experimental

The plasma emission was produced by a Q-Switched Nd:YAG laser (Quanta System, model Handy) operated at 1064 nm, with a repetition rate of 10 Hz and pulse duration of 8 ns. The laser QS trigger has been externally controlled in order to extract two laser pulses during the same lamp flashing. The laser pulse energies were varied by changing the time delay between the lamp trigger and the two QS triggers: t_1=145÷155 μs and Δt=55÷75 μs respectively). The maximum laser energy, summed over the two pulses, was 320 mJ at the maximum current through the flashlamp used here. With the maximum laser pumping, the first pulse appears for the first QS delay t_l of about 125 μs, however it becomes stable in terms of shot-to-shot energy oscillations, for delay of about 145 μs. Further increasing of delay t_l leads to a progressive increment of the first pulse energy, which reaches maximum for t_l=210 μs, while for t_l >270 μs it becomes again instable until disappears. Such behaviour of the first pulse can be explained by the limited duration of the current through the flashlamp (about 300 μs) and by the lifetime of the upper laser transition level (255 μs)[17]. These factors determine the maximum population of the upper laser level before the QS aperture. The observed pulse instabilities for short and for long t_l can be explained by the population inversion close to the lasing level before the QS aperture [17]. Furthermore, the minimum interpulse separation for which we observed the second laser pulse was Δt = 50 μs, which correspond to the time necessary to rebuild the population inversion after the first pulse at maximum laser pumping. As a consequence, when using the described laser source in DP regime, the choice of the QS delays (t_l and Δt) for which the pulses are stable, are limited by the next conditions:

1) $145\ \mu s \leq t_l \leq 270\ \mu s$
2) $(t_l + \Delta t) \leq 270\ \mu s$
3) $\Delta t \geq 50\ \mu s$

For a fixed pulse separation, the energy of both pulses could be changed simultaneously by regulating the current through the laser flashlamps (Fig. 4.1). At a fixed pumping level, the energy partition between two pulses depends both on t_l and Δt. Temporal separations between the triggers and corresponding laser energies, were optimized for the best optical signal characteristics on a given type of submerged target (Tab. 4.1).

The laser beam was focused on the sample surface by two plano-convex lenses with nominal focal lengths in air f_l=150 mm and f_2=25 mm. The second lens was directly mounted on a beaker wall, so its surface was in contact with the water. The resulting back focal length in water was about 40 mm. The use of two lenses allowed for tighter focusing, which is required in the case of bulk water analyses in-situ by the same system (see Chapter 8).

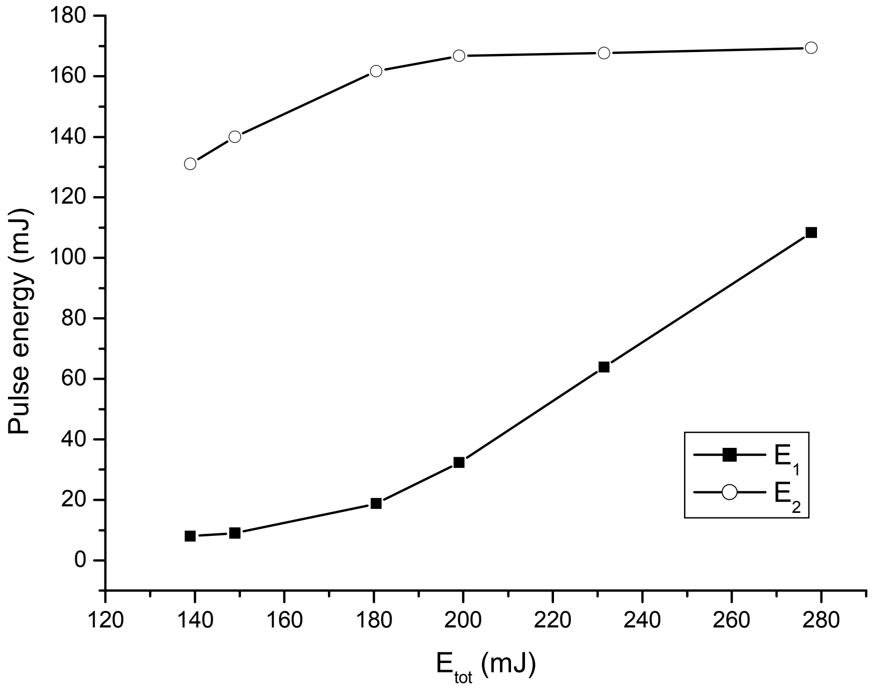

Figure 4.1: Energy of the first and second laser pulse as a function of the total laser energy, for QS delays t_1=150 μs (from the flash lamp trigger) and Δt=55 μs (interpulse).

The light emitted by the plasma in the spectral region 230÷750 nm was collected by a wide-angle receiver optics (full-angle aperture of about 11.3°), mounted at 90° with respect to the laser beam axis. The height of water column above the focal spot was about 20 mm. The collected signal was carried by an optical-fiber bundle, arranged into 0.1 mm wide fiber array the exit, to the entrance slit of a 550 mm monochromator (Jobin-Yvon, model TRIAX 550), equipped with three grating. In here described work a grating with 2400 grooves/mm was used. The corresponding wavelength intervals of about 10 nm were recorded at the monochromator exit plane by means of a gated ICCD (Andor Instaspec IV). The ICCD gate aperture was synchronized with the second laser pulse through an optical trigger brought to a delay generator. In this way, the spectral acquisition of the plasma emission could start exactly when the second laser pulse reaches the sample surface (delay 0) or could be suitably delayed [18]. Although the laser was running continuously, the QS triggers were generated only during the signal acquisitions, through a control trigger from ICCD. All the equipment was controlled by custom written software routines working in a Windows environment.

During a single measurement (at a fixed central monochromator wavelength), the spectra acquired after each laser shot were registered in separate columns inside a single file. This allowed on one hand the observation of shot to shot variations of spectral intensities and to discard the measurements showing crater effects or water transparency reduction, and on the other hand to apply a post-experiment data filtering procedure in order to improve the detection threshold. This procedure is described in details in chapter 5, together with a discussion of its advantages in the specific underwater application as well as in other LIBS analyses characterized by significant signal oscillations.

The set-up for underwater LIBS analysis is schematically drawn in Fig. 4.2.

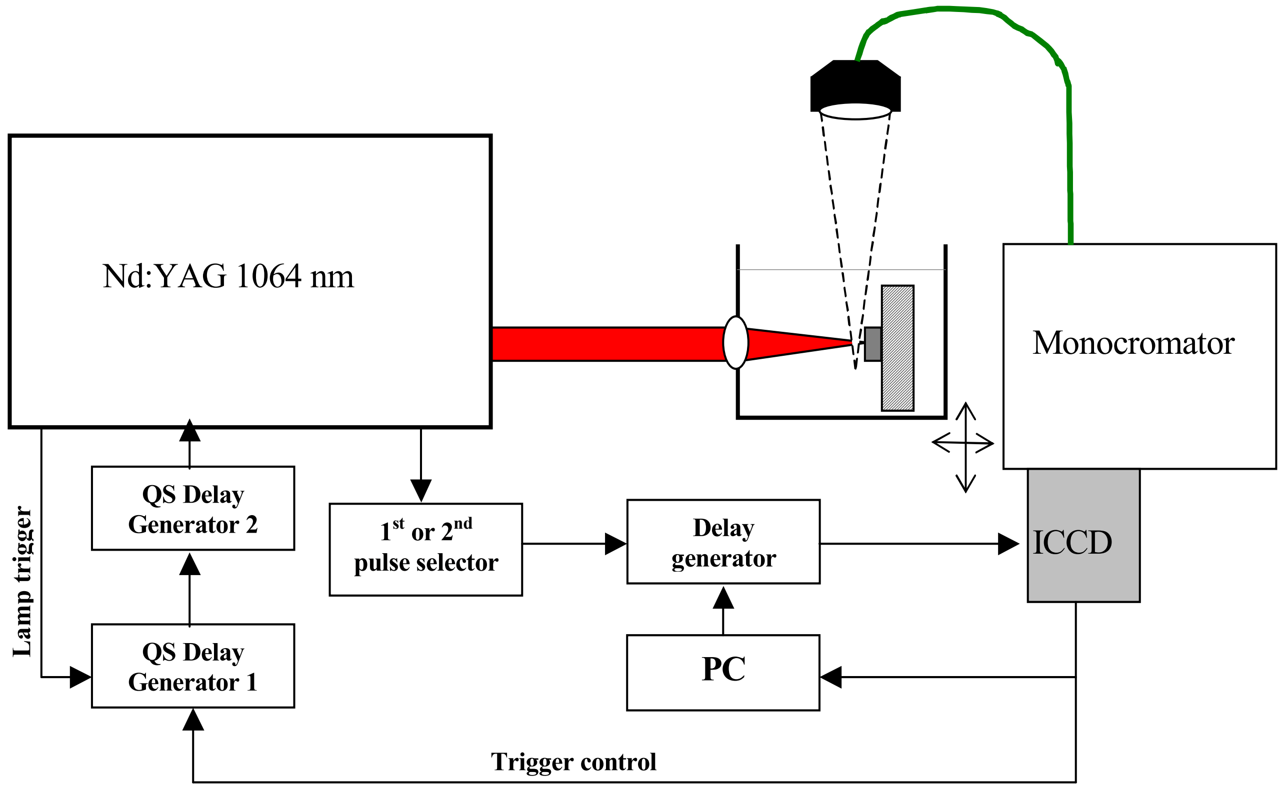

Figure 4.2: LIBS set-up for underwater characterization of solid materials.

The sample holder mounting allows for X –Y displacement in order to find optimal focusing and to expose a fresh target to the laser pulses. The measurements were performed both while moving the sample from one dual-pulse to another and at a fixed position, as discussed in the following section. For flat metallic samples the maximum LIBS signal intensity was found for the sample position before the lens focal point, corresponding to a spot diameter of approximately 300 μm and to a maximum fluency of about 450 J/cm^2.

The water used for immersing the samples was tap water to which NaCl salt was suitably added (29.3 g/l) to simulate seawater salinity. The water in the beaker was periodically exchanged in order to minimize scattering of the light from the previously ablated particles.

4.2.1 Samples

With aim to assess the analytical capabilities of the technique under optimum experimental conditions, LIBS analysis of submersed targets were first carried on clean, flat surfaces of homogeneous metal samples. However, in the case of real undersea measurements, corroded metals, and thus rough surfaces and in-homogeneous materials are expected. Therefore, the effects of surface roughness and sample inhomogeneity have been also examined through the measurements on non-metallic samples described in the next, and by sampling of a deeply corroded iron material.

The following immersed samples were analyzed:

1) A commercial stainless steel AISI 304, containing iron, 18–20% of Chromium, 0.75% of Silicon, 2% of Manganese, 0.08% of Carbon, 8–11% of Nickel, 0.04% of Phosphor and 0.03% of Sulphur. The examined sample had flat surface.

2) A commercial iron alloy C40, containing Manganese (0.5–0.8%), Carbon (0.37–0.44%), then traces of Chromium (<0.1%), Molybdenum (<0.1%) and Nickel (<0.1%). Measurements were performed both on a clean flat surface and on a strongly oxidized sample whose roughness and inhomogeneity are consequences of deep corrosion.

3) Five certified bronze samples with flat, non-oxidized surface, whose compositions are given in Table 4.2.

4) A flat area of commercial silver (900/1000) bracelet, with certified composition: 90% Silver and 10% Nickel.

5) A flat portion of a commercial gold 18 K bracelet, corresponding to Gold concentration of 75% and 25% of unknown elements.

6) A marble fragment (AKS1) from Proconnesos (Turkey), collected in one quarry utilized in ancient times [19], whose composition was determined previously [8]. The sample is naturally inhomogeneous and its surface is moderately rough after cutting.

7) A common calcareous rock extracted from seabed. The sample is naturally inhomogeneous and the examined surface area is almost flat.

8) A piece of an untreated wood.

9) Two samples of copper-based alloys with flat surfaces whose compositions were measured by SEM-EDX (Table 4.2).

Table 4.1 – Optimized experimental conditions for different materials.

Material	Trigger delays (μs)	Pulse energies (mJ)	Laser shots	Acquisition gate (ns)	Acquisition delay (ns)
Stainless steel	$t_1=150$, $\Delta t=55$	$E_1=120$, $E_2=160$	20	400	100
Iron - clean			20		
Bronze			20		
Corroded iron			100		
Precious alloys			1		
Marble, rock	$t_1=145$, $\Delta t=55$	$E_1=82$, $E_2=180$	50	600	200
Wood in air(*)	$t=210$	$E=300$	20	1000	500
Bronze – quantitative measurements		$E_1=52$, $E_2=140$	20	1000	800

(*) single pulse excitation

Table 4.2 – Composition (%wt) of standard bronze alloys used to build calibration curves.

Standard	Cu	Zn	Sn	Pb
B30	77.55	0.99	9.80	10.0
B4	83.7	1.38	11.10	2.54
LPb	88.14	0.47	9.78	0.79
HPb	82.47	5.86	5.29	5.55
CSM	90.12	0	7.9	1.8

4.3 Spectra and plasma characteristics

On different immersed samples, the LIBS spectra collected after the second laser pulse show sufficiently intense and resolved emission lines, useful for analyses.

Comparing the temporal emission of the plasmas produced on the same samples in air and in water surrounding, it could be observed that the plasma emission decay is about one order of magnitude faster in water than in air. Temporal behaviour of one Calcium line, measured on one clean marble sample (AKS1) in air surrounding (single pulse) and under water (DP excitation) is illustrated in Fig. 4.3. Here, SNR was calculated as a ratio of the line peak after the background subtraction, and standard deviation of the background close to the chosen line, with analogue spectral width. Similar results were obtained on iron sample, but the points on the analogue graph were less scattered due to better sample homogeneity and smaller surface roughness. On iron, the emission half-lifetime of Fe line at 291.2 nm was determined from an exponential data fit, and was about 500 ns, while on the ionic emission (Fe^+ at 285.8 nm) the measured half-lifetime was of about 200 ns (Fig. 4.4). The latter is shorter due to fast electron-ion recombination in plasma. Similar durations of the atomic and ionic emissions in underwater plasma have been also observed on other examined sample (metals and rocks). The strong plasma confinement and the consequent high density of species could explain the fast quenching of the plasma in water.

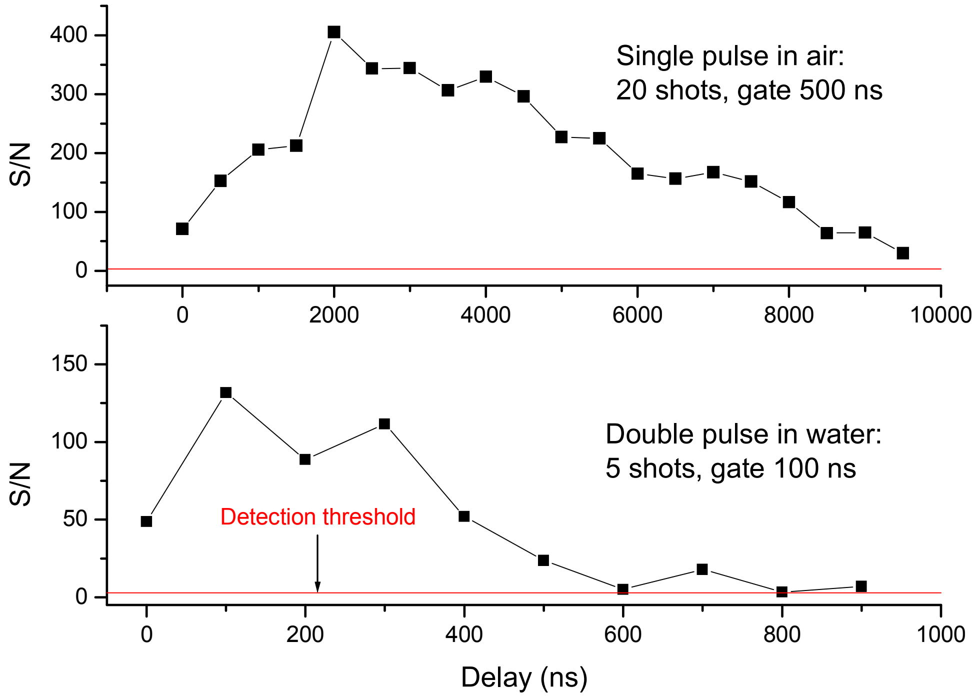

Figure 4.3: SNR of Ca line at 442.5 nm, measured by LIBS on a marble sample (AKS13) in air (single pulse, gate width 500 ns) and under water (double pulse, gate width 100 ns).

High plasma density underwater is also evident from the broadening of the emission lines caused by strong collision effects. The plasma parameters calculated from the LIBS spectra acquired on the steel sample in water (acquisition delay 100 ns and gate 400 ns) and in air (acquisition delay 2000 ns and gate 1000 ns), the latter under a single pulse excitation, were compared. Assuming the existence of LTE (see section 2.3), the plasma temperature was determined from Boltzmann plot relative to the non-resonant atomic Fe lines. The resulting plasma temperature was about (13000 ± 1400) K in water and (11000 ± 1200) K in air, and the differences can be attributed to a more efficient heating in dense media by inverse bremsstrahlung effect.

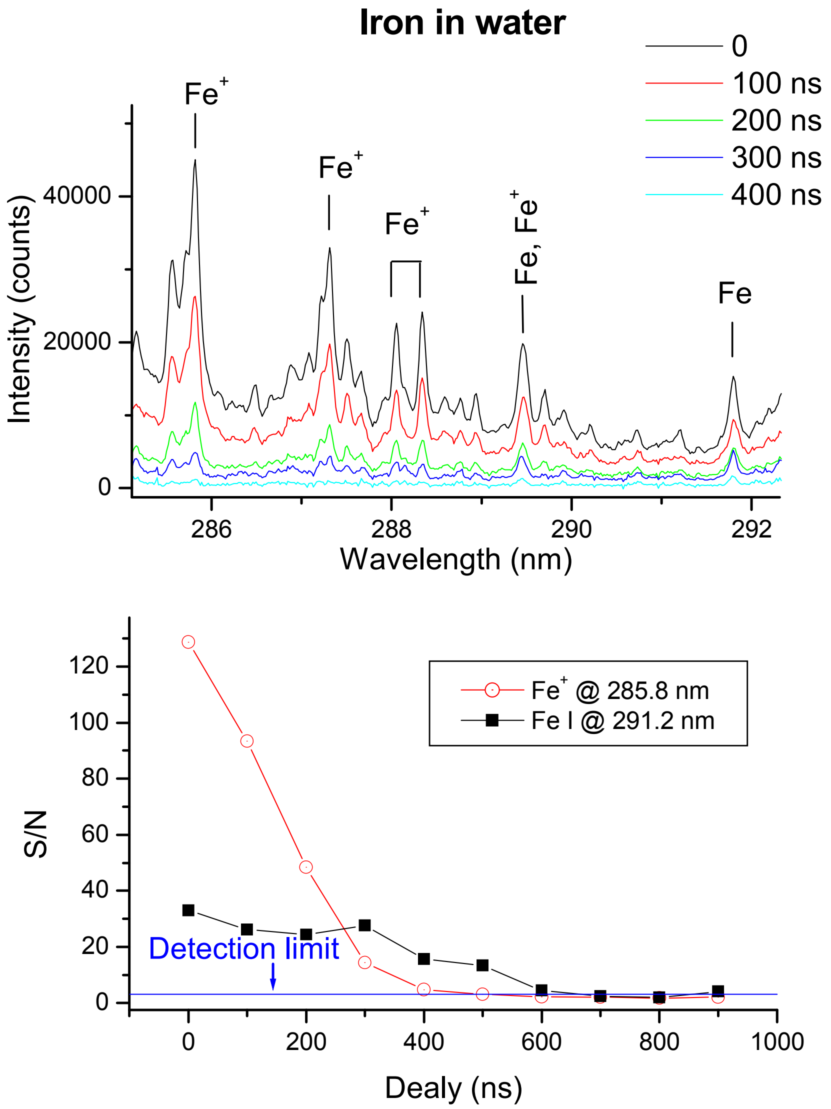

Figure 4.4: a) Portion of LIBS spectrum from immersed iron sample (DP excitation) and b) corresponding SNR of Fe line at 291.2 nm and Fe$^+$ line at 258.8 nm; gate width is 100 ns.

Knowing the plasma temperature, the electron densities were then estimated from Fe line at 538.3 nm [27-28] and result about (1.4 ±0.3)•10^{17} cm^{-3} in water and (7.5 ± 1.4)•10^{16} cm^{-3} in air.

In the spectra from the immersed samples, self-reversal was often observed for the resonant lines (see sections 2.3.4) due to the plasma cooling close to the gas bubble-water boundary [13]. Despite the high ablation rates of the submersed surfaces [20], the signals generated in water appear weaker than in air, also due to the short plasma duration. This is evident in Fig. 4.5 by observing the Ni atomic lines from the steel sample, which are well detected in air but close to the detection threshold under water.

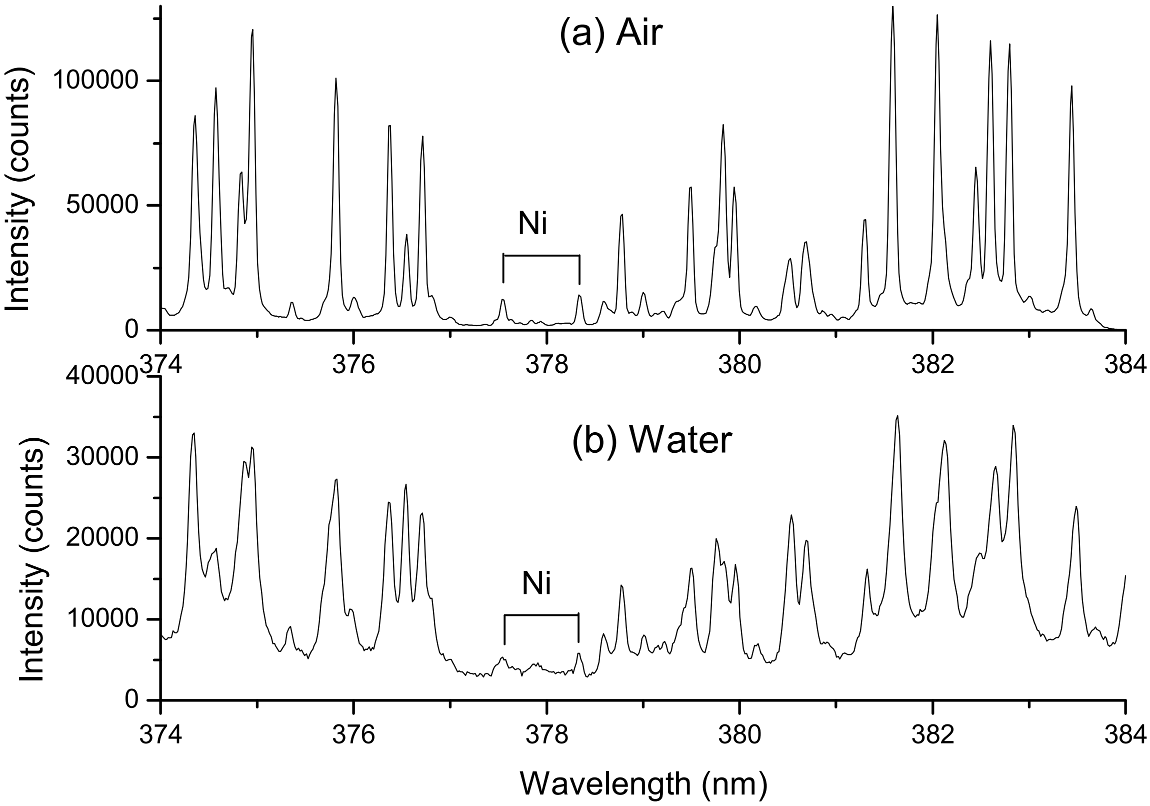

Figure 4.5: Section of LIBS spectrum from stainless steel AISI 304: a) SP excitation in air, E=300 mJ, 20 shots, gate 1000 ns, delay 2000 ns; b) DP excitation in water: E_1= 120 mJ, E_2= 160 mJ, 20 shots, gate 400 ns, delay 100 ns.

4.4 Recognition of metal alloys

With metal targets, the strongest plasma emission was achieved for pulse energies E_1= 120 mJ and E_2=160 mJ, corresponding to the trigger delays t_1=150 μs and Δt=55 μs (interpulse). The chosen acquisition delay was 100 ns, which was sufficient to avoid the most intense initial continuum emission and on the other hand, to start the acquisition while the plasma emission is strong and ionic species are still detectable. The acquisition gate was set to 400 ns after the optimisation with respect to the SNR ratio measured on different atomic emission lines.

4.4.1 Iron alloys

The spectra from the immersed clean iron sample C40 were obtained by summing the plasma emission over 20 shots. In addition to a number of Fe and Fe^+ lines (Fig. 4.6a), Mn was also detected (nominal values 0.5-0.8% wt) from its ionic triplet around 260 nm and its atomic emissions (Tab. 4.3), and Cr (guaranteed <0.1% wt) ionic (Fig. 4.6a) and atomic emission around 425 nm (Tab. 4.3). On the contrary, C (0.37-0.44% wt), Mo (<0.1% wt), and Ni (<0.1%wt) concentrations resulted below the detection limit in the current underwater experiments. A weak emission from Mg^+ (Fig. 4.3a) and Ca^+ around 390 nm (not reported) could be attributed to water impurities [14].

In order to check the detectability of other elements in an iron-based matrix, we also performed the measurements on the stainless steel sample. In this case, beside the elements mentioned above, also Ni (8-11%) was detected from the same lines as shown in Fig.4.5, but its strongest line intensities were found close to 340 nm. Si (2% nominal) atomic emission band around 250 was also well recognizable (not reported).

With the aim of simulating the undersea LIBS analyses on oxidized metals, measurements were also performed on a deeply corroded, rough iron piece. On the sample surface, the grain structures were visible to the naked eye and material in-homogeneities were evident also from colour changes from one point to another. Assuming that during in-situ experiments the laser-focusing lens would be separated from the surface by mean of a mechanical arm, the surface was interrogated by the laser both at fixed points and while moving slightly the sample in the focal plane. On the corroded iron, the signal was generally much lower than on the clean sample and the water transparency degraded rapidly due to the ablated particles, which further contributed to the laser beam and the signal attenuation. This effect drastically limits the possibility to acquire the signal over a large number of the laser shots. Much stronger shot-to-shot variations of the emission intensity were observed than in the case of the clean surface, also for the sampling at a fixed point (Chapter 5). On the corroded surface, such oscillations could be attributed to the material inhomogeneity and porosity, beside the randomness of the plasma formation. For the spectra acquired while moving slightly the sample, the plasma intensity oscillations were also caused by the surface roughness, particularly important for the short focal lengths of the focusing lens, as in our case here. The spectra summed over different shots (up to one hundred) allowed for Fe and Fe^+ detection. Moreover, after applying the data filtering procedure (Chapter 5), it was possible to detect two more minor elements like Mn and Cr.

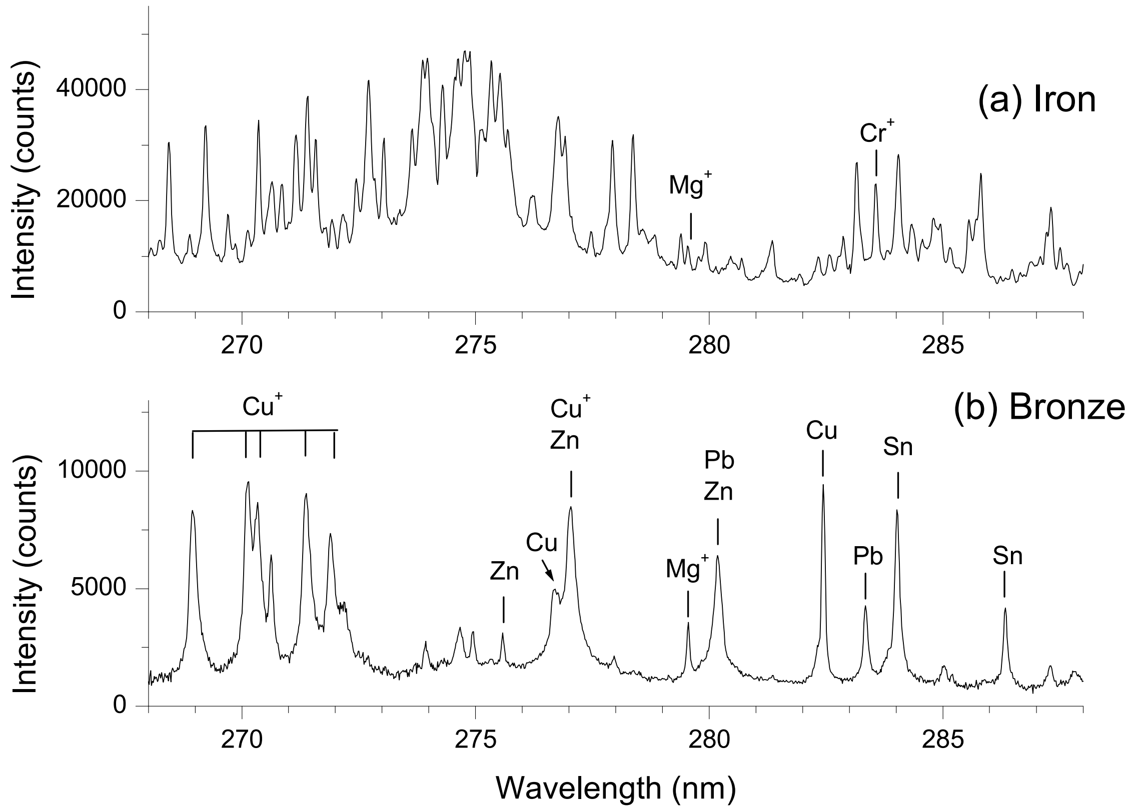

Figure 4.6: (a) Iron sample C40: detection of Fe atomic and ionic lines (unmarked peaks) and Cr$^+$; (b) bronze sample HPb: detection of Cu, Pb, Sn and Zn; Mg+ emission is attributed to water impurities.

4.4.2 Bronzes

A sample of standard bronze (HPb), with the composition similar to that utilized in Roman times for statues (82.47% Copper, 5.29% Tin, 5.55% Lead, 5.86% Zinc) [11, 21] was examined underwater. The spectra, summed over 20 laser shots, showed characteristic intense and well-resolved transitions (Figs.4.6b-4.7). All the four main elements forming the alloy were identified in a relatively narrow spectral range, i.e., 270-290 nm. However, the strongest Zn emission was observed around 470 nm (Tab.4.3) and this region should be used for the detection of concentrations lower than those reported here. In some cases, self-reversal was also observed (Fig.4.7). The plasma emission was sufficiently strong to allow the detection of some minor, non-certified elements, as for example Ni and Fe (Tab.4.3). The observed emission from Mg (Fig. 4.6b) and Ca around 390 nm (not reported) were again attributed to water impurities.

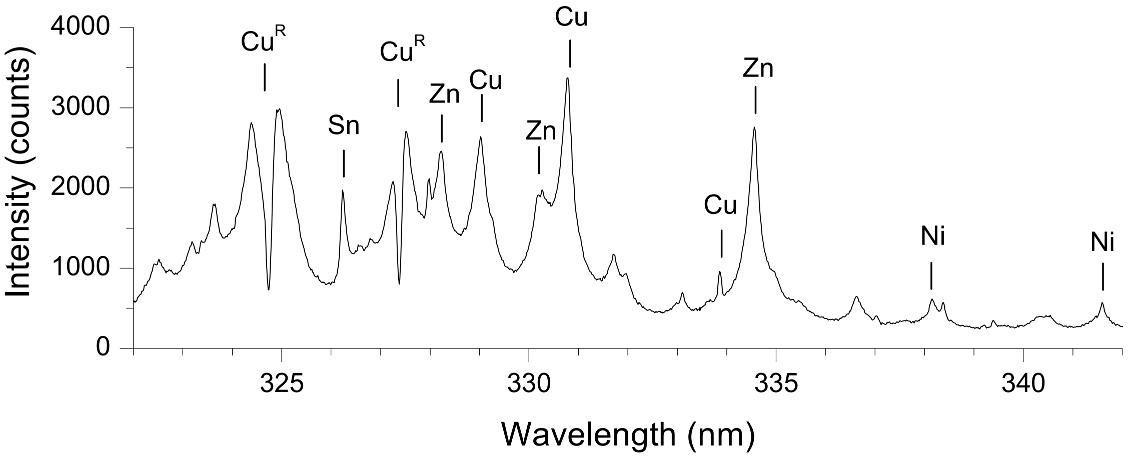

Figure 4.7: Bronze sample HPb: detection of Cu, Sn, Zn and of Ni impurity; lines denoted with the superscript ^{R} show self-reversal.

Table 4.3 – Element transition lines or bands (wavelengths in nm) used for underwater material recognition.

Elements	***Material***					
	Iron	**Bronze**	**Gold alloy**	**Silver alloy**	**Marble**	**Rock**
Fe	Different	$260^{+(b)}$	-	-	259.9^{+}	$260^{+(b)}$, $275^{+(b)}$, 302.5
Cr	283.6^{+},$425^{(b)}$	-	-	-	-	-
Cu	-	$270^{+(b)}$, 282.4, 465.1	$270^{+(b)}$, 465.1	-	-	-
Pb	-	283.3	-	-	-	-
Sn	-	284.0, 286.3	-	-	-	-
Zn	-	275.6, 468.0, 472.2	275.6, 277.1, 468.0, 472.2	-	-	-
Ag	-	-	276.8^{+}, 338.3	276.8^{+}, 272.2, 282.5	-	-
Au	-	-	274.8, 280.2^{+}, $282^{+(b)}$	-	-	-
Ni	-	338.0, 341.5	-	280.5, 282.1, 286.4^{+}	-	-
C	-	-	-	-	247.8	247.8
Ca	-	-	-	-	$300^{(b)}$, $458^{(b)}$	$300^{(b)}$, $458^{(b)}$
Mg	-	-	-	-	$280^{+(b)}$, 284.8	$280^{+(b)}$, 284.8
Si	-	-	-	-	251.6	$252^{(b)}$, 288.1
Al	-	-	-	-	308.2,309.3	308.2, 309.3
Mn	257.8^{+}, 259.3^{+}, 260.6^{+}, $476^{(b)}$, 478.3	-	-	-		257.8^{+}, 259.3^{+}, 260.6^{+}, $295^{+(b)}$
Ba	-	-	-	-	-	455.4^{+}
Sr	-	-	-	-	460.7	460.7

(b) = emission band around the specified wavelength; (+) = ionic emission

4.4.3 Precious alloys

The spectra of the precious alloys, being measured on jewels, were acquired by applying only one DP in order to avoid any visible damage on the surface. Despite a single shot acquisition, the spectra obtained both on the silver and gold alloys were very intense (Fig. 4.8). On the silver bracelet, different atomic and ionic emission lines from Silver (90%) and Nickel (10%) were detected (Fig. 4.8a). The presence of other elements could not be inferred from the spectra, apart from Mg and Ca impurities from water.

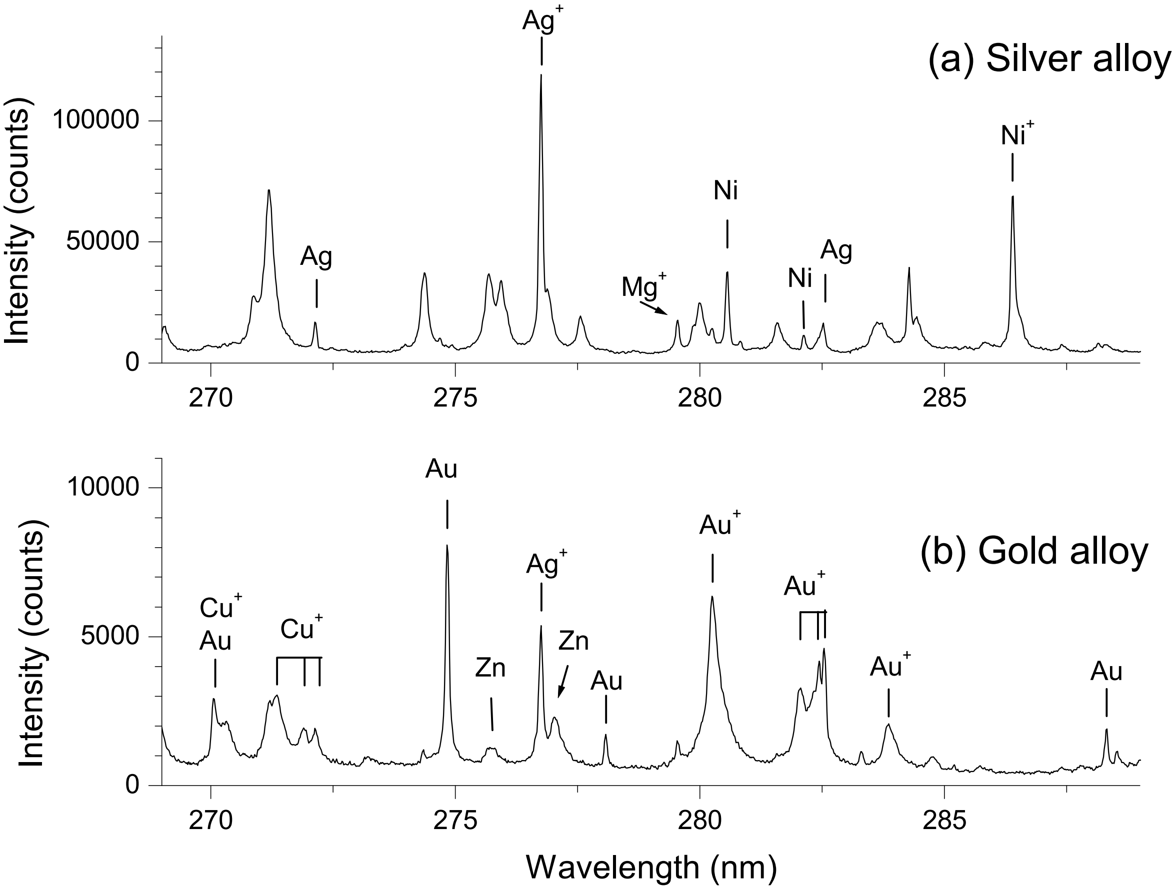

Figure 4.8: Recognition of precious alloys: (a) Silver alloy: atomic and ionic emissions from Ni and Ag; (b) Gold alloy: detection of gold (Au and Au^+), Copper (Cu^+), Zn atomic and Ag ionic emission; Mg^+ emission at 279.50 nm is attributed to water impurities.

The examined gold alloy had the composition certified only for gold (75% wt), while the other elements were unknown. Typically, Ag and Cu are added to the gold alloys used in jewellery, and frequently these alloys also contain Zn and/or Ni. Co or Fe could be also present as traces, as well as Ir or Rh, whose addition reduces the dimensions of the alloy grains. From the UV-VIS spectra, Au, Ag, Cu and Zn (Fig. 4.8b) were detected, the first three elements both from atomic and ionic emission lines. All the identified elements had emission line intensities largely above the detection threshold and, also in this case, they could be identified in the spectral range 270-290 nm.

4.5 Recognition of non-metallic samples

4.5.1 Stones

In the past, marble was extensively employed for sculptures and architectonic decorations. If the artistic shape of an undersea finding is not immediately recognizable, it is important to distinguish marble from non precious materials, as for example rocks. LIBS measurements have been performed both on a marble fragment, whose bulk composition (Ca 40.8%, C 12.2 %, Al 1.20%, Si 0.72%, Mg 6940 ppm, Fe 486 ppm, Ti 366 ppm, Cu 250 ppm, Mn 165 ppm, Ba 98 ppm) was known from previous measurements [8], and on a common calcareous rock extracted from the seabed. A similar composition for both marble and calcareous rock might be hypothesized, but a larger amount of impurities could be expected in the calcareous mineral. For of the considered stone samples, the optimal laser excitation required lower energy of the first pulse (E_1= 82 mJ, E_2=180 mJ) compared to the metal samples (Tab. 4.1). The interpulse delay was fixed to Δt = 55 μs, with the first pulse trigger being delayed to 145 μs from the flash-lamp trigger. The optimum acquisition gate was 600 ns and the gate delay from the second laser pulse was 200 ns. The data files were registered for 50 successive laser shots.

Although the ablation rates of the submerged stones resulted very high, the plasma emission intensities were surprisingly weak. The spectral intensities were much weaker for the clean, white marble than for the darker calcareous mineral, the difference being probably related to the better optical coupling of the near infrared laser radiation with the surface of the latter. Strong shot-to-shot oscillations were always observed and they are possibly caused by an intense ablation produced by the first laser pulse, which perturbs the plasma formation by the second pulse of the sequence [22]. The spectral signature from marble corresponds to its major constituents: Ca, C and Mg. Traces of Si and Fe (Fig. 4.9a), Al and Sr (Tab. 4.3) were also detected after applying the signal filtering. Note that Mg, and to a smaller extent Sr, are common calcium substitutes in calcium carbonate matrices.

The spectra from the rock sample showed the same main elements as the marble, but with more intense lines from Al and Sr. Also emissions from Si and Fe were significantly stronger than in the case of the marble and more lines from these elements were observed (Fig. 4.9b, Tab. 4.3). However, several other impurities were clearly identified in the rock samples, such as Mn and Ba (Fig. 4.9b, Tab. 4.3). While Si and Al are characteristic of alumino-silicates, Mn, Fe and Ba are usually present in the sedimentary rocks and are related to the past biological activity in seawater where the rock had been collected. When dealing with submerged archaeological samples, it is worth mentioning that the object surfaces might be covered by sedimentary layers originating from the precipitation of bioorganic materials through the water column. LIBS analyses of marine sediments and a comprehensible interpretation of the presence of different elements have been already reported [23].

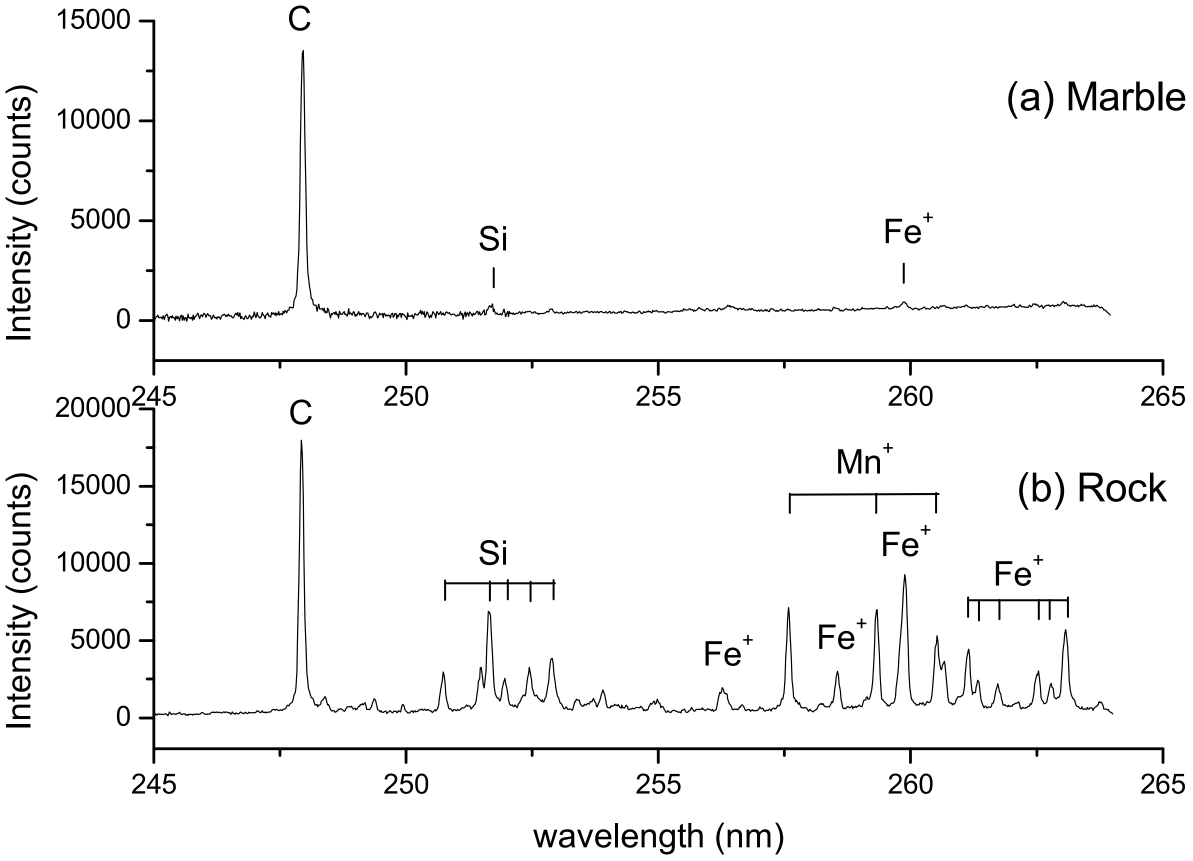

Figure 4.9: Comparison of underwater LIBS spectra from marble (a) and calcareous rock (b) in the spectral range 245 – 265 nm: identification of C, Si, Fe and Mn.

4.5.2 Wood

A submerged piece of untreated wood has been examined by LIBS using different pulse energy ratios and focusing distances. In all cases, ablation of the wood was not observed: even at the focal plane, the only emission observed was related to the breakdown in water. Probably, the ablation threshold of the wet, swollen, cellulose fibres is well above the maximum laser energy available in the present experiment. However, the same sample in air surrounding showed a very rich spectrum, where the following elements were identified: C, H, B, Mn, Fe, Mg, Ba, Ca, Sr, Al, Si and Na. An example of the wood spectrum in air, measured after a SP laser excitation at 1064 nm, is shown in Fig. 4.10. Other LIBS experiments on tree wood, carried on for dating of catastrophic events, gave similar results upon excitation at 355 nm in air [24]. In both cases a rich emission from molecular structures were observed and assigned to CN bands and C_2 Swan's bands.

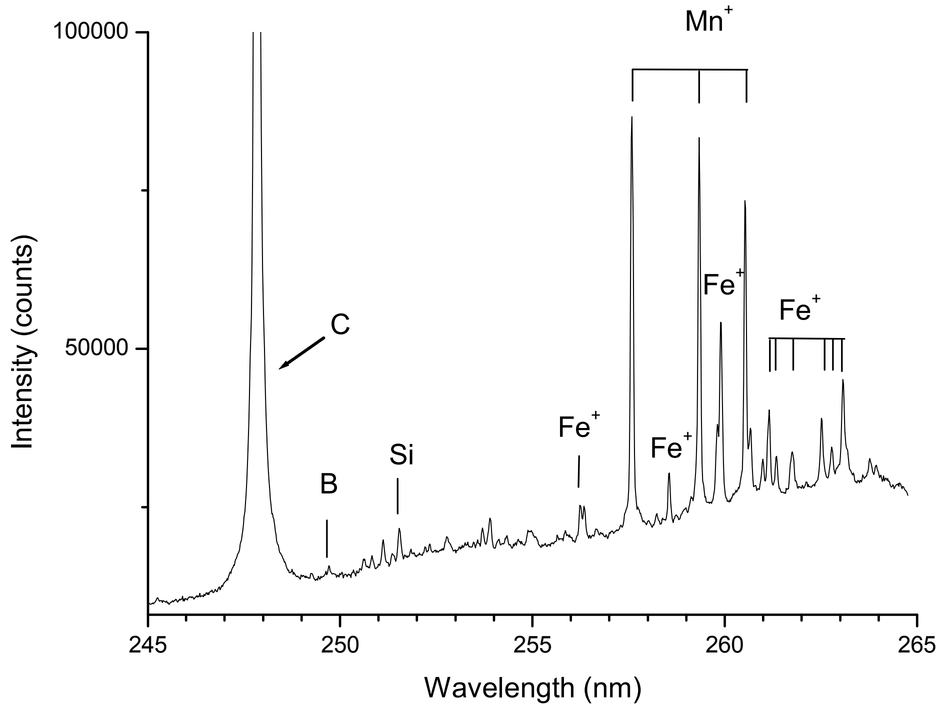

Figure 4.10: Portion of LIBS spectrum from a piece of wood in air by single pulse excitation, E= 300 mJ, acquisition delay 500 ns, gate 1000 ns, accumulation 20 shots.

4.6 Underwater quantitative analysis of copper alloys

Quantitative analyses of copper based alloys are considered important for dating of the archaeological findings. These chemical analyses were performed on two submerged copper-based samples, starting from the calibration curves generated for five submerged bronze standards whose compositions are listed in Tab. 4.2. In order to reduce the effects due to saturation of the lines, the laser pulse energies were reduced to E_1=52 mJ and E_2=140 mJ, while the acquisition delay and gate were set to 800 ns and 1000 ns, respectively. The measurements were performed by signal accumulation over 20 DP shots. Copper calibration was performed for the atomic line at 465 nm after its normalisation on nearby background emission, while the lines of other elements were normalised on this or on another Cu line (Tab. 4.3). Although such a calibration on quaternary copper alloys in air generally presents an irregular behaviour [25-26] due to the preferential vaporization of some elements (e.g. Zn), in the current underwater measurements all the calibration graphs showed a linear behaviour with acceptable correlation coefficients: 0.88 for Cu, 0.93 for Sn, and 0.999 for Pb (Fig. 4.11) and Zn. It might be hypothesized that a better stochiometry was achieved in the strongly confined underwater plasmas, but this argument needs more extensive studies.

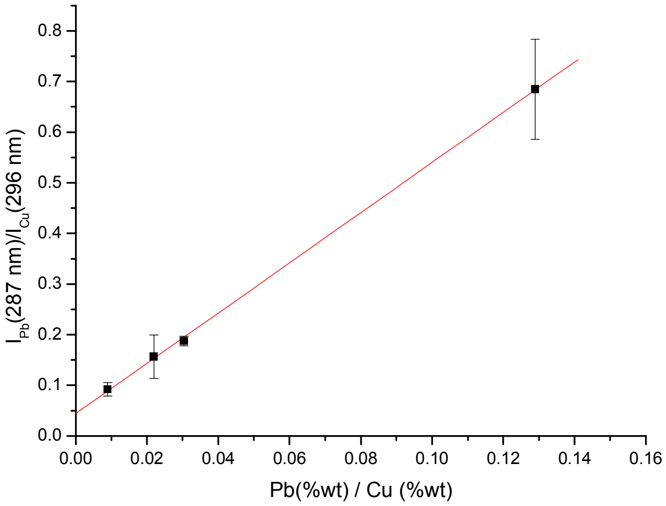

Figure 4.11: LIBS calibration used to determine Pb content of immersed copper alloys

Quantitative LIBS results are summarized in Tab. 4.4, where they are compared with SEM-EDX measurements performed on the same samples. We may notice an excellent agreement between the two analytical techniques obtained on the sample #1, which contains Cu and Sn. The comparison is less satisfactory for the other sample (#2): namely LIBS underestimates Cu by 15% and Zn by about 30%. Regarding the latter element in this sample, we must notice that the high value measured by SEM-EDX is largely out of our calibration range (see Tab. 4.2) and line saturation might occur, thus affecting the quantitative LIBS result. In the case of Pb, both by LIBS and SEM-EDX, strong concentration variations from one point to another were found and consequently, localized lead determination on such sample could not be considered affordable.

Table 4.4 – Results of quantitative analysis (%wt) by SEM-EDX and underwater LIBS for two different copper based alloys. Emission lines or their ratios used for quantitative LIBS analyses are also listed.

Sample	Element	EDX	LIBS	Analytical lines (nm)
# 1	Cu	82.6	81	465.1
# 1	Sn	5.8	5.8	Sn(286.3)/Cu(296.1)
# 2	Cu	50.9	59.6	465.1
# 2	Zn	31.8	23*	Zn(468.0)/Cu(465.1)
# 2	Pb	4.9	1.5**	Pb(287.3)/Cu(296.1)

(*) Out of calibration range
(**) Locally variable concentration

4.7 Conclusions

This work has demonstrated that dual-pulse LIBS can be used for in-situ, underwater recognition of different archaeological materials, having different states of surface roughness and preservation. The tests described were carried out both by sampling at a fixed point and while moving the sample. Plasma intensities under water present strong shot-to-shot variations in all the examined cases, particularly when dealing with in-homogeneous and/or rough surfaces, which are expected for undersea findings. The presence of ablated particles progressively reduces the water transparency, while crater development on the surface could further contribute to the fast signal degradation, particularly for high ablation rates which were observed on all the examined samples except wood. In these cases, better spectra characteristics were obtained by applying a limited number of laser shots and successive data filtering (see chapter 5), instead of spectra accumulation over a large number of laser pulses.

The main metal constituents of iron-, copper-, gold- and silver-based alloys could be identified in a relatively narrow spectral range (270-290 nm), while other minor elements could be also detected in different spectral segments. Successful identification of the minor elements (with concentration <0.1%) could supply important metallurgical information relative to the sample preparation and age. On flat metallic surfaces, single shot measurements were sufficient for the material identification. On corroded metals, the signal was lower than on clean surfaces and the detection of the minor elements required post- signal processing (chapter 5).

It has been also demonstrated that underwater recognition of marble material by LIBS is feasible, and the main spectral features necessary to distinguish it from matrix-similar calcareous rocks or sedimentary deposits, have been defined. On the other hand, laser ablation was not achieved on the untreated submerged wood with the available laser pulse energies. The same sample, analyzed in air, showed very rich spectra and revealed also some trace elements. The lack of ablation in the case of the immersed wood was attributed to the increased ablation threshold after wetting of the cellulose fibres.

Quantitative LIBS analyses of copper-based samples were also performed and further work should be carried out on a larger number of well-characterized samples.

4.8 References

[1] R. Pini, S. Siano, R. Salimbeni, M. Pasquinucci, M. Miccio. Test of laser cleaning on archeological metal artifacts, J. Cultural Heritage 1 (2002) 129-137.

[2] F. Colao, R. Fantoni, V. Lazic, L. Caneve, A. Giardini, V. Spizzichino, LIBS as a diagnostic tool during the laser cleaning of copper based alloys: experimental results, J. Anal. At. Spectrom., 19 (2004) 502 – 504.

[3] L. J. Radziemski, R. W. Solarz, J. A. Paisner (eds), Laser Spectroscopy and its Applications, Marcel Dekker, New York (1989).

[4] L. J. Radziemski, From LASER to LIBS, the path of technology development, Spectrochim. Acta B, 57 (2002) 1109-1113.

[5] D. A. Rusak, B. C. Castle, B. W. Smith, J. D. Winefordner, Fundamentals and applications of laser-induced breakdown spectroscopy, Crit. Rev. Anal. Chem. 27 (1997) 257-290.

[6] D. Anglos, Laser-Induced Breakdown Spectroscopy in Art and Archeology, Appl. Spectrosc. 55 (2001) 186A-205A.

[7] P. Maravelaki-Kalaitzaki, D. Anglos, V. Kilikoglou and V. Zafiropulos, Spectrochim. Acta B 56 (2001) 887–903.

[8] V. Lazic, R. Fantoni, F. Colao, A. Santagata, A. Morone, V. Spizzichino, Quantitative laser induced breakdown spectroscopy analysis of ancient marbles and corrections for the variability of plasma parameters and of ablation rate, J. Anal. At. Spectrom. 19 (2004) 429-436.

[9] D. Anglos, S. Couris, C. Fotakis, Laser diagnostics of painted artworks: laser-induced breakdown spectroscopy in pigment identification, Appl. Spectrosc. 51 (1997) 1025-1031.

[10] M. Martin, M. Castillejo, R. Torres, D. Silva, F. Guerra-Librero, LIBS spectra of polychromes with a low cost CCD camera based detector, J. of Cult. Heritage, 1 (2000) S293-S296.

[11] F. Colao, V. Lazic, R. Fantoni, V. Spizzichino, Laser-induced breakdown spectroscopy for semi-quantitative and quantitive analyses of artworks – application on multi-layered ceramics and copper based alloys, Spectrochim. Acta B 57 (2002) 1219-1234.

[12] Y. Yoon, T. Kim, M. Yang, K. Lee, G. Lee, Quantitative analyses of pottery glaze by laser induced breakdown spectroscopy, Microchem. J. 68 (2001) 251-256.

[13] A. De Giacomo, M. Dell'Aglio, F. Colao, R. Fantoni, Laser Induced Breakdown Spectroscopy in seawater, Spectrochim. Acta B 59 (2004) 1431-1438.

[14] A. De Giacomo, M. Dell'Aglio, F. Colao, R. Fantoni, V. Lazic, Double-Pulse LIBS in water bulk and on submerged bronze samples, Appl. Surf. Sci. 247 (2005) 157-162.

[15] D. C. S. Beddows, O. Samek, M. Liska, H. H. Telle, Single-pulse laser-induced breakdown spectroscopy of samples submerged in water using a single-fiber delivery system, Spectrochim. Acta B 57 (2002) 1461-1471.

[16] L. Robbiola, J.M. Blengino, C. Fiaud "Morfology and mechanism of formation of natural patinas on archaeological Cu-Sn alloys" Corrosion Sci. 40 (1998) 2083-2111.

[17] Koechner

[18] F. Colao, V. Lazic, R. Fantoni, S. Pershin, A comparison of single and double pulse laser-induced breakdown spectroscopy of aluminum samples, Spectrochim. Acta B 57 (2002) 1167-1179.

[19] http://venus.unive.it/termo/Marmi/BDMarmi.htm

[20] A. E. Pichahchy, D. A. Cremers, M. J. Ferris, Elemental analysis of metals under water using laser-induced breakdown spectroscopy, Spectrochim. Acta B 52 (1997) 25-39.

[21] P. T. Craddock, The composition of the copper alloys used by the Greek, Ertruscan and Roman Civilisations, J. of Archaeological Science 4 (1977) 102-123.

[22] V. N. Rai, F-Y Yueh, J. P. Singh, Study of laser-induced breakdown emission from liquid under double-pulse excitation, Appl. Optics 42 (2003) 2094-2101.

[23] R. Barbini, F. Colao, V. Lazic, R. Fantoni, A. Palucci, On board LIBS analysis of marine sediments Collected during the XVI Italian campaign in Antarctica, Spectrochim. Acta B 57 (2002) 1203-1218.

[24] F. Colao, R. Fantoni, D. Lattanzi, LIPS Analysis of samples of tree trunks, SPIE Proceedings Vol. 5850 (2005) 166-173.

[25] L. Fornarini, F. Colao, R. Fantoni, V. Lazic, V. Spizzichino, Calibration for LIBS analyses of bronze materials by nanosecond laser excitation: a model and an experimental approach, Spectrochim. Acta B 60 (2005) 1186-1201

[26] M. Gagean, J. M. Mermet, Study of laser ablation of brass materials using inductively coupled plasma atomic emission spectrometric detection, Spectrochim. Acta B 53 (1998) 581-591.

Chapter 5

IMPROVEMENT OF THE LIBS SIGNAL BY DATA PROCESSING

Abstract
Results of the post-measurement data processing, aimed to increase Signal-to-Noise Ratio are discussed. The considered data are relative to the LIBS spectra from immersed solid samples with different grades of surface roughness and material homogeneity, and from bulk water solutions.

5.1 Introduction

One of the main limitations of LIBS for underwater analyses of solid targets is related to its relatively low sensitivity. LOD's of the order of 100 ppm were reported for different elements from submerged stainless steel samples [1]. Improving the LOD is particularly important for the detection of trace elements and for system miniaturization. Increasing the laser energy far above the ablation threshold in order to obtain better SNR is limited by the laser performance. The benefits of accumulating the signal over a large number of laser shots are intrinsically limited and a saturation of SNR after about 50 laser shots was reported [2]. In the case of under water analysis of solid targets, a strong ablation by the first pulse could perturb the secondary plasma formation [1], and signal accumulation over a large number of laser shots could be limited by progressive increase of water turbidity, due to the presence of ablated particles. The use of short focal length lenses, with a short focal depth, could further reduce the LIBS signal on rough solid samples due to imperfect sample positioning.

Extreme LIBS signal intensity variations at the shot-to-shot level has been observed in many experiments [2-7]. Significant oscillations of the plasma temperature and electron density were also found in LIBS analyses of homogeneous glass samples in gas surrounding [3]. There numerous potential causes for the LIBS signal instabilities, including laser fluctuations, local variation of the sample properties (composition, surface roughness, grain size, impurity/bubble concentrations in liquids), scattering on particles/aerosols or bubbles in liquids etc. All these instabilities affect the process of the plasma formation, so they are responsible for changes in the plasma profile, volume and its parameters [2-3]. It was found that the laser instabilities, which are usually inside 1-5%, play only a minor role in the LIBS signal variations [4]. In order to increase SNR and the accuracy in LIBS quantitative analyses, usually the signal is accumulated over a certain number of the laser shots. An improved accuracy could be also obtained by removal of anomalous single-shot spectra [7].

In this chapter, the results of studies relative to shot-to-shot LIBS spectral behaviour are presented. First, the signal behaviour was examined on a flat steel sample immersed in seawater, at different sets of laser pulse energies. Then, the measurements were performed on two samples that could be found in marine archaeological parks – marble and corroded iron. These samples are strongly inhomogeneous and exhibit rough surfaces. The aim of this work was to increase the SNR through post-measurements signal processing, thus allowing for the material identification, including the detection of minor elemental constituents. The lowering of the detection threshold was also considered in view of a miniaturization of the LIBS apparatus for in-situ analyses, which requires small-size laser sources. Chosen approach to the signal improvement was to first study the influence of the low intensity spectra on the SNR. Although the elimination of weak spectra is often used prior to data analysis and sometimes mentioned [4, 7], a systematic study addressing its application to LIBS and in particular, to underwater LIBS analysis has not yet been reported.

After satisfactory results obtained on the solid samples underwater, the developed procedure was also applied to LIBS measurements on water impurities. Here, the preliminary tests were made on a magnesium containing solution at two sets of pulse energies, while more detailed studies are reported in chapter 7.

Other LIBS applications that could benefit from the proposed data acquisition and processing procedure are shortly discussed.

5.2 Experimental

5.2.1 Laboratory set-up

The experimental set-up for underwater LIBS experiments is fully described in section 4.2.

The measurements on the solid targets were performed both at a fixed position and while moving the sample, as it will be discussed later. The solid samples were fixed on a mechanical arm with vertical adjustment mounted on an X-Y table. The samples were immersed in tap water to which NaCl salt was properly added (29.3 g/l) to simulate seawater salinity. The water in the beaker was periodically exchanged in order to reduce the influence of the ablated particles on the LIBS signal.

In the case of measurements on solutions, position of the collecting optics was slightly changed in order to maximize the LIBS signal for the lowest solute concentration. This position corresponds to the detection region centred at the laser focal point in water.

5.2.2 Samples

In the LIBS analysis of submerged solid targets, both flat homogeneous samples and rough inhomogeneous sample surfaces were considered. The latter surface type is a simulation for what could be found in undersea archaeological parks, as for example corroded metallic surfaces and stones.

The details of the considered samples, listed below, are already described in section 4.2:

1) A commercial stainless steel AISI 304 sample with a flat surface.
2) A corroded piece of iron, whose roughness and inhomogeneity are due to deep oxidation.
3) A marble fragment (AKS1) from Proconnesos (Turkey) collected in one ancient quarry, whose composition was measured in a previous work [8]. The sample is naturally inhomogeneous and its surface is moderately rough.

In addition to the solid samples, a solution containing magnesium in different concentrations was analyzed by LIBS. The solution was prepared from $MgSO_4$ dissolved in high purity (milli-Q) water. Mg concentrations varied between 5 mg/l and 500 mg/l.

5.2.3 Data acquisition and signal processing

For a single measurement, at one fixed wavelength setting of the monochromator, the spectra acquired at each laser shot were recorded in separate columns inside a single file. This approach allows observing shot to shot variations of the spectral intensities, and is also useful for rejecting measurements affected by the crater effect or by a reduction in water transparency. On the other hand, separate spectrums' recording has some disadvantages, as for example the increase of ICCD readout noise, particularly for non cooled detectors, and large data file dimensions.

From single registered files, the data processing program operates in the following way:

1) For each acquired spectrum in one file, the program finds the intensity maximum, which corresponds either to the strongest emission line in the measured spectral range, or to the maximum background intensity in absence of any line emission , or to the maximum noise level, in absence of breakdown.
2) Among the registered spectra in one file, the program selects the one with the highest maximum intensity (I_{max}) - this column represents the reference data.
3) Inside the same file, the program selects other spectra whose maximum intensities are above threshold intensity, set at a given percentage of the maximum in the reference spectrum.
4) All the spectra characterized by a maximum intensity above such threshold are then summed and saved for further analysis.

This data filtering procedure is wavelength independent and was used for spectra acquired at different central monochromator wavelengths and on various immersed samples, characterized by different spectral features. However, the variable continuum emission intensity also contributes to the spectral maximum. In the case of weak correlation between the continuum and the plasma line emission (see section 7.5), better results from the data processing could be expected if the filtering is performed with respect to the peak emission from a chosen line. For this reason, the data acquired at a fixed monochromator position, such as in the case of water solutions, were processed considering the peak intensity of the selected analytical line (Mg^+ line at 279.5 nm) instead of the spectral maximum. The reference intensity over a single measurement was then the spectrum with the highest detected analytical peak (P_{max}) after background subtraction. Filtering at, for example, 10% level corresponds to rejecting all spectra characterized by an intensity of the selected peak lower than 0.1 P_{max}, while the remaining spectra are automatically summed and saved into a new file.

The data filtering software and SNR analyses of the new resulting spectrum at a single monochromator position were developed under LabView. The software rapidly elaborates all the data from a chosen directory. The program includes an option for linear fitting of the maximum (or peak) spectral intensity as a function of the shot number, and whenever this fit shows an important decaying trend, the data file can be automatically discarded.

5.3 Results on immersed solid samples

5.3.1 Stainless steel

For the SNR studies on the stainless steel sample, the spectra were acquired for successive 100 laser shots, with a gate delay of 200 ns after the second laser burst and an acquisition temporal window of 600 ns. The QS trigger delays were fixed to t_1= 150 μs (from the flash lamp trigger) and Δt = 55 μs (interpulse delay). The effects of the signal filtering were studied for different total laser pulse energies, whose partition between the first and second laser bursts is reported in Fig. 4.1. The samplings were performed both at the fixed position and by moving the target along the focal plane. At increasing laser energy, the spectral intensity fluctuations are progressively reduced, as well as the number of missing breakdown events. In the case of measurements performed while moving the sample manually, the data filtering, here applied with respect to the maximum spectrum intensity, improves the SNR only for the lowest pulse energies used: its effectiveness at E_1=8 mJ and E_2=131 mJ is shown in Fig. 5.1. For different measurements, a common optimal filtering range could be defined, although the statistical intensity distribution might change from one measurement to another. Differences in the distribution may be caused by various factors, e.g., presence of gas bubbles and ablated particles, laser instabilities, unsteady movement velocity and imperfect sample positioning with respect to the focal plane, which is particularly important when using a lens with a short focusing length.

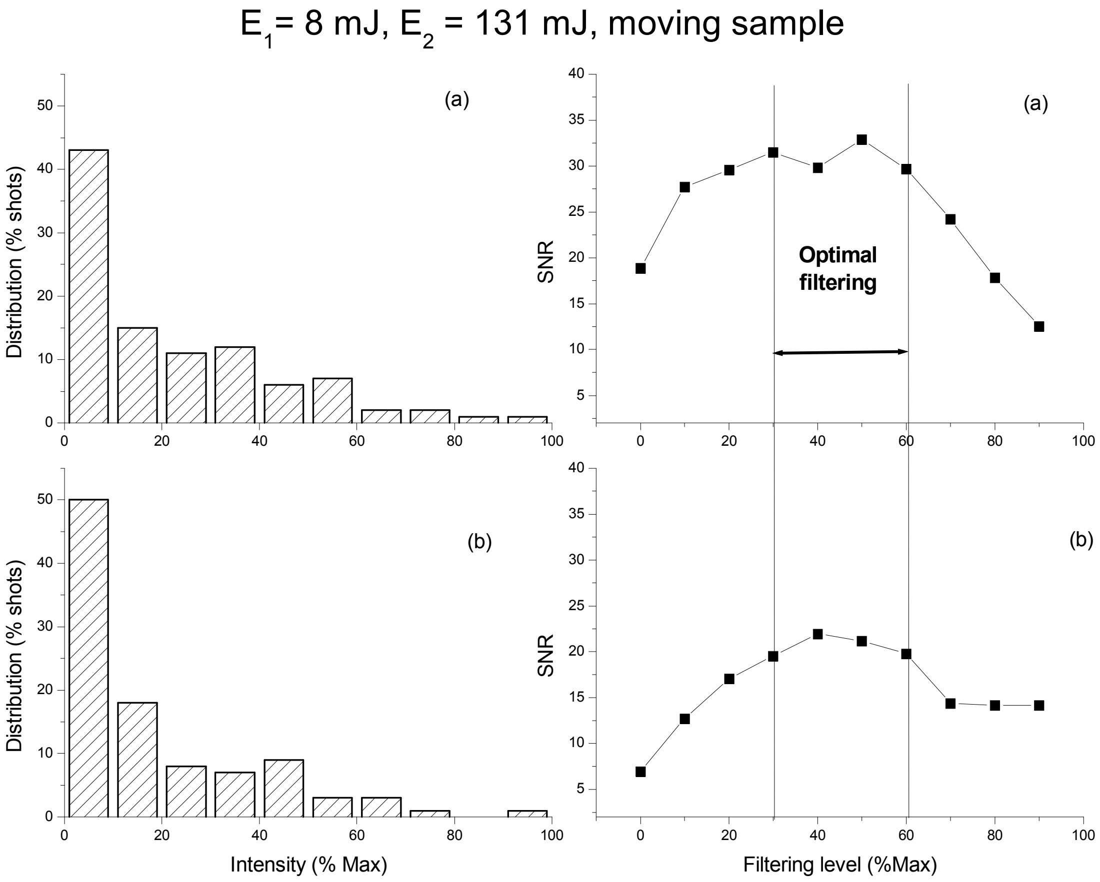

Figure 5.1: Statistical intensity distribution (left column) and SNR for Cr line (480.1 nm) at different filtering levels, for two replicated measurements (a, b) on the stainless steel sample in movement; laser pulse energies are E_1=8 mJ and E_2=131 mJ in both cases.

For sampling at a fixed position, the spectral intensity fluctuations are more severe and in this case the data filtering may bring some SNR improvement also at high laser energies (Fig. 5.2). Furthermore, a crater development was sometimes inferred from the progressive signal reduction observed during a single measurement (Fig. 5.2b). In this case, the data filtering at a low 10% level can always be useful to eliminate automatically the low intensity spectra due to the crater formation on the sample surface, as well as due to the progressive degradation of the water transparency. The latter effect must be considered in all LIBS underwater measurements on solid samples.

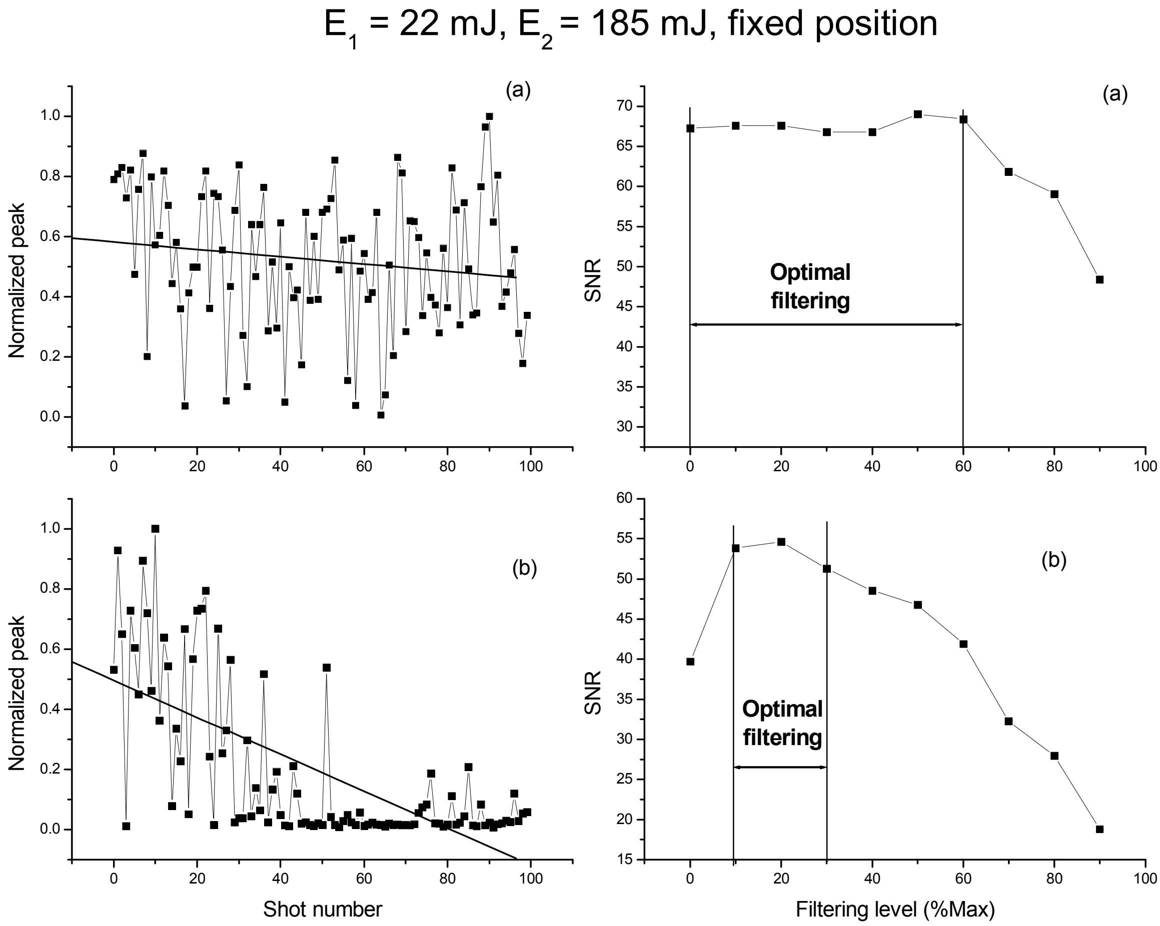

Figure 5.2: Shot-to-shot variation of normalized maximum spectral intensity in the range 474-484 nm (left) and SNR of Cr line (480.1 nm) at different filtering levels (right), measured on the steel sample over 100 shots at fixed position: (a) normal distribution; (b) signal reduction due to the crater effect and/or induced water turbidity.

5.3.2 Analyses of corroded iron

The measurements described in the previous section were performed on a flat, homogeneous sample. However, for in-situ underwater analysis of findings in undersea archaeological parks, the presence of rough surfaces and inhomogeneous samples is expected. As an example of the real undersea samples, we considered a deeply corroded, rough iron piece. The material was evidently inhomogeneous, with colour differences from one point to another and the presence of grains visible with the naked eyes. Two ways of the LIBS sampling were performed, either at a fixed point or moving slightly the sample in the focal plane. On the corroded iron, the LIBS signal was generally very low and the ablated particles rapidly reduced the water transparency, which further decreased the spectral intensities due to the attenuation of both laser beam and signal. For this reason, in absence of water flushing, as it was the case in the present experiment, it was not possible to increase the number of laser shots for the signal acquisition, which was again fixed to one hundred. Here, the measurements were performed by applying the maximum laser energy available for given QS delays (E_1= 120 mJ, E_2=160 mJ), and the acquisition gate delay and width were set to 100 ns and 400 ns, respectively.

For this corroded sample, much stronger shot-to-shot emission intensity variations were observed (Fig. 5.3) than in the case of the flat steel sample (Fig.5.2a), and this might be explained by the material inhomogeneity and porosity. By slightly moving the sample during the signal acquisition, the plasma intensity oscillations (Fig. 5.3b) were also caused by the surface roughness, and the latter effect must be considered particularly severe when using a short focal length lens.

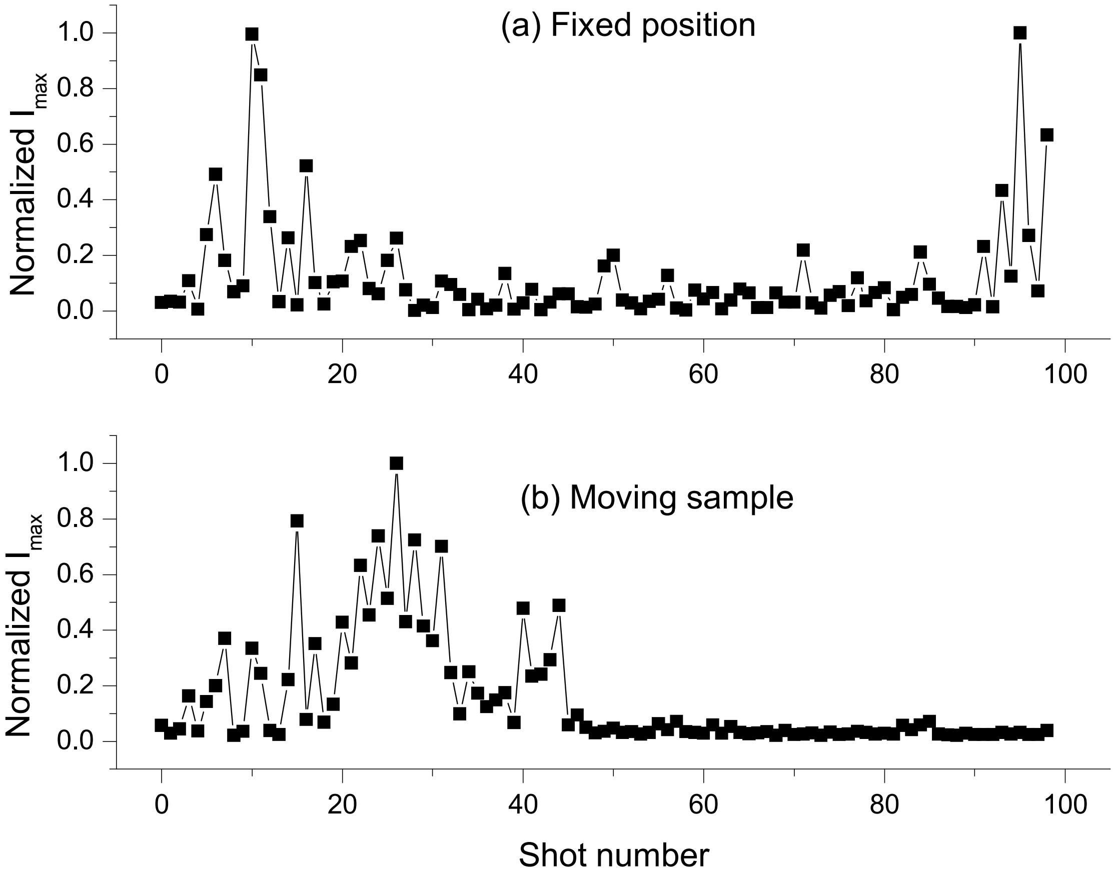

Figure 5.3: Shot-to-shot variation of normalized maximum spectral intensity in the range 372-382 nm, measured on the corroded iron sample: (a) at fixed position; (b) moving the sample.

The spectra summed over different shots were characterized by a low SNR (Fig. 5.4a). The results could already be improved by eliminating the spectra with the maximum intensity below 10% of the reference maximum (Fig. 5.4b). Although the statistical intensity distributions changes significantly from one measurement to another, in all the cases examined, filtering at the 10% level gave better results than the indiscriminate summing of spectra. In most cases, filtering at the 50% level was optimal (Fig. 5.4c) improving the SNR by a factor 3.6.

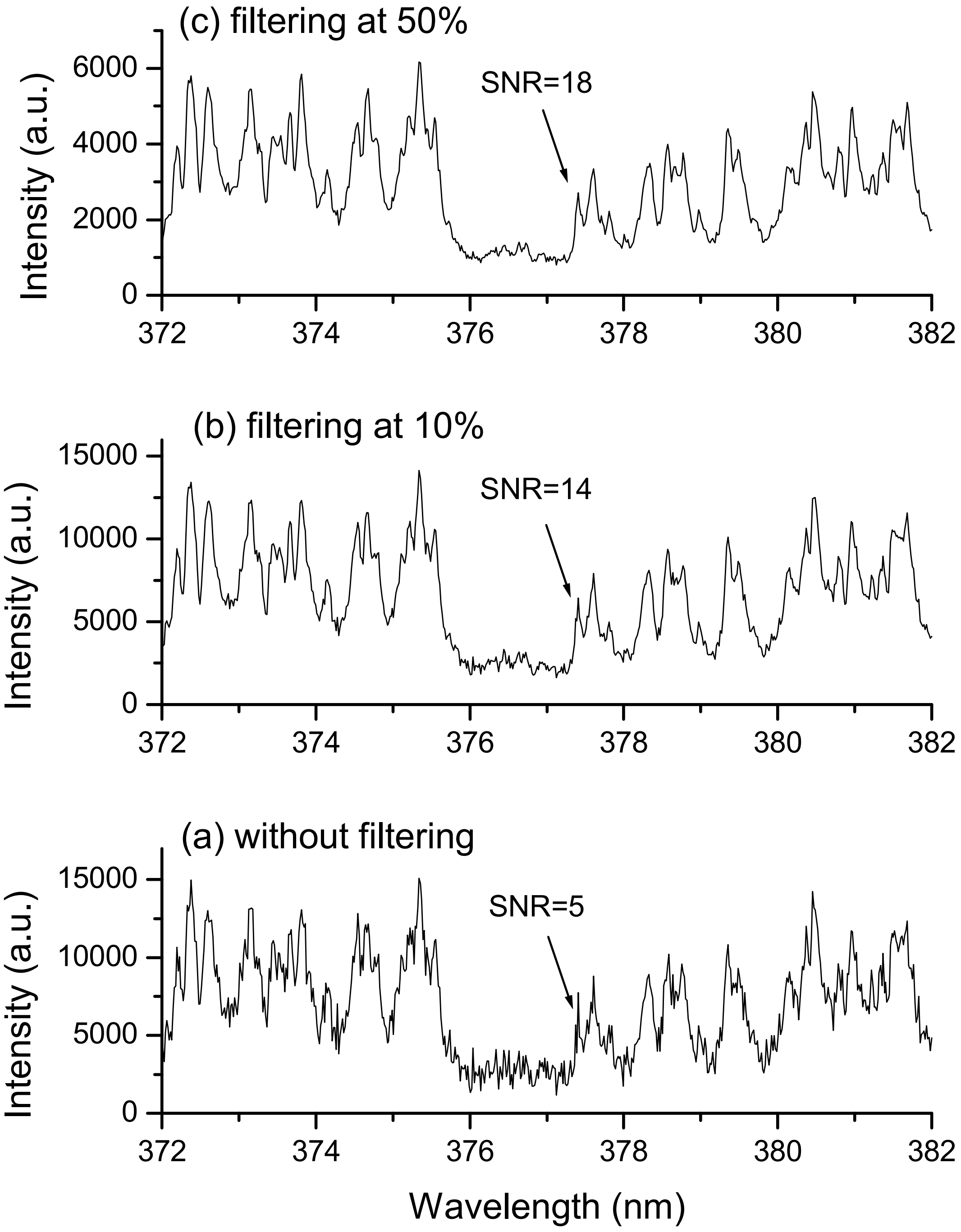

Figure 5: Section of LIBS spectrum from corroded iron, taken with the sample in movement: (a) summing all the spectra; (b) after filtering at the 10% level; (c) after filtering at the 50% level.

5.3.3 Stones

On the marble fragment, the optimal laser excitation was found for pulse energies of 82 mJ and 180 mJ, which corresponds to the first QS trigger delay of t_1=145 μs and an interpulse delay Δt = 55 μs at the maximum laser pumping level. The optimized acquisition gate was 600 ns and the delay from the second pulse was 200 ns. The data files were registered for 50 successive laser shots.

Despite the very high ablation rate observed from the strong surface scavenging by the laser, the corresponding plasma emission intensity was weak. Strong shot-to-shot oscillations were detected, both for the sampling at a fixed point and by moving the sample. Occasionally, for few successive laser shots, a signal intensity of about one order of magnitude higher than the average value occurs, probably due to the hitting of some inclusions which are more easily ablated. For this reason, in most cases, low filtering values gave the best results, as shown in Fig. 5.5. In this case, the filtering at 10% of the maximum allowed for good resolution of the two Al emission lines, which were at the limit of detection in the case of indiscriminate spectra summing. This kind of data processing also permitted to identify some other minor marble constituents, such as Si and Fe, in spectral regions not shown here (see chapter 4).

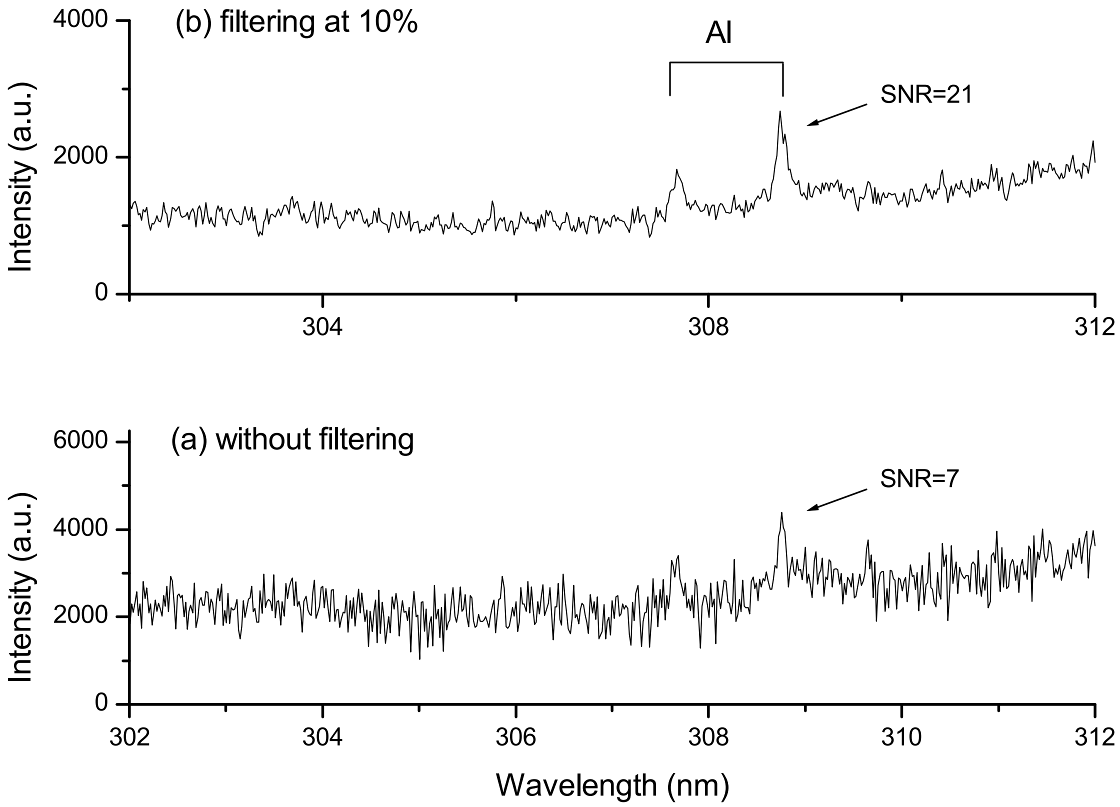

Figure 5.5: Example of a spectrum from marble obtained: (a) after summing the spectra over 50 laser shots; (b) after applying the filtering at 10% of the spectra maximum.

5.4 Element detection in water solutions

The Mg ionic emission line at 279.5 nm was chosen for the analysis, as it was the most intense feature in the spectrum analyzed. Six replicated measurements were performed by applying two laser pulse energy settings. The first laser setting corresponded to the maximum laser pumping and the QS trigger delays for which the most intense plasma emission was obtained, namely t_1=155 μs and interpulse Δt=75 μs. In this case, the laser pulse energies were E_1=91 and E_2= 214 mJ. For comparative measurements, laser pumping was decreased (second laser set) so that the pulse energies were E_1=37 and E_2= 156 mJ. Both the acquisition delay from the second laser pulse and gate width were set to 600 ns. Each measurement was performed by acquiring 1000 spectra recorded in separate columns inside the same data file.

For the considered laser energy sets, large shot-to-shot signal oscillations have been observed and regard both the line peak intensities and the continuum level. Such behaviour and its consequences on the quantitative LIBS analyses, is discussed in details in chapter 7.

The intensity of the analytical line from the indiscriminately summed spectra of a 5 mg/l solution resulted close to the detection threshold, particularly at the lower laser pulse energies used. In order to improve the SNR, the spectral filtering at different levels was tested, basing on the peak emission at 279.5 nm rather than on the spectral maximum. The choice was determined by a relatively high continuum level, which intensity strongly changes from one laser shot to another (see section 7.5).

For repeated measurements, the SNR was determined at different filtering levels for both sets of laser pulse energies, and the results are reported in Fig. 5.6. At lower pulse energies the optimal filtering level could be considered between 50% and 70%, while at the higher energies this interval is 40%-60%. An example of the spectra before and after applying the filtering procedure is given in Fig. 5.7, where the SNR for the analytical line is also reported. The applied filtering procedure leads to an improvement of the detection limit up to a factor 7 (see Chapter 7).

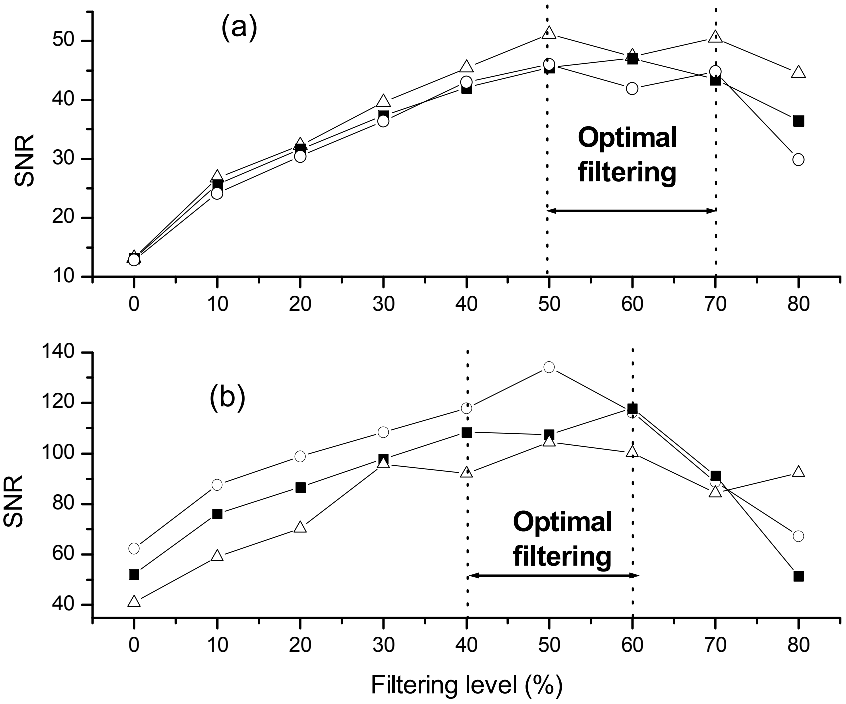

Figure 5.6: Signal-to-Noise ratio as a function of filtering level, for the solution with 5 ppm (three replicated measurements are shown) of Mg and laser pulse energies: (a) E_1=37 and E_2= 156 mJ, (b) E_1=91 and E_2= 214 mJ.

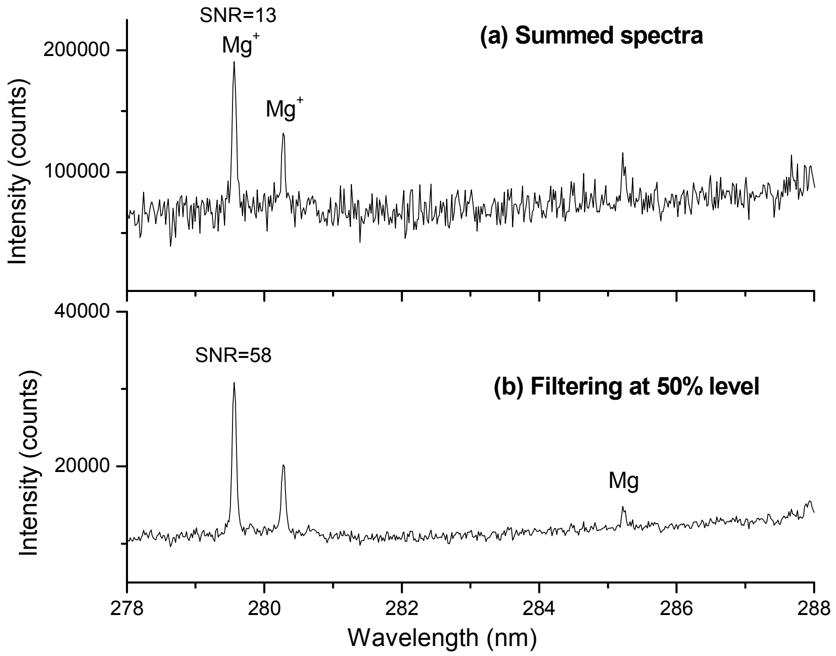

Figure 5.7: Comparison of the spectra obtained after: (a) summing over 1000 shots and (b) filtering at 50% of maximum peak; Mg concentration is 5 mg/l, laser pulse energies are E_1=37 and E_2= 156 mJ.

5.5 Conclusions

A separate shot-to-shot registration of LIBS spectra underwater, followed by an appropriate data processing, was shown to be effective in improving significantly the Signal-to-Noise Ratio. The efficiency of data processing depends on the laser pulses energies and on the sample properties. For solid samples underwater, it depends also on the ablation rate, surface roughness, homogeneity and sampling method (fixed or moving target). By eliminating low intensity spectra, the SNR improvement observed on immersed solids was up to factor of 4, allowing the detection of some minor elements in materials characterized by rough surfaces and inhomogeneities.

Laser plasmas produced in bulk water exhibit strong shot-to-shot intensity oscillations, and sometimes the breakdown events are even missing in the detection region. Improvement of the signal to noise ratio by averaging over a large number of laser pulses has been already achieved by applying 1000 laser shots. It was shown that the elimination of low intensity spectra can lower significantly the limit of detection. By summing only the spectra whose peak intensities are above 50% of the maximum peak in series of 1000 shots, an improvement up to a factor of seven was obtained.

The proposed spectral filtering could improve the LIBS detection threshold also in other surroundings (gases or other liquids), whenever strong shot-to-shot spectral intensity variations with a significant percentage of low intensity spectra occur. Examples can be found in the case of dense aerosols formed during ablation of some solid materials and with the short timing between successive laser pulses, and in multipoint measurements on rough surfaces. In the case of inhomogeneous samples, as for example in the mapping or search of hazardous materials, the presence of some trace elements could be looked for by peak filtering at the characteristic emission wavelength. The separate recording of spectra produced by each laser shot could also serve for an automatic detection of crater effects and for discarding measurements where a progressive signal reduction is observed. Conversely, the method could be applied for automatic determination of pre-ablation shots [5] and for summing only the spectra whose intensity has reached stable values.

Finally, improving the detection limit will be relevant in the case of system miniaturization for in-situ applications with small-size, low power laser sources.

5.6 References

[1] A. E. Pichahchy, D. A. Cremers, M. J. Ferris, Elemental analysis of metals under water using laser-induced breakdown spectroscopy, Spectrochim. Acta B 52 (1997) 25-39.

[2] R. Wisbrun, I. Schechter, R. Niessner, H. Schröder, K. L. Kompa, Detector for Trace Elemental Analyses of Solid Environmental Samples by laser Plasma Spectroscopy, Anal. Chem. 66 (1994) 2964-2975.

[3] U. Panne, C. Haisch, M. Clara, R. Niessner, Analysis of glass and glass melts during the vitrification process of fly and bottom ashes by laser-induced plasma spectroscopy. Part I: Normalization and plasma diagnostics, Spectrochim. Acta Part B 53 (1998) 1957–1968.

[4] L. Xu, V. Bulatov, V. V. Gridib, I. Schechter, Absolute Analyses of Particulate Materials by Laser-Induced Breakdown Spectroscopy, Anal. Chem. 69 (1997) 2103-2108.

[5] B. C. Castle, K. Talabardon, B. W. Smith, J. D. Winefordner, Variables Influencing the Laser-Induced Breakdown Spectroscopy Measurements, Appl. Spectroc. 52 (1998) 649-657.

[6] G.A. Lithgow, S.G.Buckley, Effects of focal volume and spatial inhomogeneity on uncertainty in single-aerosol laser-induced breakdown spectroscopy measurements, Appl. Phys. Lett. 87 (2005) (011501–1–011501–3).

[7] J.E. Carranza, D.W. Hahn, Sampling statistics and considerations for single-shot analysis using laser-induced breakdown spectroscopy, Spectrochim. Acta Part B 57 (2002) 779–790.

[8] V. Lazic, R. Fantoni, F. Colao, A. Santagata, A. Morone, V. Spizzichino, “Quantitative laser induced breakdown spectroscopy analysis of ancient marbles and corrections for the variability of plasma parameters and of ablation rate, J. Anal. At. Spectrom., 19 (2004) 429-436.

Chapter 6

LIBS ANALYSES OF IMMERSED SEDIMENTS

Abstract

LIBS technique was applied on sediments directly under water with aim to develop a method for in-situ characterization of submerged soft materials. For signal detection, both ICCD and non-gated, compact detectors were used. The major difficulties in underwater sediment analyses are related to the natural and laser induced surface roughness, and to the sample softness. The latter characteristic is responsible for the formation of particle clouds above the surface, which scatter both the laser and plasma radiation, and induce the breakdown formation above the analyzed surface. In such cases, a broad sonoluminescence emission from water, formed during the gas bubble collapse was sometimes registered. A way for obtaining quantitative analyses from strongly fluctuating LIBS spectra is discussed. Application of such a procedure could improve the measurement accuracy also in other surroundings and on samples different from the ones analyzed here.

6.1 Introduction

Among different LIBS applications developed [1-2], there are characterization of sediments and soils [3-6], which is important both for geological studies and environmental protection. The use of LIBS for soil analyses was recently proposed also for planetary exploration [7-9]. Soils or sediments were always analyzed by LIBS in atmospheric or low-pressure environment.

By using a DP laser excitation and gated ICCD detector, quantitative LIBS measurements were also obtained on flat metallic samples and rocks underwater [10-12] and LOD’s of about 100 ppm were achieved. The use of underwater LIBS coupled with non-gated detectors, whose typical integration time is in the order of milliseconds, has not been yet reported. In such case the detected emission might be affected by the sonoluminescence occurring much later than the LIBS signal [13-14]. The sonoluminescence can appear at the end of the gas bubble collapse, which for nanosecond laser-excitation is typically delayed in order of hundred of microseconds from the laser pulse [13-14]. The sonoluminescence spectrum has a broad spectral emission [16-17] attributed to ions-electrons recombination occurring at the high temperature of the compressed bubble.

In this work, feasibility of performing LIBS analyses on sediments directly under water was examined. The aim of the research was to develop and test a method for measuring the sediment elemental composition, including minor elements, which could be implemented in situ, e.g. for sub-glacial lake and marine exploration. In contrast with previously reported LIBS analyses of submerged samples [10-12, 16, 18-19], dealing with compact materials such as metals and rocks, sediments are soft materials, which underwater naturally generate suspended particles above the sample surface. These particles increase in number after laser-induced breakdown due to the intrinsic shock-waves, which blast away the material from the top layers. As a consequence, one expects severe fluctuations in the breakdown position due to impurities acting as centres for micro-plasma formation [20], as well as the radiation scatterers, with consequent changes of the plasma characteristics (emission intensity, temperature, density). Furthermore, a sediment surface has its natural and/or laser induced roughness, which also contributes to the signal instabilities. Removal of the suspended material by flushing water above the sample surface is not a viable solution, as the flux would provoke additional water turbidity by moving around the particles from the soft sediment. For similar reasons, it would not be possible to apply a gas flux above the examined surface [19], with the aim to create sample/air interface, which is more favourable for LIBS analyses.

LIBS measurements were performed using DP excitation from a single laser source. Both natural sediments and certified soils/sediments were analyzed under water. The latter were used to estimate roughly the detection limits and to generate the calibration graphs required for future quantitative analysis. The experimental lay-out and operating parameters were optimized and a data acquisition/processing procedure was established for obtaining quantitative LIBS results in the case of strongly fluctuating plasma characteristics, as in the present measurements. In order to evaluate the feasibility of using compact (not gated) spectrometers as a spectroscopic probe, comparative measurements were performed by using a HR system with an ICCD detector and a LR compact spectrometer, the latter without gating option (see section 2.2).

6.2 Experimental

6.2.1 Laboratory set-up

The plasma emission was produced by the Q-Switched Nd:YAG, already described in section 4.2 and operated in DP mode. The triggering scheme and examples of pulse energy partitions are reported in Chapter 4.

The laser beam was focused by two plano-convex lenses, whose equivalent focal length in air was 35 mm. The second lens was in contact with the water. The laser incidence was fixed at an angle, to avoid that the gas bubbles, formed by the breakdown, deposit on the immersed focusing lens and further disturb the laser transmission (Fig. 6.1). The signal was collected by a wide angle optical system, at 60° with respect to the laser beam, and brought to the LR spectrometer by a fibre (diameter 0.1 mm). Coaxial geometry has been also tested, but soon discarded because of frequent breakdown formation above the sample and towards the focusing lens, which increases the level of the detected plasma continuum. The compact detection system (Ocean&Optics S2000, range 200-500 nm) available in laboratory, has low resolution (about 0.3 nm) and slow gate aperture (3 μs). The detector integration time is in the millisecond scale.

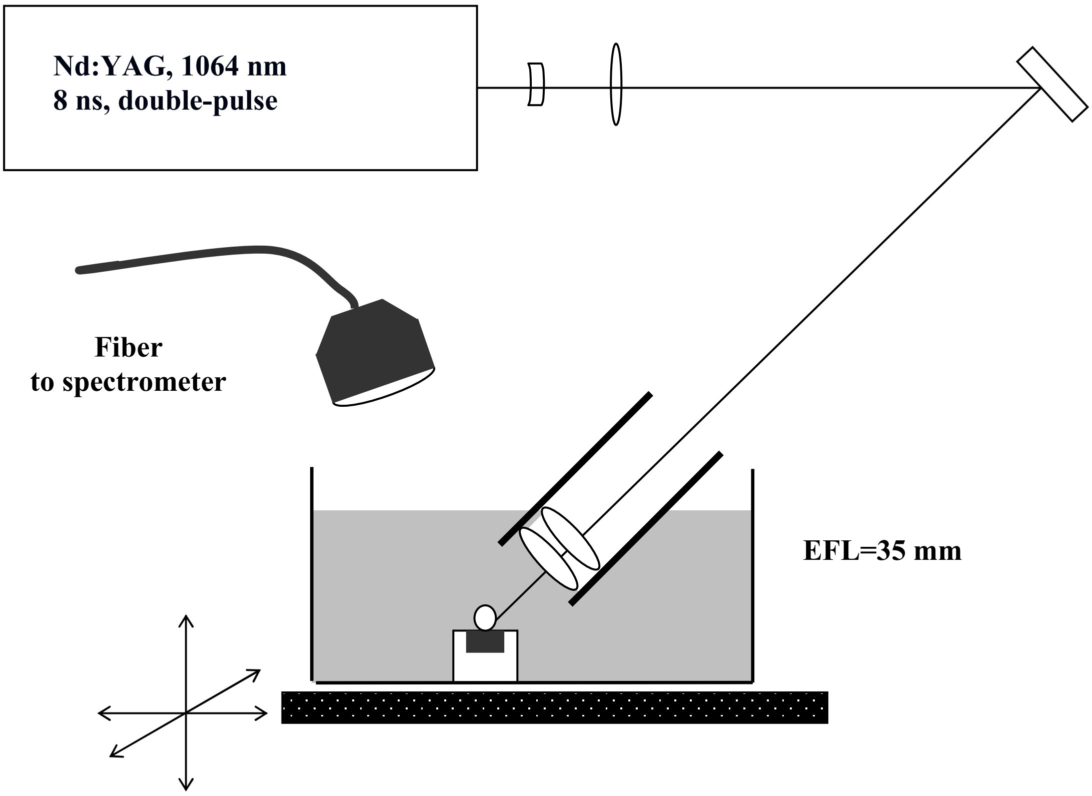

Figure 6.1: Experimental lay-out: EFL is the equivalent focal length in air

Since the use of an array of HR compact spectrometers (not available in laboratory) was planned for the submersible probe realization, comparative measurements were performed with a monochromator (Jobin Yvon 550) equipped with an ICCD, where grating 1200 gr/mm was selected. The latter system was considered as a HR system. The ICCD gain was set to zero and for comparative measurements the integration time was set to 3 ms, i.e. analogue to the non gated system. Both HR and LR systems were electrically triggered simultaneously with the first QS trigger, thus integrating also the plasma emission formed by the first laser pulse.

The beaker containing tap water, which was frequently renewed, was mounted on a holder adjustable in X, Y and Z directions to allow for the sample surface repositioning. No particular care was taken in controlling the water transparency and sample surface morphology during the measurements, as the experiment is intended to be applied in-situ, where different water and surface conditions are found. As said earlier, immersed sediments have their natural roughness, which increases during the LIBS measurements due to shock wave removal of the soft material.

Consequently, a departure form the optimal focusing distance is expected both for the sampling at a fixed position and for scanning the surface.

Each spectrum (acquired at each laser shot) was saved separately inside a single file relative to one measurement (on one sample at fixed conditions). This approach allows monitoring of shot to shot variations of the spectral intensities, and is also useful for rejecting the spectra affected by the breakdown above the sample surface, by crater effect or by a significant reduction of water transparency (see section 5).

6.2.2 Samples

The LIBS measurements were first performed on the Antarctic sediments taken during XVI Italian campaign [4], which were analyzed without any treatment. The exact composition of the examined natural sediments was unknown, and only the comparative values from the reference Antarctic sediment were available, which however was extracted at a different location and depth [4-5].

In order to check the possibility of quantitative measurements through the initial calibration and to roughly estimate the LOD's achievable, underwater measurements on certified standard sediment/soil samples were also performed. These samples have different properties from the natural ones; in particular, they are in form of fine powders. Before performing LIBS measurements, these materials were first pressed into pellets, inserted into the sample holder and kept underwater for at least one hour to allow for deep wetting. About 10 laser shots were applied prior to the analysis, in order to reduce the surface compactness of pellets and simulate in-situ conditions.

6.3 Optimization of the laser excitation

Immersed sediments are difficult to analyze directly underwater, mainly due to the formation of the suspended particles. Shortly after their immersion, a layer of turbid water is already present above the sediment surface. Laser ablation and material removal by the laser induced shock waves, further degrades the water transparency. This problem is particularly severe on certified samples in form of fine powders, where the amount of suspended material produced is remarkably higher than for natural sediments with larger grain sizes.

Running the laser at 10 Hz repetition rate, a severe LIBS signal reduction was observed already after first laser pulse (Fig. 6.2), caused by accumulation of the suspended particles in proximity of the sample surface. These particles scatter the incoming laser light, often causing a significant enlargement of the focal spot on the sample, sometimes also visible by bare eye. The presence of the particle cloud lowers the breakdown threshold of water itself, and this effect had been also exploited for determination of the particle concentration in liquids [20]. Plasma formation may then occur above the sample surface. In such cases a much weaker LIBS signal from the sediment, due to the laser absorption by the overlaying plasma, or even only plasma continuum emission are detected (Fig. 6.3). In order to avoid particle accumulation above the analyzed sediment, in all the successive measurements the laser was triggered manually at low frequency (lower than 0.5 Hz), allowing for the material blown by the laser to be partially deposited.

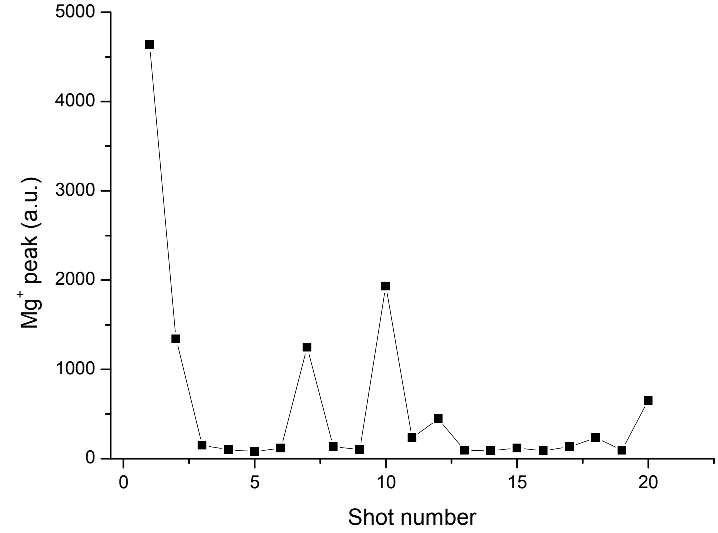

Figure 6.2: Shot-to-shot behavior of Mg$^+$ peak emission (at 279 nm) measured on the certified Antarctic sediment at a laser repetition rate of 10 Hz.

Further, the energy partition between the two laser pulses and the respective time delay were optimized to achieve the best signal characteristics. This optimization is particularly important for limiting the total number of laser pulses required for the analyses i.e. for reducing undesirable effects related to the formation of a dense particle cloud caused by the shock waves. In the present experimental set-up, it was found the LIBS signal maximum, averaged over 20 spectra acquired, for the energy partition between the pulses corresponding to E_1=60 mJ and E_2=240 mJ and for an inter-pulse timing Δt=75 μs. When the energy of the first pulse is reduced by shortening the time delay between the flash-lamp trigger and the first QS trigger, here set at t_1=145 μs, the line intensities decrease, probably due to less efficient gas bubble formation. On the other hand, increasing the first QS trigger delay, i.e. the first pulse energy, the energy of the second laser pulse is lowered and this can explain the observed signal reduction. For the chosen delay t_1=145 μs, the maximum second pulse energy correspond to an interpulse delay of 75 μs; this value was therefore chosen for the measurements.

6.4 Qualitative sediment analyses

The use of the spectrometer with ICCD allowed for time resolved LIBS plasma measurements. The plasma duration after the second laser pulse was examined first. Severe shot-to-shot variations of the emission line intensities, even at low laser repetition rates (see Fig. 6.3), make difficult to measure precisely the decay time behaviour of the emission lines. However, , as observed with a gate width set at 100 ns and by changing the gate delay with respect to the second laser pulse it was clear that the strongest line emissions occur for the acquisition beginning immediately after the second laser pulse. The plasma decays very rapidly and already after 500 ns the only observable emissions were from water and its impurities, namely the spectral lines from Mg ionic lines (around 280 nm) [18] and features from oxygen and hydrogen. The elimination of the initial plasma continuum after the arrival of the second pulse, while still keeping the LIBS signal high, would require a relatively fast gate aperture (less than 100 ns). Such a feature was not presently available in here used compact spectrometer, characterized by a relatively slow gate aperture (time required for full gate aperture is 3000 ns). It was therefore necessary to trigger the acquisition by the first laser pulse.

In order to simulate the use of a HR compact spectrometer system for underwater LIBS measurements on sediments, the ICCD acquisition gate on was set at 3 ms and the acquisition was triggered with the first laser pulse. The contribution of the plasma emission after the first laser pulse to the overall signal was first checked by reducing the gate width to 10 μs. For the selected laser pulse energies, only a rather weak continuum emission was detected, whose level can be neglected in comparison with the plasma emission measured after the second laser pulse. Such weak emission was attributed to a relatively low energy of the first laser pulse, and also to inherent electrical delays between the trigger and the effective gate aperture. Measured delay between the laser pulse emission and the ICCD gate aperture was about 80 ns. Due to severe plasma quenching after the first laser pulse (the cavitation bubble is not yet developed), the initially stronger plasma emission produced by the first pulse was not included in the signal integration.

Under the described experimental conditions and for long integration time (3 ms), on all the samples considered, both the main constituents and some minor species could be detected by applying a single laser shot sequence (Figs. 6.4-6.5). The latter elements include Ti, Ba, Mn and Li, the former Si, Ca, Al, C, Fe, Na and K. On immersed calcium carbonate rocks, which give a much higher LIBS signal and much less problems related to suspended particles, also Sr was detected. Tab. 6.1 collects the elements detected together with their most prominent emission lines.

LIBS spectral intensities were at least twice lower on the certified powder samples than on natural sediments. However, the measurements on the certified samples allowed estimating the detection limits in water, as reported in Tab. 6.2. The LOD values indicated here correspond to the lowest certified element concentrations which were detected in a single shot acquisition, so they are certainly higher than the real values.

Table 6.1: Elements in an Antarctic sediment and rock, detected by the HR and by the LR system. The element concentrations in the reference Antarctic sample are also reported.

			HR system		LR system
Element	Reference concentration	Line/band (nm)	Rock	Sediment	Sediment
Al	6,71%	308^{b}	+	+	Not resolved
		395^{b}	+	+	
Ba	566 ppm	455.4^{+}	+	+	-
		458.0	+	+	-
C	-	247.8	+	+	-
Ca	1.70%	390^{b+}	+	+	+
Fe	2.44%	275^{b+}	+	+	+
		375^{b}	+	+	+
K	2.7%	768^{b}	+	+	Out of range
Li	-	670.8	+	+	Out of range
Mg	1.52%	280^{b+}	+	+	+
		284.8			+
Mn	446 ppm	260.6^{b+}	+	+	+
Na	2.17%	589^{b}	+	+	Out of range
Si	33.5%	252^{b}	+	+	-
		288.1	+	+	+
Sr	217 ppm	460.7	+	-	-
Ti	2980 ppm	325,335^{b+}	+	+	+
		453.6	+	+	-

$^{(b)}$ *= emission band;* $^{(+)}$ *= ionic emission*

On some of the certified samples, resonant Cu transition at 324.8 nm was also detected, and for this element the lowest certified concentration detected was 114 ppm. Detection of Cu on the Antarctic sediment was not obtained, as its expected value is much lower (in the order of ppm) [4-5]. The evaluation of the LOD for Li was not possible since no certified value was given in all the reference samples investigated.

Table 6.2: Minimum certified concentrations of minor/trace elements detected on reference samples by the HR system in a single-shot DP acquisition. The effective LOD is lower than the values reported here.

Element	**Min. Conc. (ppm)**	**Sample**
Ba	59	ES6 – loess (France)
Cu	114	NIST2710 – contaminated soil (Montana)
Mn	375	NBS1646 – Estaurine sediment (Chesapeake Bay)
Ti	56	ES1 – marine deposit (Italy), mixed with PbO powder

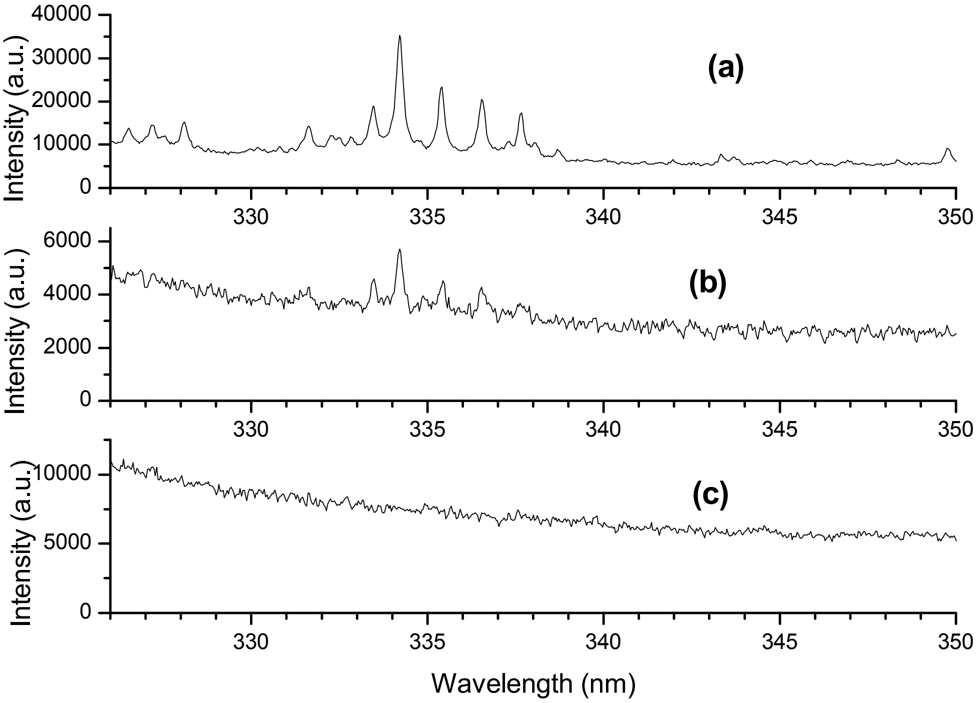

Figure 6. 3: HR, single DP shot LIBS spectra from the certified Antarctic sediment: a) optimal for the analysis; b) in presence of a weak breakdown above the surface; c) in presence of an intense breakdown above the sample surface. The emission lines belong to Ti^+.

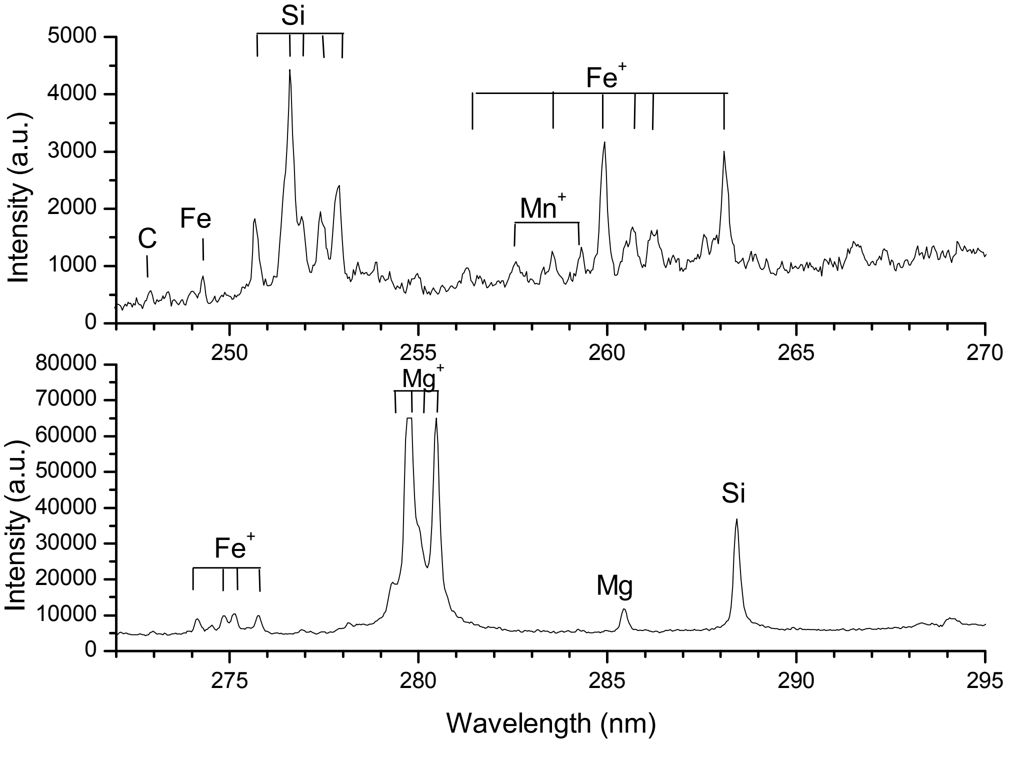

Figure 6.4: Examples of single shot spectra (HR system) taken on natural sediment in water: (a) detection of C, Si, Fe and Mn; (b) detection of Fe, Mg and Si

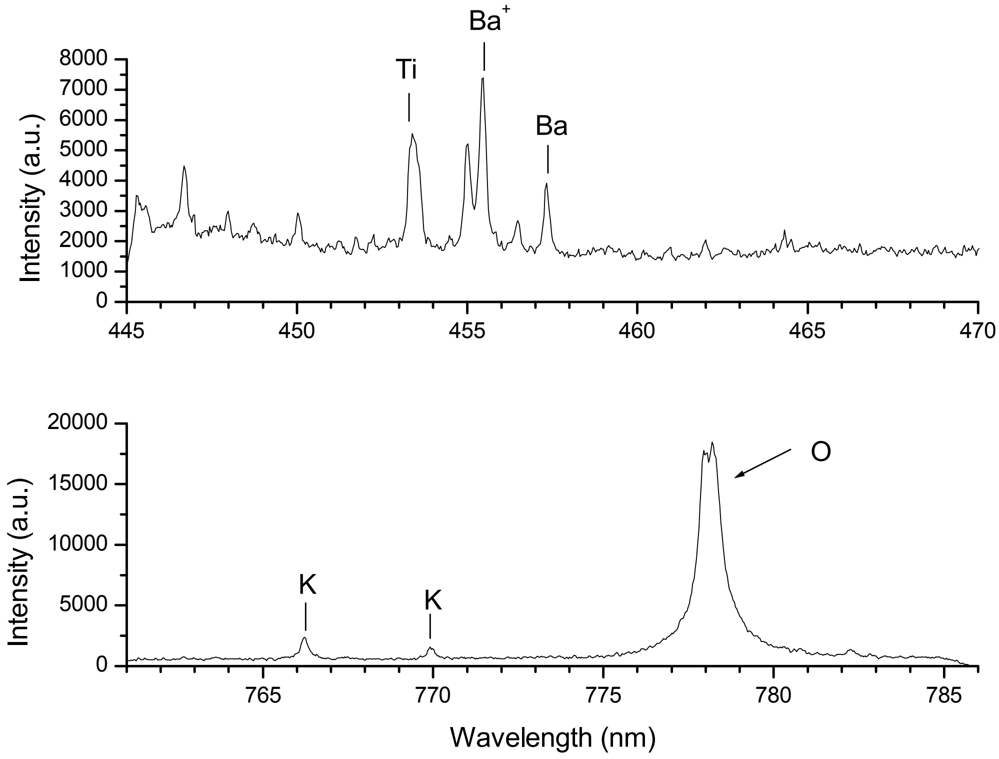

Figure 6.5: Examples of single shot spectra (HR system) taken on natural sediment in water: (a) detection of Ti and Ba; (b) detection of K and O

By applying a multi-shot data acquisition, the SNR and consequently the LOD might improve, particularly if an appropriate signal processing procedure is applied (section 5). For example, on the certified Antarctic sediment, after summing the emission produced by 20 laser shots, the SNR for the Si line at 289 nm was 14. On other hand, by summing only the spectra where the Si line peak intensity was above 10% of the maximum peak observed among these 20 spectra, the SNR of this line was improved by factor of 4. This improvement could be explained by the reduced plasma continuum level.

With the LR system, the number of detected lines is smaller than with the HR system (Tab. 4.1). This could be expected due to increased line overlapping and reduced SNR, and to the limited and fixed spectral range (200-500 nm). As shown in Fig. 6.6a, not well resolved Al lines overlap with ionic emission from Ti (around 308 nm) or Ca (around 395 nm). As a result, their direct measurements without applying a spectral deconvolution, is not possible with the LR system. Furthermore, strong water spectral emission features in the range 400-500 nm, do not allow resolving and detecting relatively weak Ba lines. Since the two detection systems have a comparable spectral response in the wavelength range 250-500 nm, the lower SNR values obtained by the compact spectrometer can be attributed to its poorer resolution.

If the breakdown was formed much above the sample surface, only a broadband spectrum was detected. This emission might be attributed both to the breakdown and to sonoluminescence emission [17] (Fig. 6.6b). Occasional appearance of the sonoluminescence emission was also observed by using the ICCD system with a gate delay of 100 μs from the second laser pulse, while keeping the gate width at 3 ms. The intensity of the sonoluminescence emission is generally higher for a symmetrical bubble collapse [21], and unlikely when close to a rigid surface where the collapse is asymmetric. In the present experiment, however, the target surface is soft and easily removed by the shock waves. In absence of well controlled material repositioning, a significant blasting of the top sediment layers might also increase locally the distance between the bubble, sometimes formed also before the focal point, and the sample surface. In this way, the probability of experiencing a symmetrical bubble collapse, and consequently observing sonoluminescence emission, could not be neglected.

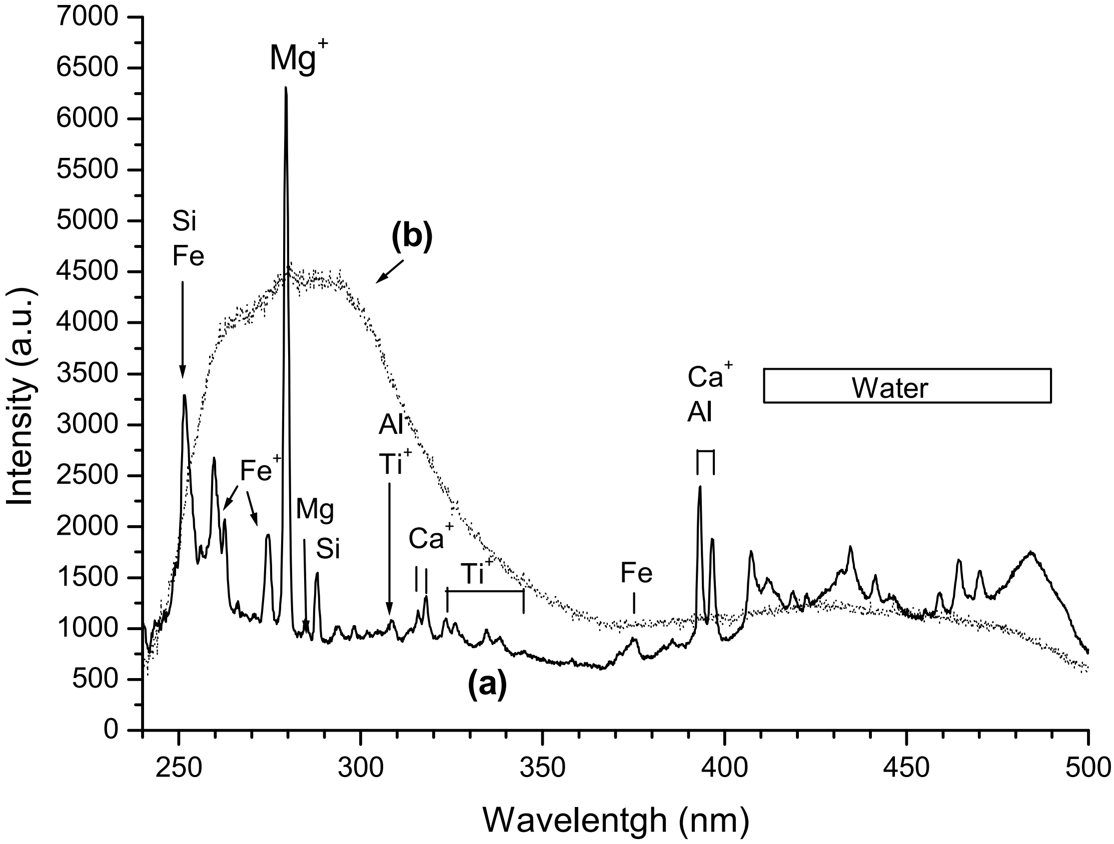

Figure 6.6: Example of LR spectrum: (a) obtained by summing 6 strong spectra taken on natural sediment in water; (b) single shot, broadband emission caused by breakdown formation above the sediment surface or by sonoluminescence (intensity multiplied by 6).

6.5 Calibration for quantitative analysis

Only the spectra acquired in a wide spectral range, i.e., by the LR system were considered for the calibration. Due to the line overlaps in the LR spectra, it was possible to analyze only a limited number of elemental lines, belonging to ionic emission from Mg, Ti and Fe, and to atomic emission from Si.

In order to discard the spectra containing a very weak line emission or only the continuum radiation, which may be particularly intense in presence of the sonoluminescence, the filtering procedure described in Chapter 5 was applied first. The filtering was performed with respect to the Mg^+ peak at 279 nm (after background subtraction) and its maximum value among the acquired spectra on a single sample (typically 100 spectra per sample) was used as a reference value. Automatically selected spectra, characterized by the Mg^+ peak intensity above 10% of the reference value, were successively saved as columns in another file. An attempt to obtain calibration graphs relative element concentration (see section 3.5) from the simply summed selected files failed, as the obtained data were fully uncorrelated. This was checked on the atomic emission from Si, after normalization on different ionic lines (from Ti, Mg or Fe). Consequently, this procedure for making any quantitative LIBS analysis on immersed soft materials must be considered unfeasible. Even attempting normalization only between different ionic emission lines, the correlation of the resulting calibration graphs was not satisfactory. The observed scattering of the data points may be attributed to strong, random variations in the plasma properties from one spectrum to another. This variation affects also the relative intensities of the analytical lines both due to different level population and to different atom to ion number ratios. For this reason, it was necessary to consider for the calibration only the spectra characterized by similar plasma parameters.

To this aim, one reference spectrum was selected among those acquired on different samples. Considering that the plasma parameters are related to the spectral distribution of the continuum emission [22-25], 7 spectral intervals for its comparison are defined (Tab. 6.3), each one a few nanometres wide. A program for further data processing was also written under LabView and performs the following operations:

1) For each spectrum relevant to a single sample the mean continuum intensities over defined comparing intervals (Tab. 6.3) are calculated;
2) These mean values are divided by the corresponding mean values for the reference spectrum;
3) The Relative Standard Deviation (RSD) between the points from step 2 is calculated;

4) If the RSD in step 3 is lower than a chosen value (example 0.2), here called “RSD limit”, this spectrum is selected for calibration;

5) All spectra selected in the previous step, relevant to one certified sample, are then summed for further analysis, i.e. used for the calibration.

When analyzing the RSD (step 3) for different spectra, it was found that its value could be as high as 1.2, indicating a strong difference in the spectral distribution of the plasma continuum with respect to the reference spectrum. In Fig. 6.7, examples of the normalized continuum intensity ratios and estimated plasma temperatures (discussed in following) are reported, together with the corresponding spectra.

Table 6.3: Spectral intervals used for comparison of the plasma continuum emission: λ_1 and λ_2 are the beginning and the end of the interval, respectively, with corresponding interval width $\Delta\lambda$.

Interval No.	**1**	**2**	**3**	**4**	**5**	**6**	**7**
λ_1 (nm)	240.0	267.5	290.5	361.0	387.0	399.0	450.0
λ_2 (nm)	243.0	269.5	291.5	365.0	389.0	402.0	452.0
$\Delta\lambda$ (nm)	3	2	1	4	2	3	2

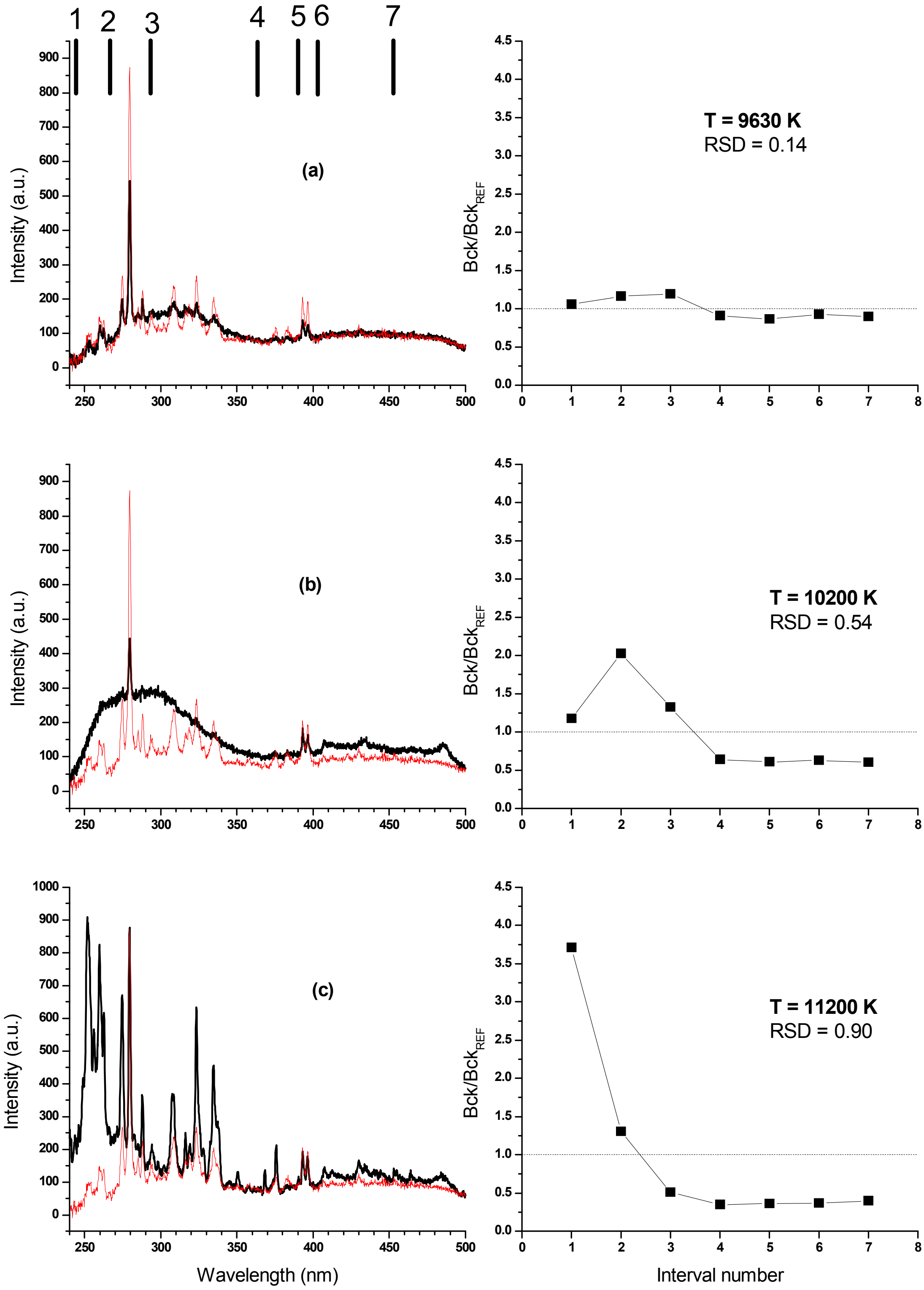

Figure 6.7: Left: single shot spectra compared to the chosen reference spectrum (RED); the intervals for comparing the continuum intensities are indicated (upper lines); Right: corresponding normalized ratios of the continuum intensities with respect to the reference spectra (estimated plasma temperature 9590 K), as a function of the interval number.

Due to the insufficient number of resolved emission lines from one element in the spectra registered by the LR system, it was not possible to calculate the plasma temperature from a Boltzmann plot. In the case of the spectra acquired by the HR system, due to small spectral interval in a single acquisition (about 20 nm wide), temperature measurements were possible only on Ti^+ lines. The measured values oscillate between 9500 K and 13500 K from one spectrum to another. However, in most of the cases, the energy span for the detected lines was too small for reliable temperature determination. For these reasons, the plasma temperature was successively determined using the Wien's displacement law for a black-body radiator and analyzing the wide spectra obtained by the LR spectrometer.

A temperature measurement of the single spark plasma in water by applying black-body approximation was already discussed in Chapter 3. However, in DP excitation the secondary plasma is formed inside the gas bubble. Several works have been published recently regarding the temperature measurements and modelling of plasma produced by a collapsing bubble underwater [23-24]. If the plasma is optically thick, i.e. the radiation emitted from the plasma originates only from the bubble surface, its emission could be approximated by the Planck's law for blackbody radiation [23]. Consequently, the plasma temperature could be calculated from the spectral distribution of the continuum radiation. For optically thin plasmas, as in the case of LIBS except at the wavelengths corresponding to very strong atomic/ionic transitions where a partial light re-absorption occurs, the continuum spectra represents a convolution of blackbody and bremsstrahlung spectrum if the conditions of LTE are fulfilled [23]. The latter conditions could be considered satisfied in most of LIBS plasmas, except for those characterized by a low electron density [25], as for example those generated in low pressure environments, which is not our case [14]. Assuming LTE, the emissivity of the plasma continuum is proportional to product of Planck's function, whether or not the photon field is in equilibrium with matter field, and the opacity [23-24].

In our case, the continuum spectral distribution, corrected for the instrument response, does not fit the Planck's function for the reasons described above, as the observed continuum peak is much narrower (Fig. 6.8). Not knowing the plasma opacity, necessary to correct expression for blackbody emission, the data were simply fitted in the range 240-370 mm, thus to find more precisely the peak position (Fig. 6.8). Note that the emission at longer wavelengths is less representative for the hot plasma core, as the absorption coefficient for inverse bremsstrahlung is proportional to λ^3 and there is also an emission contribution from cooler (external) plasma regions [26]. Subsequently, the plasma temperature was calculated from Wien's displacement low, using the peak wavelength obtained from the fit. For the spectra containing also line emission, and therefore useful for the sediment analyses, the calculated plasma temperature ranges between 9000 K and 11800 K. The estimated error in peak position determinations is smaller than ±10 nm; this uncertainty would correspond to an error in the temperature calculation lower than ±320 K. It thus appears that the calculated temperatures are comparable with those of a Boltzmann plot obtained by using Ti^+ lines, even though this fit was possible only on a limited number of very strong spectra and the temperature determination was affected by large errors, as discussed previously.

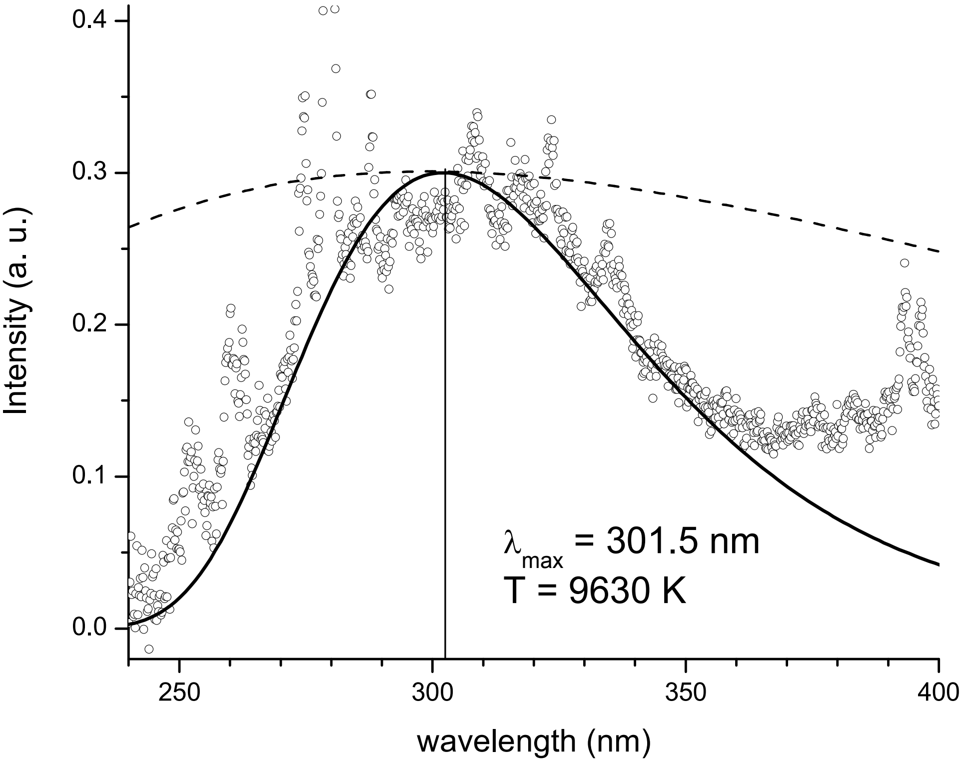

Figure 6.8: Example of the plasma continuum emission fitted mathematically (thick) to obtain the peak position and fitted blackbody radiation with the same peak position (dashed). The temperature was calculated from the Wien's displacement low.

Looking back to Fig. 6.7, case (a) refers to the spectrum considered acceptable for the calibration, where the calculated RSD (from step 3 above) is 0.14. The estimated plasma temperature is 9630 K, very close to a temperature of 9590 K calculated for the reference spectrum. For the spectrum shown in (b), the estimated plasma temperature is slightly higher (10 200 K) but the line emission is very weak, probably due to a partial breakdown above the sample. Consequently, the continuum spectral distribution is somewhat different from the reference spectrum and the calculated RSD is 0.54. In case (c), the peak of the plasma continuum emission is shifted towards shorter wavelengths and corresponds to the temperature of 11 200 K. Although some particularly strong emission lines are present in this spectrum, it was not chosen as the reference because in most cases, the acquired spectra showed much different continuum spectral distributions, i.e. corresponding to lower plasma temperatures. Generally, the spectra characterized by a continuum peak shifted towards longer wavelengths with respect to the chosen reference spectrum, present much weaker emission lines, and therefore are not useful for the sample analysis. The influence of a variable plasma temperature on the calibration for quantitative purposes was discussed in [27], where the derived correction factors could be calculated if the plasma temperature and electron densities were known. In here discussed measurements, it was possible to determine the plasma temperature from the LR spectra where the spectral resolution is too low for the calculation of the electron density., using for example the Saha equation applied to Mg and Mg^+ lines (multiplet not resolved). If we assume a constant electron density of $1 \cdot 10^{+17}$ cm^{-3} and the Saha equation, it is possible to estimate the behaviour of several ratios of selected species in the plasma, in the temperature range 9000 K to 11000 K (Tab. 6.4). The calculated ratio Mg^+/Fe^+ increases only by a factor of 1.15 and the calibration graphs for relative concentration measurements would not be strongly affected by the temperature variation. On the other hand, the ratio of Si/Ti^+ is reduced for factor 3.5 when the plasma temperature is increased from 9000 K to 11000 K. This factor is even higher if we consider the ratios Si/Mg^+ and Si/Fe^+. In the latter case, the energy levels of the Si line at 288.16 nm and the Fe multiplet around 275 nm are quite close (5 eV and 5.6 eV, respectively), and therefore their intensity ratio is not expected to change significantly due to a variation of the level population, but rather to the ionization degree. In spite of the fact that the calculations do not take into account changes of the level populations and possible variations of electron density with plasma temperature, they indicate the relevance of selecting suitable spectra (e.g., those with similar temperatures) prior to calibration.

Table 6.4: Partition between atoms and ions for different elements at two plasma temperatures, calculated for an electron density of 10^{17} cm^{-3}.

Element	T=9000 K		T=11000 K		Population ratio at 9000 K	Population ratio at 11000 K
	Atoms (%)	Ions (%)	Atoms (%)	Ions (%)		
Mg	25.0	75.0	6.4	93.6	Mg^+/Fe^+=1.01	Mg^+/Fe^+=1.15
Fe	65.2	34.8	7.4	92.6		
Si	62.8	37.2	17.9	82.1	Si/Ti^+=0.714	Si/Ti^+=0.184
Ti	87.3	12.7	2.7	97.3		

After imposing different values for the “RSD limit”, it was found that sufficiently well correlated calibration graphs, regarding relative element concentrations, could be obtained for an “RSD limit” up to 0.3. Lowering of this limit leads to improved correlation but results into a smaller number of selected spectra. This has the consequence that, when the spectra are summed, the SNR is reduced.

Examples of the calibration graphs obtained for the “RSD limit” of 0.3 are reported in Fig.6.9. It can be seen that, by applying the above described procedure, a relatively good correlation (above 0.92) between the relative element concentrations and the measured line intensity ratios could be obtained.

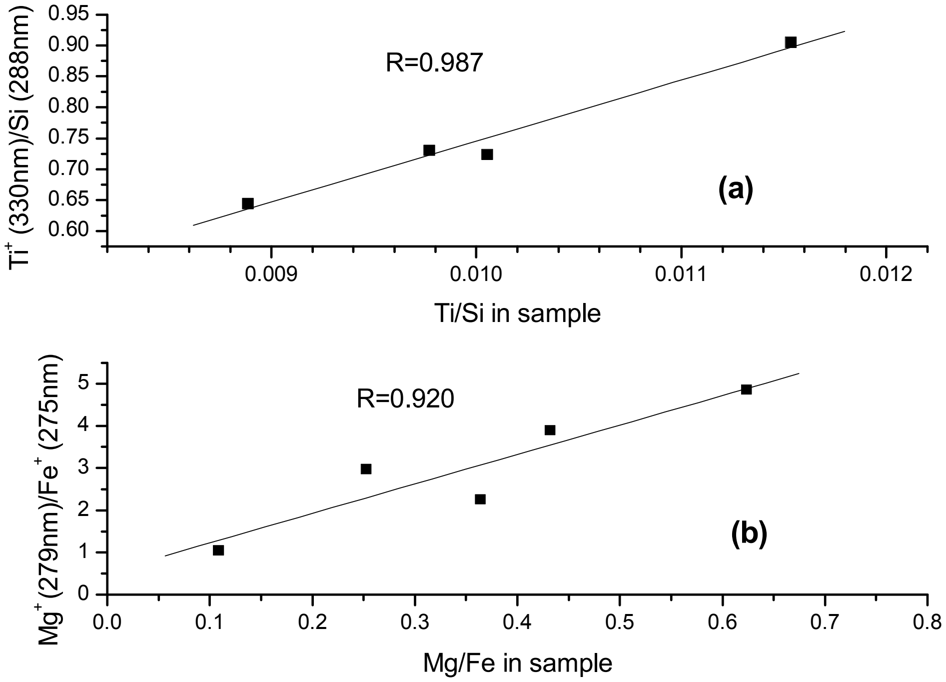

Figure 6.9: Calibration graphs obtained using the LR spectrometer and spectral selection with an “RSD limit” of 0.3. The ratios reported in the ordinate axis refer to the peak values after background subtraction.

6.6 Conclusions

In this work it is demonstrated that sediments can be analyzed by a double-pulse LIBS applied directly underwater, also if a non-gated detector is employed. Different experimental configurations were tested, and an angular laser incidence on the sample was chosen in order to reduce perturbations in laser transmission caused by the gas bubbles formed by previous laser pulses and deposited on the focusing lens. Very low laser repetition rates must be selected to avoid accumulation of a dense particle cloud above the analyzed surface, as the soft sediment material is easily removed by the shock waves formed in the interaction. Strong shot-to-shot variations of the spectral features and their intensities are encountered due to rough sample surfaces (natural or laser-induced roughness), and to light scattering caused by suspended sediment particles (always present), which are also responsible for a frequent breakdown formation above the surface. If the plasma was produced above the sample surface, a sonoluminescence signal was also occasionally detected. Such signal generates after the bubble collapse and is characterized by a relatively intense broadband emission. Intense, broad band continuum spectra not carrying analytically useful line emission should be avoided in the spectra summation prior to the data analysis, as it partially masks the emission from the analytical lines. If gated detection is not used, therefore allowing a possible measurement of an intense occasional sonoluminescence emission, the spectra containing an intense continuum component could be eliminated via software.

With the high resolution spectrometer, a number of minor sediment elements were detected: in this case, for example, the LOD's of Ti and Ba are lower than 60 ppm in a single shot acquisition. The number of the detected lines by the low resolution spectrometer is lower, although the spectral throughput for the two systems is similar.

Direct calibration for quantitative LIBS analyses of the submerged sediments is not feasible because the plasma parameters change significantly from one shot to another. This is reflected in variable line intensity ratios, and consequently, in uncorrelated or weakly correlated calibration data. However, selecting only the spectra with correspondingly similar plasma temperatures, here identified from the spectral distribution of the continuum emission, made possible to obtain well correlated calibration graphs. This opens a possibility for direct quantitative LIBS analyses of submerged sediments or other soft or rough surface materials underwater.

The proposed method could improve the measurement accuracy, whenever this is affected by variable plasma parameters, as for example during ablation of dusty or rough surfaces or in the presence of laser induced craters, which might strongly influence the LIBS plasma properties [28].

The results presented here demonstrate that LIBS is a promising technique for direct underwater sediment characterization, capable to supply in situ important environmental and geological data, as well as information about biological activity in the examined water (e.g. to quantify the presence of biogenic Si and Ba). Further developments imply the use of an array of high resolution compact spectrometers, covering a broad spectral range, in order to extend the number of elements that could be analyzed and/or to improve their detection limits.

6.7 References

[1] J. D. Winefordner, I. B. Gornushkin, T. Correll, E. Gibb, B. W. Smith, N. Omenetto, Comparing several atomic spectrometric methods to the super stars: special emphasis on laser induced breakdown spectrometry, LIBS, a future super star, J. Anal. At. Spectrom., 19 (2004) 1061-1083.

[2] L. J. Radziemski, From LASER to LIBS, the path of technology development, Spectrochim. Acta Part B, 57 (2002) 1109-1113.

[3] C. Lopez-Moreno, S. Palanco, J. J. Laserna, Remote laser-induced plasma spectrometry for elemental analyses of sample of environmental interest, J. Anal. At. Spectrom. 19 (2004) 1479-1484.

[4] R. Barbini, F. Colao, V. Lazic, R. Fantoni, A. Palucci, M. Angelone, On board LIBS analysis of marine sediments Collected during the XVI Italian campaign in Antartica, Spetrochim. Acta Part B, 57 (2002) 1203-1218.

[5] V. Lazic, R. Barbini, F. Colao, R. Fantoni, A. Palucci, Self-absorption model in quantitative Laser Induced Breakdown Spectroscopy measurements on soils and sediments, Spectrochim. Acta Part B, 56 (2001) 807-820.

[6] R. Barbini, F. Colao, R. Fantoni, A. Pallucci, F. Capitelli, Application of laser-induced breakdown spectroscopy to the analysis of metals in soils, Appl.Phys. A 69 (1999) 175–178

[7] A. K. Knight, N. L. Scherbarth, D. A. Cremers, M. J. Ferris, Characterization of laser-induced breakdown spectroscopy (LIBS) for application to space exploration, Appl. Spectrosc. 54 (2000) 331-340.

[8] F. Colao, R. Fantoni, V. Lazic, A. Paolini, F. Fabbri, G. G. Ori, L. Marinangeli, A. Baliva, Investigation of LIBS feasibility for in situ planetary exploration: An analysis on Martian rock analogues, Planetary and Space Sci. 52 (2004) 117-123.

[9] V. Lazic, I. Rauschenbach, S. Jovicevic, E. K. Jessberger, R. Fantonia, M. Di Fino,Laser induced breakdown spectroscopy of soils, rocks and ice at subzero temperatures in simulated martian conditions, Spectrochim. Acta Part B, 56 (2007) 1546-1556.

[10] V. Lazic, F. Colao, R. Fantoni, V. Spizzichino, Recognition of archeological materials underwater by laser induced breakdown spectroscopy, Spectrochim. Acta Part B 60 (2005) 1014-1024

[11] A. E. Pichahchy, D. A. Cremers, M. J. Ferris, Elemental analysis of metals under water using laser-induced breakdown spectroscopy, Spectrochim. Acta Part B, 52, (1997) 25-39.

[12] De Giacomo, M. Dell'Aglio, F. Colao, R. Fantoni, V. Lazic, Double-Pulse LIBS in water bulk and on submerged bronze samples, Appl. Surf. Sci., 247 (2005) 157–162.

[13] D. Lohse, Sonoluminescence: inside a microreactor, Nature 418 (2002) 381-383.

[14] M. P. Brenner, Single-bubble sonoluminescence, Rev. of Modern Physics 74 (2002) 425-484.

[15] A. Vogel, J. Noack, K. Nahen, D Theisen, S. Busch, U. Parlitz, D. X. Hammer, G. D. Noojin, B. A. Rockwell, R. Birngruber, Energy balance of optical breakdown in water at nanosecond to femtosecond time scales, Appl. Phys. B 68 (1999) 271-280.

[16] A. Casavola, A. De Giacomo, M. Dell'Aglio, F. Taccagna, G. Colonna, O. De Pascale, S. Longo, Experimental investigation and modeling of double pulse induced laser plasma spectroscopy under water, Spectrochim. Acta Part B 60 (2005) 975-985.

[17] R. Hiller, S. J. Putterman, B. P. Barber, Spectrum of synchronous picosecond sonoluminescence, Phys. Rev. Lett. 69 (1992) 1182-1184.

[18] De Giacomo, M. Dell'Aglio, F. Colao, R. Fantoni, V. Lazic, Double-Pulse LIBS in water bulk and on submerged bronze samples, Appl. Surf. Sci., 247 (2005) 157–162.

[19] D. C. S. Beddows, O. Samek, M. Liska, H. H. Telle, Single-pulse laser-induced breakdown spectroscopy of samples submerged in water using a single-fibre light delivery system, Spectrochim. Acta Part B, 57 (2002)1461-1471.

[20] Bundschuh, J-I Yun, R.Knopp, Determination of size, concentration and elemental composition of colloids with laser-induced breakdown detection/spectroscopy (LIBD/S), Fresenius J.Anal.Chem. 371 (2001) 1063-1069.

[21] C-D. Ohl, Probing luminescence from nonspherical bubble collapse, Phys. Of Fluids 14 (2002) 2700-2708.

[22] H. R. Griem, Plasma Spectroscopy, McGraw-Hill, USA (1964).

[23] W. C. Moss, D. B. Clark, D. A. Young, Calculated pulse widths and spectra of a single sonoluminescing bubble, Science 276 (1997) 1398-1401

[24] S. Hilgenfeldt, S. Grossmann, D. Lohse, Sonoluminescence light emission, Phys. Of Fluids 11 (6) (1999) 1318-1330

[25] T. Fujimoto, R.W. P. Whirter, Validity criteria for local thermodynamic equilibrium in plasma spectroscopy, Phys. Rev. A 42 (1990) 6588-6601.

[26] P. A. Barnes, K. E. Reickhoff, Laser induced underwater sparks, Appl. Phys. Lett. 13 (8) (1968) 282-284.

[27] V. Lazic, R. Fantoni, F. Colao, A. Santagata, A. Morone, V. Spizzichino, Quantitative Laser Induced Breakdown Spectroscopy analysis of ancient marbles and corrections for the variability of plasma parameters and of ablation rate, J. Anal. Atom. Spectrom. 19 (2004) 429-436.

[28] S. S. Mao, X. Zeng, X. Mao, R. E. Russo, Laser-induced breakdown spectroscopy: flat surface vs. cavity structures, . J. Anal. At. Spectrom. 19 (2004) 495-498.

Chapter 7

LIBS ANALYSES OF LIQUID IMPURITIES

Abstract
The analytical performance of LIBS for bulk liquid was studied as a function of the solution composition and concentration. The signal depletion in the detection region, caused by changes of the breakdown location, was studied as a function of the analyte concentrations and water salinity. Influence of the moving breakdown on the plasma parameters and quantitative LIBS analyses is also considered. Calibrations were performed on water solutions containing Mg, Cr or Mn, at different sets of the laser pulse energies, and the detection limits were considerably lowered by applying data filtering procedure.

7.1 Introduction

One of the growing requests for LIBS technique regards in-situ analyses of water solutions, which is important for environmental control [1-4], for monitoring of cooling or waste waters from industry, thermo-electric and nuclear power plants [4-6], then for geological and marine researches [7], for study of chemical reactions in the liquid phase etc. A number of papers reported LIBS analysis of waters in presence of water-air interface, by applying single [2-12] or double pulse excitation [13]. However, in some cases direct measurements on bulk water are required, so in the absence of liquid-gas interface. Examples include detection of leakages in industrial plants, measurements of biological activity, determination of nutrients and pollution in deep waters, characterization of sub-glacial waters, etc. A very few studies regard LIBS analyses of bulk liquids [1, 9, 14-15], where the LOD's below 1 ppm were obtained for some elements [14-15] when applying DP excitation. Presently, the studies relative to matrix effect, i.e. the liquid composition, on the LIBS signal are not available in literature. On the other hand, influence of the size and concentration of colloid particles on breakdown probability in liquids are known [9, 16]. It was found that LIBS signal reaches the maximum at certain, low colloid particle concentrations and that further increase of the particle number causes the signal reduction, attributed to the radiation scattering and absorption by the particles [9].

Here, an influence of matrix effect in LIBS analyses of bulk liquids has been studied on water solutions containing different concentrations of Mg, Mn or Cr. In view of developing of the LIBS method for quantitative bulk water analyses in-situ, that could regard both sweat waters (river, lakes, wells) and seawaters, as well as mixed waters (close to river foci), the solutions from above, prepared starting from pure water and the same with different grades of salinity were examined.

7.2 Experimental

The experimental set-up is already described in sections 4.2 and 5.2.

Calibration graphs for quantitative LIBS analyses were generated on reference solutions, adding properly $MgSO_4$, $MnCl_2•7H_2O$ or $Cr(CH_3COH)_3$ to a pure (milli-Q) water. The corresponding minimum element concentrations were 5 ppm for Mn and Cr, and 1 ppm for Mg. The latter elements was chosen as a common component of waters, Mn as an element related to bioactivity in waters and Cr as an example of contaminant.

In order to study the influence of water salinity on the LIBS signal, beside the solutions prepared from pure water, the analytes with the same concentrations were also analyzed in:

a) pure water with NaCl properly added to simulate seawater salinity (ASW);

b) mixing pure water (PW) and ASW in ratios 70%-30% (ASW30).

In order to avoid disturbances from eventual nanoparticle formation, which for example were clearly observed (clustered) after long measurement sessions in solutions containing Mg in concentrations of 200 mg/l or more, the higher concentration solutions in the beaker (over 50 mg/l of an analyzed element) were exchanged each 30 minutes of the measurements. During water exchange, the focusing lens was always cleaned to avoid accumulation of the gas bubbles produced by the breakdown.

For each solution concentration, six replicated measurements were performed by applying two laser pulse energy settings. The first laser setting corresponded to the maximum laser pumping and the QS trigger delays for which the most intense plasma emission was obtained, namely t_l=155 μs and interpulse Δt=75 μs. In this case, the laser pulse energies were E_1=91 and E_2= 214 mJ. For comparative measurements, laser pumping was decreased (second laser set) so that the pulse energies were E_1=37 and $E_{2=}$ 156 mJ.

After performing further optimization of the laser excitation, as described in Chapter 8, some measurements were repeated by applying E_1=72 mJ, E_2=144 mJ, delayed for 75 μs. In these conditions the first laser pulse is split into a sequence of 5 pulses.

Both the acquisition delay from the second laser pulse and gate width were set to 600 ns. These values were chosen after optimization of the LIBS signal on the lowest concentration solutions for Mg and Mn. Each measurement was performed by acquiring 1000 spectra recorded in separate columns inside the same data file.

7.3 LIBS signal oscillations

For both laser energy sets, strong shot-to-shot signal oscillations have been observed, although the liquid sample can be considered homogeneous. However, in the case of bulk water some other effects must be considered, such as the statistical probability for the breakdown [9, 17-19] and the moving breakdown phenomenon [19]. The latter effect has been observed also with the naked eye, particularly at the higher pulse energy set and for concentrated solutions. This was confirmed by investigating the breakdown probability inside the detection region, as a function of the solution concentration.

The presence of the breakdown was determined through an average value of the continuum plasma emission in the spectral range 277.5-279 nm. For the background compensated ICCD, the average continuum level was about zero in the absence of plasma, and for the breakdown threshold the average continuum level was fixed to only two ICCD counts. The percentage of the breakdown events at a single solution concentration was calculated as an average value over six measurements, each one performed over 1000 laser shots, and the obtained values, together with their standard deviation, are reported in Fig. 7.1.

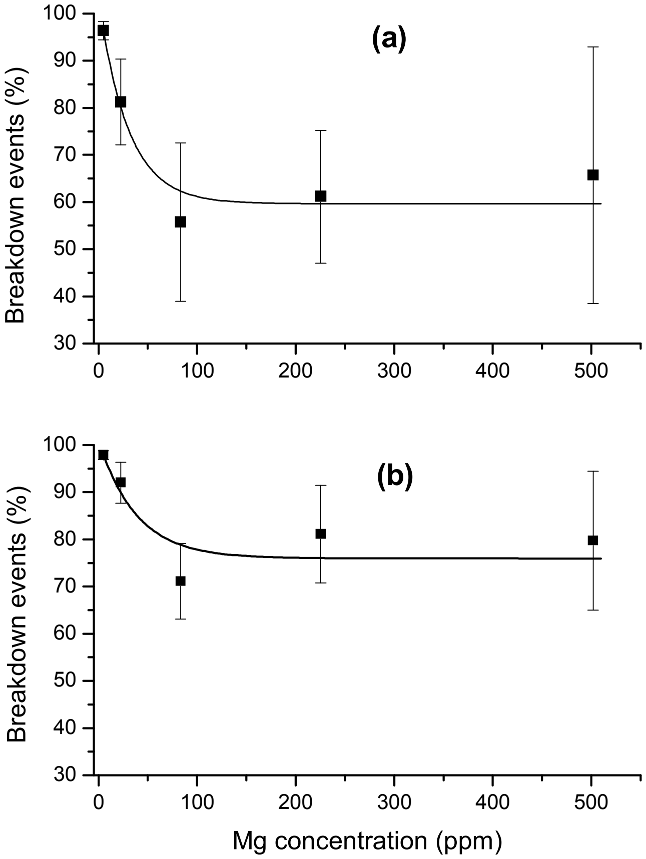

Figure 7.1: Number of breakdown events (%) in the detection region as a function of Mg concentration in pure water, for two sets of laser pulse energies: (a) E_1=37 and E_2= 156 mJ, (b) E_1=91 and E_2= 214 mJ.

The measured breakdown probability in the detection region, whose sectional diameter was about 3 mm, is close to 100% at the lowest solution concentration for both the laser energy sets considered. Increasing of the solution concentration initially leads to a decrease of the number of breakdown events and then remains almost constant. As it is well known, the breakdown probability in water increases with the presence of solutes [17-19], and the observed reduction of the breakdown events in the detection region (Fig. 7.1) is caused by the spatial movement of the plasma towards the focusing lens. The plasma position also became less stable with increasing the solution concentration, as observed from the progressive deterioration of the measured standard deviation.

7.4 Matrix effect

When comparing the solutions with different grades of water salinity, at fixed analyte concentration the most intense plasma emission was obtained on the solution prepared from pure water (Fig.7.2). The measurements were performed by changing the gate delay from the laser pulse and keeping the gate width constant at 200 ns. In all the cases examined the plasma emission, measured through the continuum intensity, extinguishes after about 1500 ns from the second laser pulse, but the decay rate is slower for higher water salinity. An overall decrease of the plasma intensity with water salinity is attributed to a visible plasma elongation. The plasma formation before the focusing point is responsible for partial laser absorption (remaining portion of the pulse) and to a reduced energy available for the bubble formation and expansion after the first pulse. Analogue plasma elongation was observed by adding any impurity to water (Fig. 7.3), including the analytes as discussed above. This effect causes fast saturation of the calibration curves (see next section).

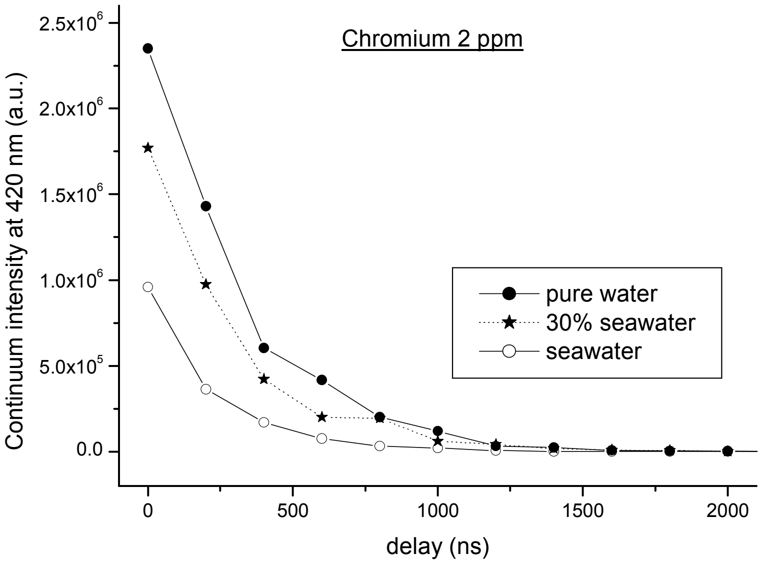

Figure 7.2: Reduction of the plasma continuum intensity with water salinity

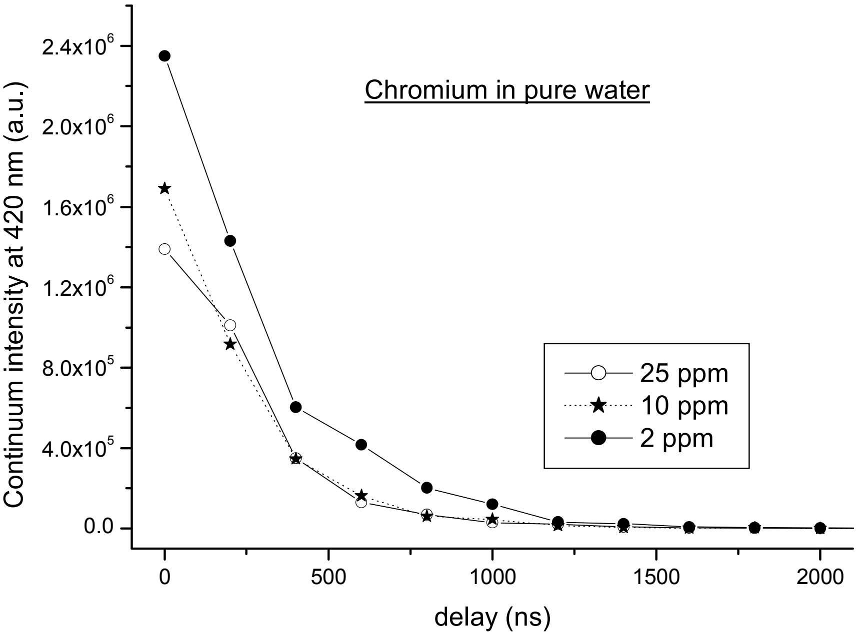

Figure 7.3: Reduction of the plasma continuum intensity with impurity concentration

If we compare the ionic line intensity between solutions with the same analyte concentration but with different grades of salinity, it behaves in analogue way as the continuum plasma emission, i.e. it decreases with the salt addition. However, the differences are reduced with increasing of the solution concentration, which itself gives rise to the plasma elongation (Fig. 7.4).

Presence of NaCl in water decreases the ionic line intensities but enhances the atomic emission (Fig. 7.5). This can be explained by lowering of the plasma temperature and/or by increasing of the electron density in the plasma. Sodium has low ionization potential (5.14 eV), thus contributes both to a decrease of the breakdown threshold with consequent plasma elongation, and to an increase of the electron density in plasma. The latter effect leads to a more efficient recombination, so to higher atomic-to-ionic ratios in the plasma (eqn. 2.7). As a result, the highest detection limits relative to the chosen analytical ionic lines, were obtained in the case of the water with the highest salinity (Tab. 7.1).

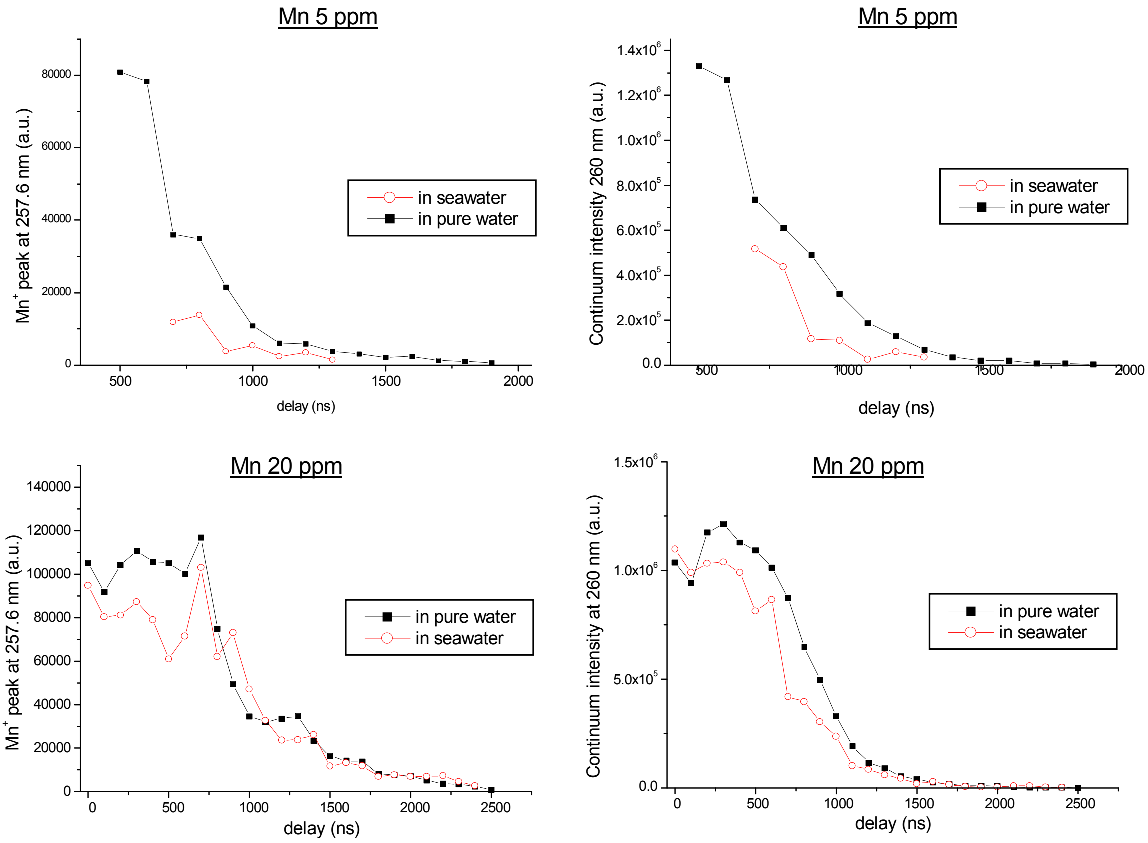

Figure 7.4: Temporal behavior of Mn$^+$ peak and continuum intensity in pure and seawater.

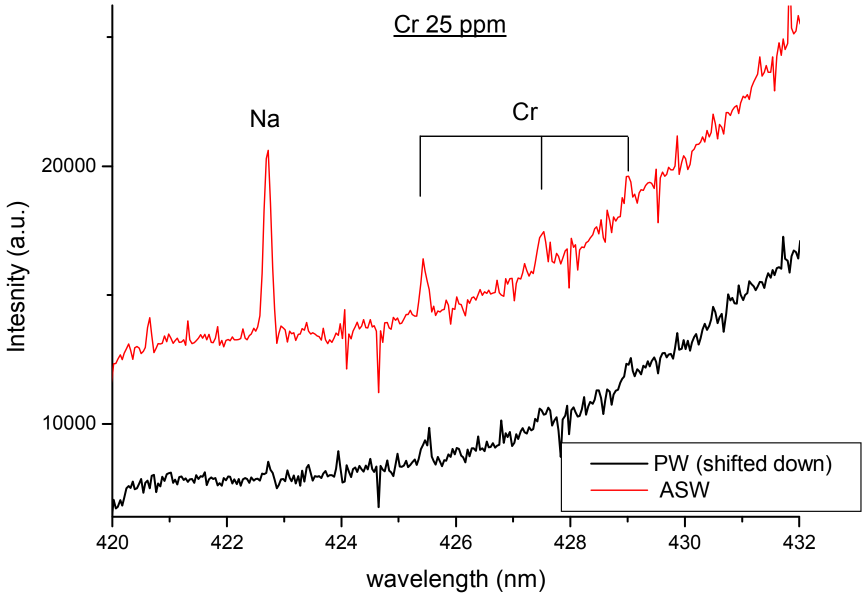

Figure 7.5: Atomic emission from Cr in pure water (spectrum shifted down) and artificial seawater; delay 600 ns, gate 2400 ns, accumulation over 100 shots

7.5 Calibration for quantitative analyses

In a view of a quantitative analysis, the application of an internal standardization procedure was considered (see section 2.5). Spectra were acquired in a narrow region (278-288 nm) encompassing the analytical line, but not containing spectral features due to water (oxygen and hydrogen), which might be used for normalization. Then, the possibility to normalize the signal on the nearby continuum was examined. The presence of a possible correlation between the background emission and the line peak intensity, as observed in case of the ablation of solid samples in air [20-21], was first investigated. In the present LIBS measurements on bulk solutions, this correlation was found to be rather poor, and also dependent on the laser energy and on the solution concentration (Fig. 7.6). Comparative calibration plots for Mg were created, where the spectra were summed over 1000 laser shots, before and after the analytical peak normalization on the background level (not shown). It was found that the correlation coefficient obtained with the normalization was lower than that in the absence of the normalization. As a consequence, such internal standardization procedure is not adequate for the LIBS measurements in bulk water.

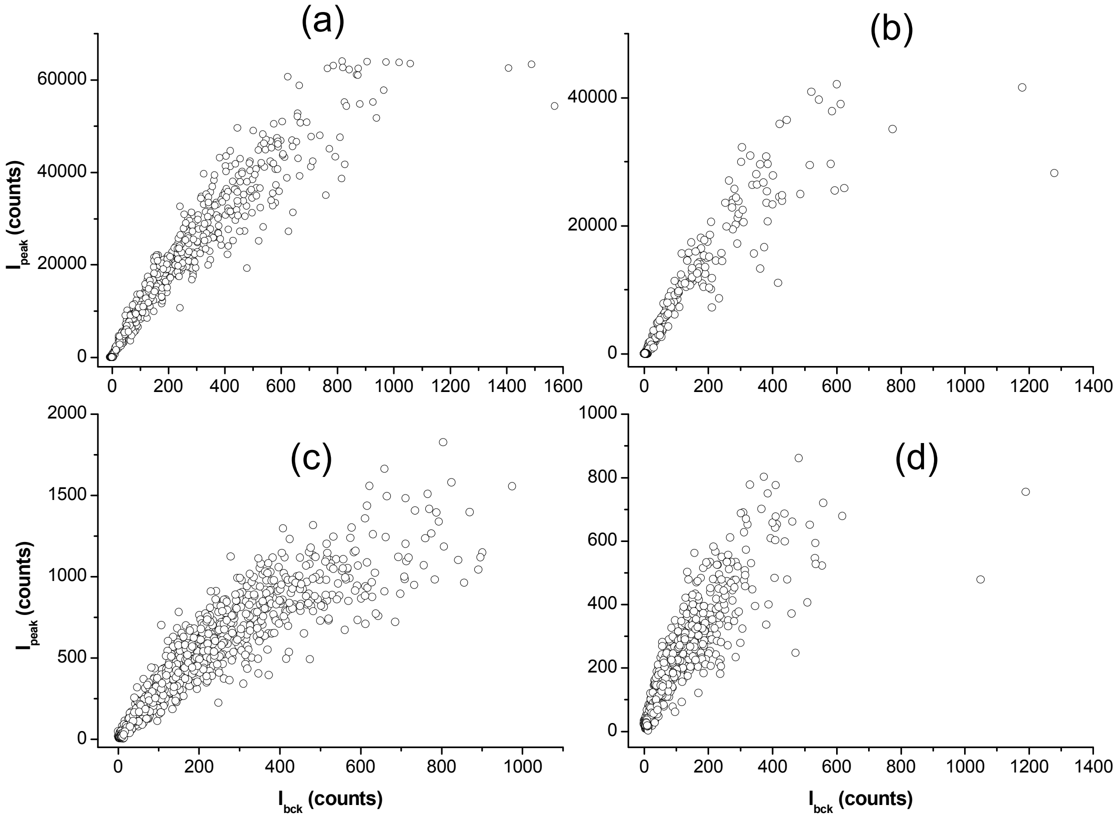

Figure 7.6: Correlation between Mg^+ peak intensity at 279.5 nm and the average nearby background level, for solutions containing Mg in pure water: (a) Mg 500 mg/l, E_1=91 and E_2= 214 mJ; (b) Mg 500 mg/l, E_1=37 and E_2= 156 mJ; (c) Mg 5 mg/l, E_1=91 and E_2= 214 mJ; (d) Mg 5 mg/l, E_1=37 and E_2= 156 mJ.

Calibration was then comparatively performed for the spectra summed over 1000 shots and for the spectra summed after applying the filtering at 50% level of the maximum peak. The data reported in Fig. 7.7 are the average value of six replicate measurements, and the error bars have been calculated for a 95% confidence interval. The measurements for the highest Mg concentration (500 mg/l) have been excluded from the graphs as the curves of growth became non linear. After applying the signal filtering procedure at 50% level (Chapter 5), the LOD defined as three time the noise in the background divided by the slope of the calibration graph, was found to be 0.33 mg/l at low laser energy (resulting in a 7-fold improvement) and 0.21 mg/l at high laser energy (resulting in a 3-fold improvement). In all the examined cases, the correlation factor of the linear fit R is very high. Although the LOD improvement was significant after applying data filtering, there is no clear evidence of an effect in the precision of the measurement.

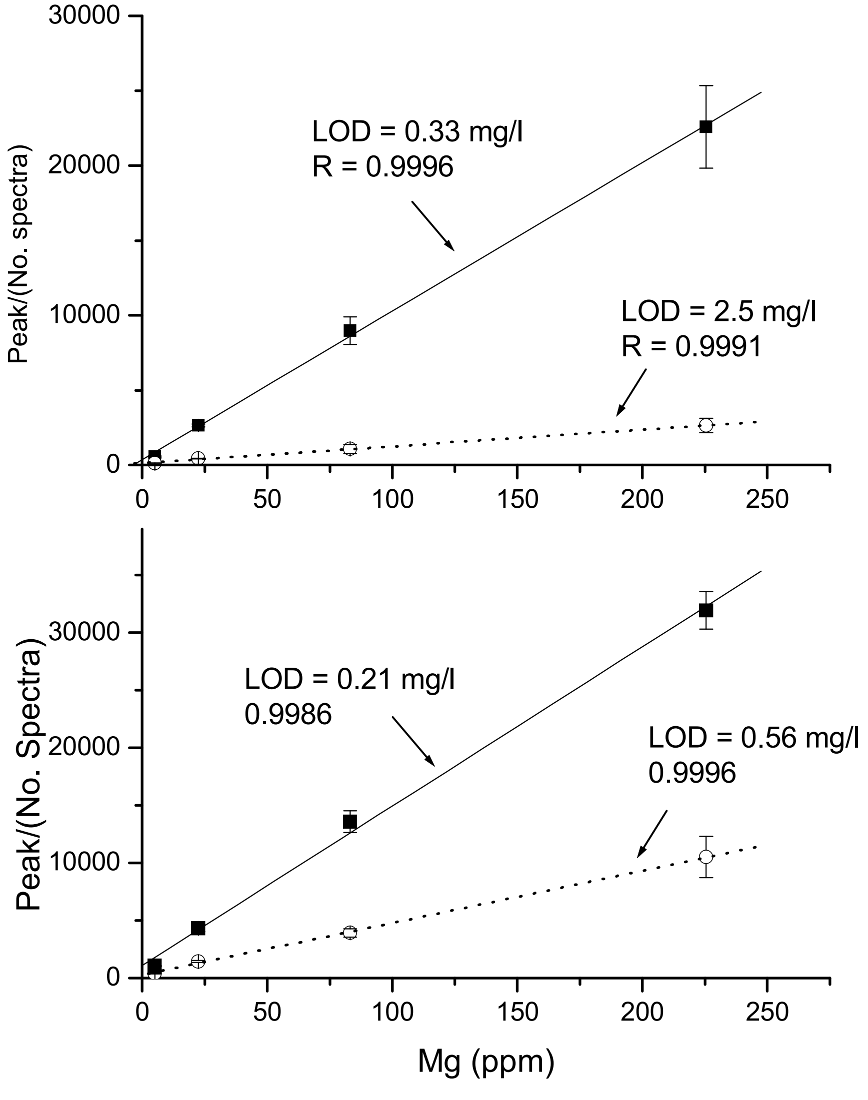

Figure 7.7: Calibration plots for summed spectra without filtering (○) and after applied filtering at 50% level (■), for two sets of laser pulse energies: (a) E_1=37 and E_2= 156 mJ, (b) E_1=91 and E_2= 214 mJ. The peak intensity (Y axis) is normalized on the number of the summed spectra

After the optimization of the laser excitation, as described in the next chapter, the LOD's for the three considered elements result below 1 mg/l (Tab. 7.1). In these conditions the optimal filtering level, applied before the calibration, is at only 10% of the chosen line intensity and this can be explained by more stable plasma position i.e. reduced fluctuations in the plasma intensity inside the observed volume.

With the laser excitation optimized for solutions not containing salts, as described in Chapter 8, the calibration was repeated for waters also containing NaCl. In these cases, due to the plasma elongation, the detection thresholds through the ionic lines are significantly higher (Tab. 7.2). Although the atomic emission increases with water salinity, their lines were not considered for the calibration as for the analyzed elements they are always weaker than the chosen ionic lines. Calibration plots for Mn in pure water and ASW are shown in Fig. 7.8 and they exhibit fast saturation caused by the plasma elongation with adding the impurities to water.

Table 7.1: Element detection limits in pure water for two different conditions of the laser excitation

Element	Wavelength (nm)	E_1=92 mJ E_2=214 mJ	E_1=72 mJ E_2=144 mJ
Mg	279.5	0.210 ppm	0.034 ppm
Mn	257.6	2.450 ppm	0.390 ppm
Cr	283.6	-	0.920 ppm
Notes		t_1=155 μs, Δt=75 μs One pre-pulse	t_1=145 μs, Δt=75 μs Five pre-pulses

Table 7.2: Element detection limits in waters with different grades of salinity for the optimized laser excitation (E_1=72 mJ, E_2=144 mJ)

Element	Wavelength (nm)	PW	ASW30	ASW
Mg	279.5	0.034 ppm	-	-
Mn	257.6	0.39 ppm	0.67 ppm	0.74 ppm
Cr	283.6	0.92 ppm	-	1.96 ppm

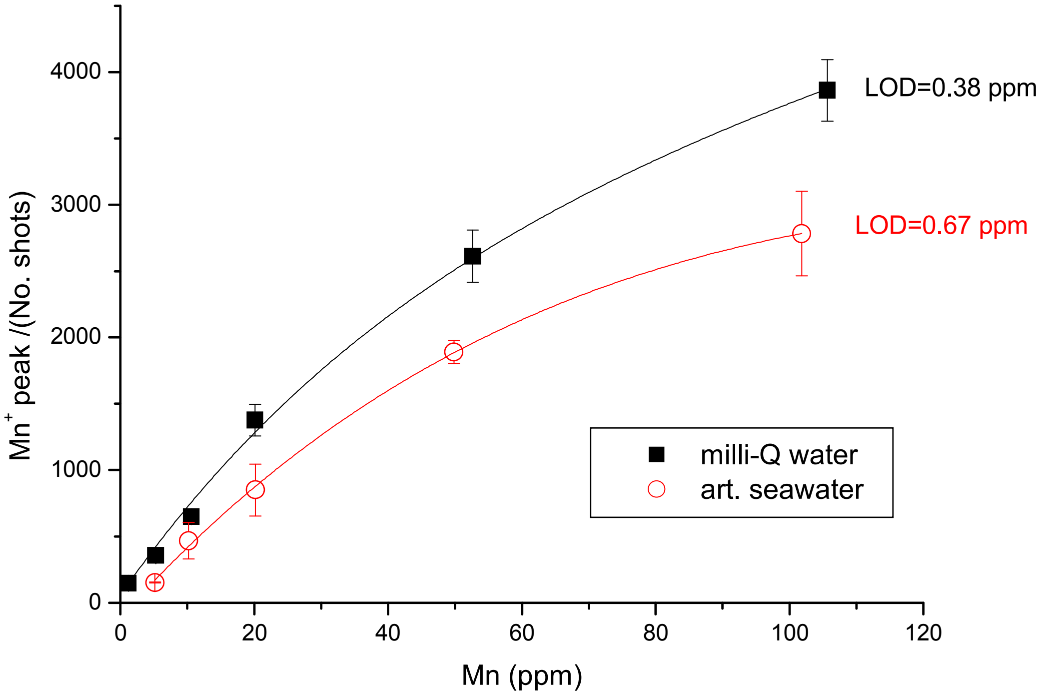

Figure 7.8: Calibration for Mn in pure water and ASW: 1000 shots, filtering at 10%, optimized laser excitation

7.6 Conclusions

Laser plasmas produced in bulk water exhibit strong shot-to-shot intensity oscillations, and sometimes the breakdown events are even missing in the detection region. The statistical intensity distribution may differ from one measurement to another, particularly at higher solution concentrations, such effect being attributed to the probabilistic nature of breakdown in water and the spatial moving of the breakdown location. The plasma extension out of the detection region becomes more pronounced both with an increase of the analyte concentration and presence of other water impurities, including salts. This effect also contributes to a fast saturation of the calibration graphs at higher analyte concentrations. Increasing of the water salinity leads not only to the plasma elongation towards the focusing lens, but also to changes of the plasma parameters, which enhance ratio of the atomic to ionic emission. As a consequence, strong matrix effect must be encountered in LIBS analyses of unknown bulk liquids.

The measured correlation between the line peak emission and the plasma continuum is poor for bulk water excitation, thus negating the use of a normalization procedure based on the background emission.

It was shown that the elimination of low intensity spectra can lower significantly the limit of detection (up to factor 7).

Quantitative LIBS analyses of unknown bulk waters should include a control of the plasma elongation caused by different impurities, and of the plasma parameters. The both factors, particularly affected by water salinity, lead to variable intensity of the analytical lines and potentially, to high analytical errors.

7.7 References

[1] S. Koch, W. Garen, M. Müller, W. Neu, Detection of chromium in liquids by laser induced breakdown spectroscopy (LIBS), Appl. Phys. A 79 (2004) 1071-1073

[2] L. M. Berman, P. J. Wolf, Laser-Induced Breakdown Spectroscopy of liquids: Aqueous Solutions of Nickel and Chlorinated Hydrocarbons, Appl. Spectrosc. 53 (1998) 438-442.

[3] G. Arca, A. Ciucci, V. Palleschi, S. Rastelli, E. Tognoni, Trace element analysis in water by the laser-induced breakdown spectroscopy technique, Appl. Spectrosc. 51 (1997) 1102-1105.

[4] O. Samek, D. C. S. Beddows, J. Kaiser, S. V. Kukhlevsky, M. Liška, H. H. Telle, J. Young, Application of laser-induced breakdown spectroscopy to in situ analysis of liquid samples, Opt. Eng. 39 (2000) 2248–2262.

[5] P. Fichet, P. Mauchien, J. F. Wagner, C. Moulin, Quantitative elemental determination in water and oil by laser induced breakdown spectroscopy, Anal. Chim. Acta, 429 (2001) 269-278.

[6] J. Wachter, D. A. Cremers, Determination of uranium in solution using laser-induced breakdown spectroscopy, Appl. Spectrosc., 41 (1987) 1042-1048.

[7] C. Fabre, M. C. Boiron, J. Dubessy, M. Cathelineau, D. A. Banks, Palaeofluid chemistry of a single event: a bulk and in-situ multi-technique analyses (LIBS, Raman Spectroscopy) of an Alpine fluid (Mont-Blanc), Chem. Geology, 182 (2002) 249-264.

[8] B. Charfi, M. A. Harith, Panoramic laser-induced breakdown spectrometry of water, Spectrochim. Acta Part B, 57 (2002) 1141-1153.

[9] R. Knopp, F. J. Scherbaum, J. I. Kim, Laser induced breakdown spectroscopy (LIBS) as an analytical tool for the detection of metal ions in aqueous solutions, Fresenius J.Anal.Chem., 355 (1996) 16-20.

[10] P. Yaroschyk, R. J. S. Morrison, D. Body, B. L. Chadwick, Quantitative determination of wear metal in engine oils using laser-induced breakdown spectroscopy: a comparison between liquid jets and static liquids, Spectrochim. Acta Part B, 60 (2005) 986-992.

[11] L. St-Onge, E. Kwong, M. Sabsabi, E. B. Vadas, Rapid analysis of liquid formulations containing sodium chloride using laser-induced breakdown spectroscopy, J. of Pharmac. and Biomed. Analysis, 36 (2004) 277–284.

[12] C. W. NG, F. Ho, N. H. Cheung, Spectrochemical analyses of liquids using laser-induced plasma emission: effects of laser wavelength on plasma properties, Appl. Spectrosc., 51 (1997) 976-983.

[13] A. Kuwako, Y. Uchida, K. Maeda, Supersensitive detection of sodium in water with use of dual pulse laser-induced breakdown spectroscopy, Appl. Optics, 42 (2003) 6052-6056.

[14] W. Pearman, J. Scaffidi, S. M. Angel, Dual-pulse laser-induced breakdown spectroscopy in bulk acqueous solution with an orthogonal beam geometry, Appl. Optics, 42 (2003) 6085-6093

[15] D. A. Cremers, L. J. Radziemski, T. R. Loree, Spectrochemical analyses of liquids using the laser spark, Appl. Spectrosc. 38 (1984) 721-729.

[16] N. M. Thang, R. Knopp, H. Geckeis, J. I. Kim, H. P. Beck, Detection of nanocolloids with flow-field flow fractionation and laser-induced breakdown detection, Anal. Chem. 72 (2000) 1-5.

[17] Bundschuh, J-I Yun, R.Knopp, Determination of size, concentration and elemental composition of colloids with laser-induced breakdown detection/spectroscopy (LIBD/S), Fresenius J.Anal.Chem. 371 (2001) 1063-1069.

[18] N. F. Bunkin, A. V. Lobeyev, Influence of dissolved gas on optical breakdown and small-angle scattering of light in liquids, Phys. Letters A 229 (1997) 327-333.

[19] P. K. Kennedy, D. X. Hammer, B. A. Rockwell, Laser-induced breakdown in aqueous media, Prog. Quant. Electr. 21 (1997) 155-248.

[20] V. Lazic, R. Fantoni, F. Colao, A. Santagata, A. Morone, V. Spizzichino, Quantitative laser induced breakdown spectroscopy analysis of ancient marbles and corrections for the variability of plasma parameters and of ablation rate, J. Anal. At. Spectrom. 19 (2004) 429-436.

[21] L. Xu, V. Bulatov, V. V. Gridib, I. Schechter, Absolute Analyses of Particulate Materials by Laser-Induced Breakdown Spectroscopy, Anal. Chem. 69 (1997) 2103-2108.

Chapter 8

OPTIMIZATION OF UNDERWATER PLASMA EXCITATION BY LASER

Abstract

In order to optimize the LIBS signal from bulk waters, laser pulse energies were varied through changing of the QS trigger delays. It was noted that at mid pulse energies the LIBS signal had a tenfold enhancement. In order to explain such a phenomenon the dynamics of the gas bubble generated after the first laser pulse was studied through measurements of the HeNe laser light scattered on the bubble. The influence of laser energy on underwater bubble and plasma formation was observed by photographic technique. An importance of a multi-pulse sequence on the LIBS signal was also analyzed, where the pulse sequence after the first QS aperture was produced by operating the laser close to the lasing threshold.

8.1 Introduction

One of the factors to take into consideration for double pulse LIBS applied on bulk liquids or immersed samples is the timing between the pulses. The maximum LIBS signal can be obtained if the second pulse hits the sample when the gas bubble produced by the first pulse reaches its expansion maximum [1].

Dynamic of the laser generated bubbles in liquids was mainly studied for laser medical applications (ref [2] and therein cited papers) with the aim to avoid an excessive tissue damage, and also in the attempt to obtain efficient tissue ablation or high efficiency of the shock-wave generation (laser lithotripsy). The time evolution and maximum radius of the laser-induced bubble in a certain liquid are strongly dependent on the experimental conditions [2], such as laser wavelength, pulse duration and numerical aperture after the focusing lens.

One of the methods for studying the gas bubble dynamic is laser scattering [3-4]. The laser-induced bubbles have diameter in order of 0.010-1 mm [5] and the scattering of light in the visible can be described by Mie's theory [3, 6].

The final scope of here described research was to improve the sensitivity of LIBS technique applied on bulk liquids, also intended to employ for sub-glacial lake exploration. To this aim, the influence of the laser energy, divided in two or more nanosecond pulses, on underwater plasma emission was studied. Dynamics of the lateral gas bubble expansion after the first laser pulse was measured by light scattering techniques and for different laser pulse energies. Shape of the laser-induced plasma was photographed both by conventional photo camera and by an ICCD, after applying one or two laser pulses.

The LIBS signal intensity after the second laser pulse was also measured and compared to the results obtained by the above mentioned techniques. Influence of low energy multi-pulse laser sequence on the LIBS signal was also considered. For a few representative laser excitation conditions, calibration graphs were generated for solutions containing Mg, Mn or Cr, and the corresponding LOD's were determined. Different experimental aspects, important for the improvement of the LIBS signal intensity are also discussed.

8.2 Experimental

LIBS set-up is the same to that described in sections 4.2 and 5.2.

8.2.1 Scattering measurements

The gas bubble produced by the first laser pulse was illuminated by a 35 mW HeNe laser. The scattered signal was measured at 90° using the same collection optics as for LIBS measurements or at 20° in forward direction where the light was collected with a plano-convex lens (Fig. 8.1). In both cases, the full angle aperture for the scattered light collection was larger than 15° in order to minimize angle dependent signal ripples characteristic for Mie scattering [3-4, 6] .

The signal was brought to a photomultiplier (PMT) by a 6 mm diameter fiber bundle. Between the fiber bundle exit and the PMT, an interferential filter centred at the HeNe laser emission was placed. The PMT used for the present experiment was a Hamamatsu R928. The high voltage power supply feeds a divider designed for high linearity; and the output anode was pre-amplified and AC coupled with a Tektronix 2430A oscilloscope to record light transient. An additional gate circuit was used, which electronically switches off the PMT gain during the time elapsing between consecutive laser shots. Gated operation allowed us to use a CW laser illumination, minimizing problems related with the high mean photon flux incident on the PMT cathode due to light scattering by hydrosols and particles suspended in water. However, this background scattering was always present and the PMT was operated at relatively low voltage (425 V) in order to avoid nonlinearities in its response.

Considering that the laser produced gas bubble might be elongated or that the bubbles might be formed also out of the focal volume, only the lateral expansion of the bubble in the focal point was measured. To this aim, a 1 mm high slit with precisely adjustable vertical position, was placed in proximity to the optical window of the beaker wall. Position of laser generated plasma and consequently the bubble centre might depend on the laser pulse energy [5]. In order to keep the illumination constant across the bubble, a negative lens (f=-50 mm) was placed before the slit, which horizontal width was restricted to 5 mm. The power distribution through the slit, scanned vertically in 3 mm range, was checked by a power-meter and resulted uniform within 5%. This range of the slit positions enclosed fully both the bubble produced by low laser energy pulse (8 mJ) and the one produced at the maximum laser energy (300 mJ, single pulse).

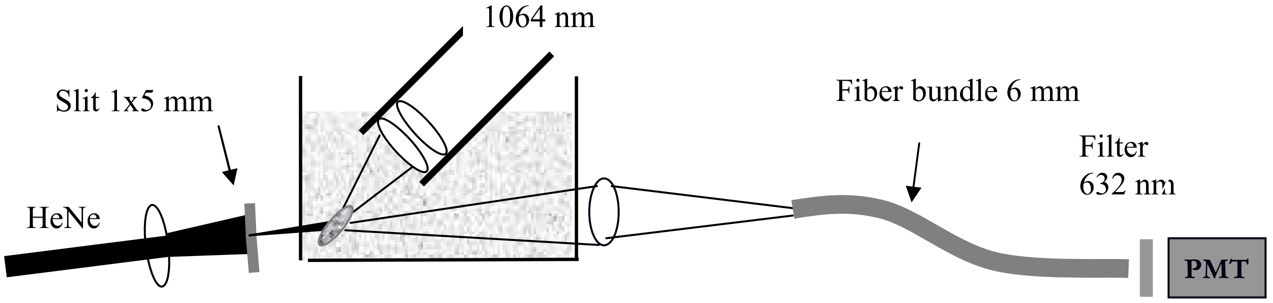

Figure 8.1: Experimental lay-out for forward scattering measurements

8.2.2 Samples

The measurements of the bubble dynamics by scattering technique were performed on tap water, whose standard impurities content was previously determined [7]. In order to avoid disturbances from eventual nanoparticle formation, water in the beaker was exchanged each 30 minutes of the measurements. During water exchange, the focusing lens was always cleaned.

Calibration graphs for quantitative LIBS analyses were generated on reference solutions, adding properly $MgSO_4$, $MnCl_2•7H_2O$ or $Cr(CH_3COH)_3$ to a pure (milli-Q) water (see previous chapter).

8.3 Initial results from LIBS measurements

In order to optimize the LIBS signal, laser pulse energies were varied through changing of the QS trigger delays with respect to the flash-lamp trigger, as discussed in chapter 7. It had been noticed that the reduction of the first pulse energy from 92 mJ to 72 mJ drastically improves the signal, although the second pulse energy was also lowered from 214 mJ to 144 mJ. With lower pulse energies, LOD for Mg in pure water was reduced for one order of magnitude (34 ppb instead of 210 ppb).

One of possible explanation for strong plasma emission enhancement after the second laser pulse with mid first pulse energy could be searched in dynamics of the gas bubble expansion following the first laser pulse. In literature, the reported maximum gas bubble expansions in liquids after a nanosecond laser induced-breakdown are in the range 15-325 μs [5], depending on the laser energy and its wavelength, as well as on the focusing conditions (numerical aperture after the focusing lens). The highest LIBS signal can be obtained when the arrival of the second (probing) laser pulse coincides with the maximum gas bubble radius [1,8]. In order to verify whether the LIBS signal enhancement that we had observed is caused by the maximum bubble expansion for Δt=75 μs at mid first laser pulse energy (72 mJ) the laser scattering measurements were performed.

8.4 Bubble dynamics

For scattering measurements, the plastic baker was initially substituted with one made of glass. However, the strong reduction in the plasma emission was always observed already after 100 laser shots, due to air bubble deposition on the focusing lens. As such an effect was not observed when using plastic beaker, it might be supposed that the electrostatic charges, induced by the shock waves, were forming in presence of large glass surface. For this reason, again the plastic beaker was placed and modified to have an optical window for the HeNe beam entrance.

Dynamics of the laser induced bubble as a function of the laser energy was monitored by settling a single QS trigger (t_1=210 μs) and by changing the current through the flash lamp. This delay corresponds to the stable, highest energy single pulses. With increasing of the laser energy, the produced plasma becomes visibly more elongated. In order to monitor only the lateral bubble expansion, which we consider more important for the LIBS signal after the arrival of the second laser pulse, the HeNe beam was sent through 1 mm high slit, moved with 1 mm step, and scattered signal was measured at different slit positions. At maximum laser energy here used (280 mJ) the signal could be observed for three slit positions (over 3 mm), while up to 170 mJ the signal is existent for only two slit positions. In all the cases, the same slit position gave the signal maximum and corresponding scattered light intensity as a function of time is depicted in Fig. 8.2a. The first, narrow peak, correspond to the laser pulse arrival, which produce the plasma continuum emission also in the spectral range transmitted by the interferential filter. In the same figure (8.2b), the scattering signal obtained without slit is also reported. Here, we could observe that the first bubble collapse occurs between 240 μs and 320 μs, followed by the first rebound. At the maximum energy, also the second and weak third rebounds were detected (Fig. 8.2b).

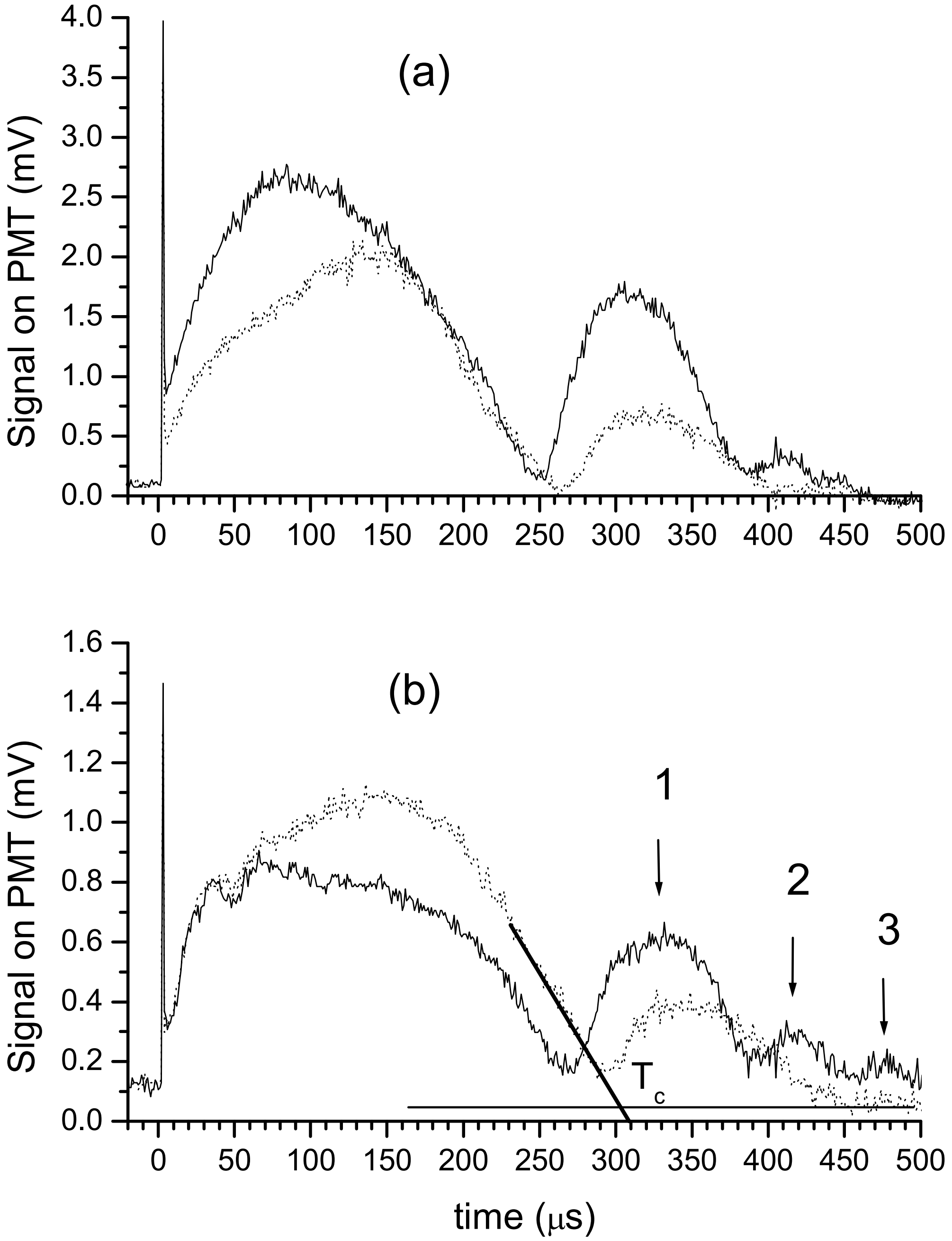

Figure 8.2: Signal from the light scattered at 90° on the gas bubble produced by the laser with pulse energy 65 mJ (dots) and 280 mJ (solid): a) without slit; b) with slit; T_c is the measured first collapse period at lower energy; 1-3 indicate the bubble rebounds at the higher laser energy

The signal shape in presence of the slit is quite different from the one in the absence of the aperture. With the slit, the signal is more symmetrical, and the highest peak, as well as the longest first collapse period, is observed at a relatively low energy, thus indicating largest lateral bubble expansion (eqn. 8.1). In absence of the slit, the peak value is larger for higher laser pulse energies due to the plasma and elongation. It could be assumed that the produced bubble is also elongated, so the scattering from the peripheral bubble volume increments the peak value, or that another bubble is also formed out of the focal point, which also contributes to the signal peak. At high laser energies, also the peak voltage is shifted towards shorter time because the peripheral bubble expansion time is shorter then the central one, as it was confirmed from the measurements with the slit scanned over different positions.

Both for Mie scattering and geometrical optics, the intensity of the light scattered by the spherical bubble of radius R is proportional to R^2 for all scattering angles [6, 9]. Consequently, the gas bubble diameter is proportional to the square root of the PMT voltage V [9]. The maximum bubble radius achieved R_{max} is proportional to the first collapse period T_c through Rayleigh relation [2]:

$$R_{\max} = \frac{T_c}{1.83\sqrt{\rho_0 /(p_0 - p_{v)}}} \tag{8.1}$$

Where ρ_0=998 kg/m^3, p_0 is hydrostatic pressure and p_v is vapour pressure inside the bubble.

The same relationship approximately describes also elongated bubbles, but in this case, R_{max} corresponds to the radius of a sphere having the same volume as the elongated bubble [9].

The first collapse period T_c was determined from the intersection of linearly fitted decaying signal on PMT and the final voltage level (see Fig. 82b) [10]. The scattered signal peak V_{max} and the first collapse period of the bubble as a function of the laser pulse energy, measured with the slit, are shown in Figs. 8.3a-b. In both cases, the maximum lateral bubble expansion corresponds to the laser energy of 65 mJ. Up to this energy, V_{max} value increases approximately linearly. After achieving the maximum, the gas bubble starts to elongate or to form in multiple sites as the breakdown threshold is reached also out of the focal volume. Therefore, a smaller part of the available optical energy is coupled to the mechanical energy (bubble expansion) in the focal point. The measured values of V_{max} and T_c are correlated with factor 0.91. The slightly different behaviour between these two parameters could be observed for the laser pulse energies between 65 mJ and 125 mJ, where probably an elongated bubble or multiple bubbles are formed inside the illuminated section, which corresponds to about 1.5 mm length along the laser axis. The measurements with higher spatial resolution were not possible as the scattered signal becomes too low. On the other hand, further increasing of PMT supply voltage leads to the signal distortion, so it was not applied here. However, there is an evidence of the longitudinal plasma expansion in the illuminated section also from the shape of the scattered signal (Fig. 8.4). For the energy of 45 mJ, the waveform is symmetrical, thus indicating the bubble sphericity. Increasing the energy to 65 mJ, a weak feature at shorter times appear, that could be attributed to another, much weaker micro-plasma (bubble) formed inside the observed volume. Contemporary, the central peak still increased. Further increasing of the laser energy leads to more intense scattered signal at shorter times due to more intense micro-plasma out of focus, and the central peak starts to decrease as discussed above. For laser energies of 170 mJ or higher, two distinct peaks could be observed before the central one, and this can be attributed to another two centres for micro-plasma formation inside the observed volume. These plasmas are weaker then the plasma in focus and the produced bubbles at these centres decay earlier. The central peak is strongly reduced.

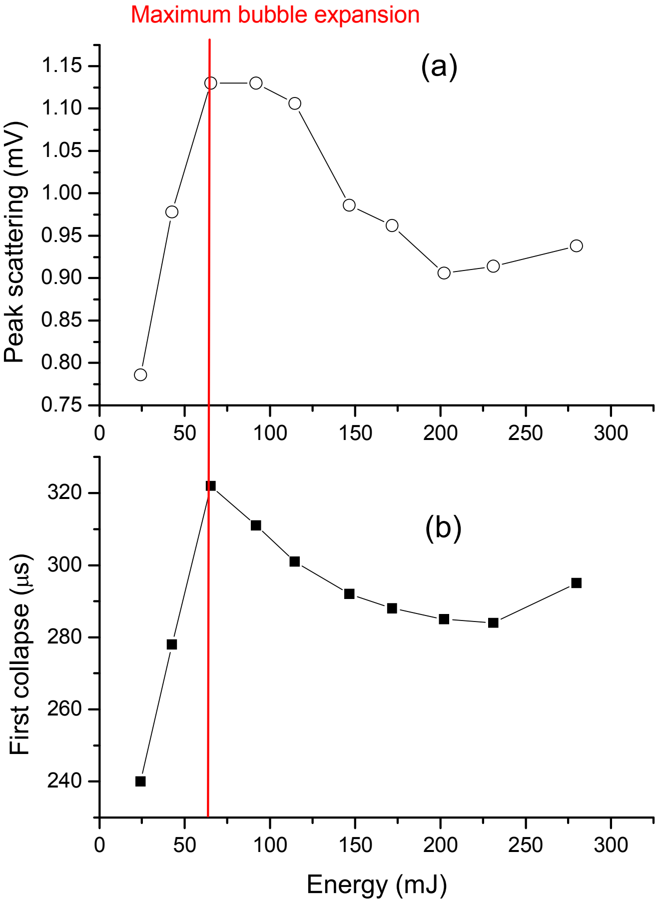

Figure 8.3: Peak of the scattered signal *V* at 90° (a) and the first bubble collapse period T_c (b) as function of the single laser pulse energy; measurements with the slit.

From the results reported in this section, we might conclude that for the present focusing conditions, the optimal energy of the first laser pulse, used to prepare LIBS analyses by the second pulse, is about 65 mJ. Further increase of the first pulse energy leads to the LIBS signal deterioration due to the plasma elongation and reduced lateral bubble expansion. These results are consistent with the higher measured values of LOD's by LIBS when using the maximum laser energy (E_1=92 and E_2= 214 mJ) than when applying E_1=37 and E_2= 156 mJ (see Chapter 7). In the latter case, the first laser pulse produces the bubble of smaller radius (Fig. 8.3a), so the LIBS signal is consequently lower [1]. However, the differences in the lateral bubble expansion between the first laser pulse energies of 72 mJ and 92 mJ are very small - only 3% according to T_c measurements, and from the scattered signal waveforms they could be even neglected for time interval of 75 μs, used for the second pulse arrival. Consequently, the measured differences in the lateral bubble expansions cannot explain the LIBS signal increase for almost one order of magnitude with the applied energy reduction from 92 mJ and 72 mJ.

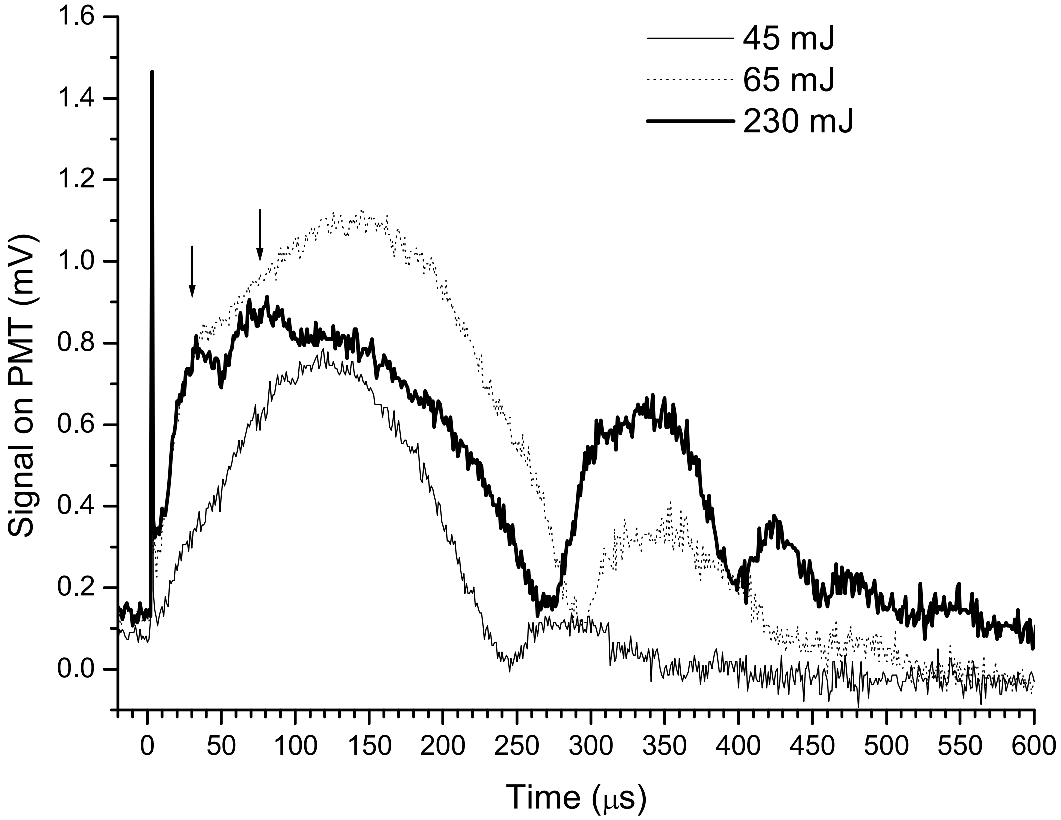

Figure 8.4: Scattered signal measured with the slit as a function of time for three sets of the laser pulse energies; QS delay is t_l=210 μs. Peaks corresponding to the bubbles from new micro-plasma centers inside illuminated volume are indicated by arrows.

In [1] the LIBS signal improvement of about factor 10 was measured when hitting the gas bubble having a diameter two orders of magnitude larger and that is not our case. If we compare the second laser pulse energy in the two discussed cases (144 mJ and 210 mJ), it could be hypothesized that more pronounce plasma elongation at higher energy reduces the amount of the energy transmitted to the focal point, i.e. to the centre of the bubble produced by the first pulse. Unfortunately, by using a DP pulse technique from single laser source, the energies of the two pulses cannot be varied independently, as required for rigorous measurements of the second pulse influence on the LIBS signal. However, from Fig. 8.3 an appreciable difference in the energy coupled to the focal volume cannot be observed when the single pulses with analogue energies are applied. Therefore, the reason for the LIBS signal improvement at lower laser energies was further investigated through characterization of the laser pulse form and by photographing the plasma shape.

8.5 Laser pulse and plasma shape

Previously, the laser pulse energies in DP excitation were measured by an energy-meter, applying one or two QS triggers. The energies of the pulses were varied by changing the QS trigger delays, where longer first pulse delays correspond to its higher energy and consequently to lower energy of the following pulse. Observing the laser pulse shape by a fast photodiode, it was noticed that for shorter first QS delays with respect to the flash lamp trigger, the relaxation oscillations occur resulting in a multi-pulse sequence (Fig. 8.5). For t_1=145 μs or shorter, five pulses are present, whose energies are tending to equalize with reducing of the QS delay.

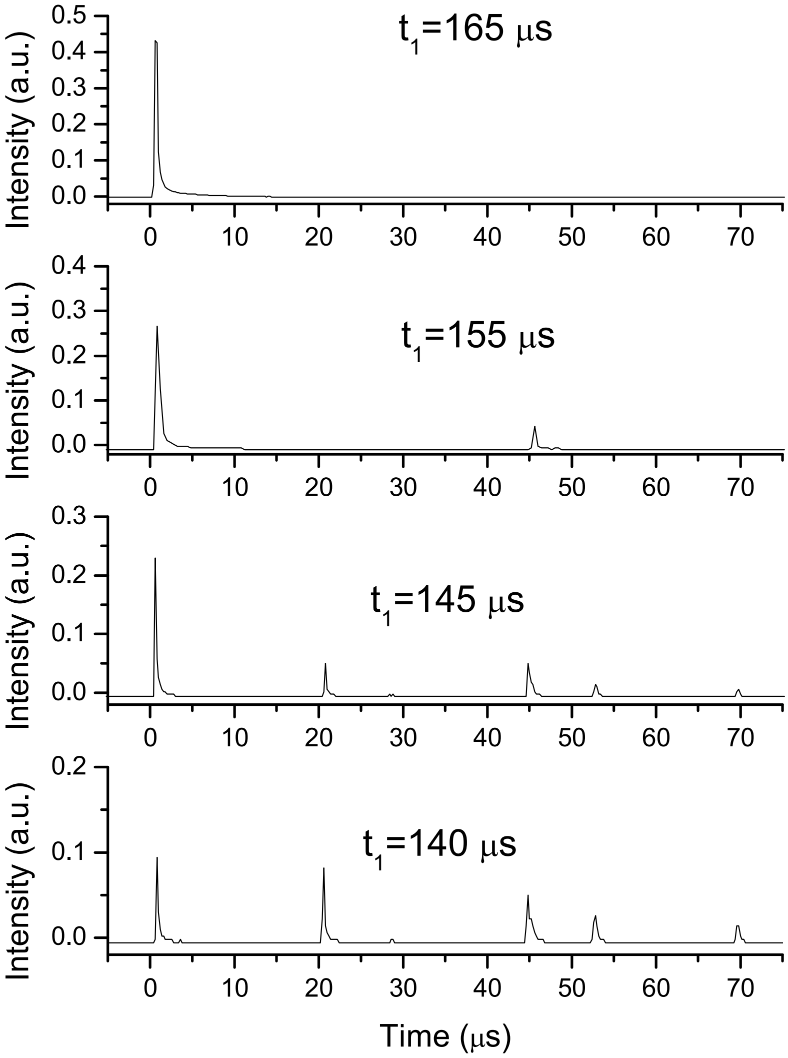

Figure 8.5: Shape of the first laser pulse, detected by a fast photo-diode, for different delays of the QS trigger with respect to the flash-lamp trigger.

Now, it seems clear that lowering laser pulse energies a better LIBS signal was obtained due to multi-pulse excitation. In the first measurements, the first pulse had energy of 92 mJ obtained for t_l=155 μs, so in presence only of a weak secondary pre-pulse, delayed for about 45 μs from the first one. Its energy was estimated to about 13% of the total pre-pulse energy, so the first pre-pulse had about 80 mJ. In the second experiment, 5 pre-pulses were present with total energy of 72 mJ and the corresponding first pre-pulse energy was about 50 mJ. The last pre-pulse occurs after about 70 μs from the first one, so 5 μs before the probing (second pulse). However, it should be clarified if the observed LIBS signal improvement in the second case was due to:

a) Larger lateral plasma expansion in presence of the multi-pulse sequence

b) More localized breakdown (less elongated plasma) and the gas bubble formation

c) Short interval between the last pre-pulse and the probing pulse

The lateral bubble expansion after the first laser pulse sequence was then compared for the two settings from above and for single pulse (t_l=210 μs) with the same energy as the pulse sequence (Fig. 8.6). Both from the scattered signal intensity and the first collapse period, the lateral bubble expansion results smaller for the lower energy setting (t_l=145 μs, E_1=72 mJ) than for the higher one (t_l=155 μs, E_1=92 mJ). In the first case, the intermediate pulse occurring about 50 μs from the first one clearly increases the slope of the bubble expansion. For the interval used for the second laser pulse arrival (Δt=75 μs) the scattered light intensity approximately reaches that one obtained at higher energy setting. In the latter case, a portion of the scattered signal for this timing also comes from the bubble(s) formed out of the focus, as discussed earlier. We might conclude that the splitting of the pulse into sequence of the pulses with the same total energy does not improve, or at least – not significantly, the lateral bubble expansion in the cases here examined. Consequently, the gas bubble dynamics is not responsible for the detected LIBS signal improvement with lowering of the laser pulse energies.

Observing photographs of the underwater plasma, taken with simple digital camera in the presence also of the second laser pulse, we may note that increasing the first laser pulse (or pulse sequence) energy, the secondary plasma changes shape from the spherical to elliptical (Figs. 8.7a-b). Further increase of the first pulse energy leads to clear formation of the secondary plasma in multiple sites (Fig. 8.7c).

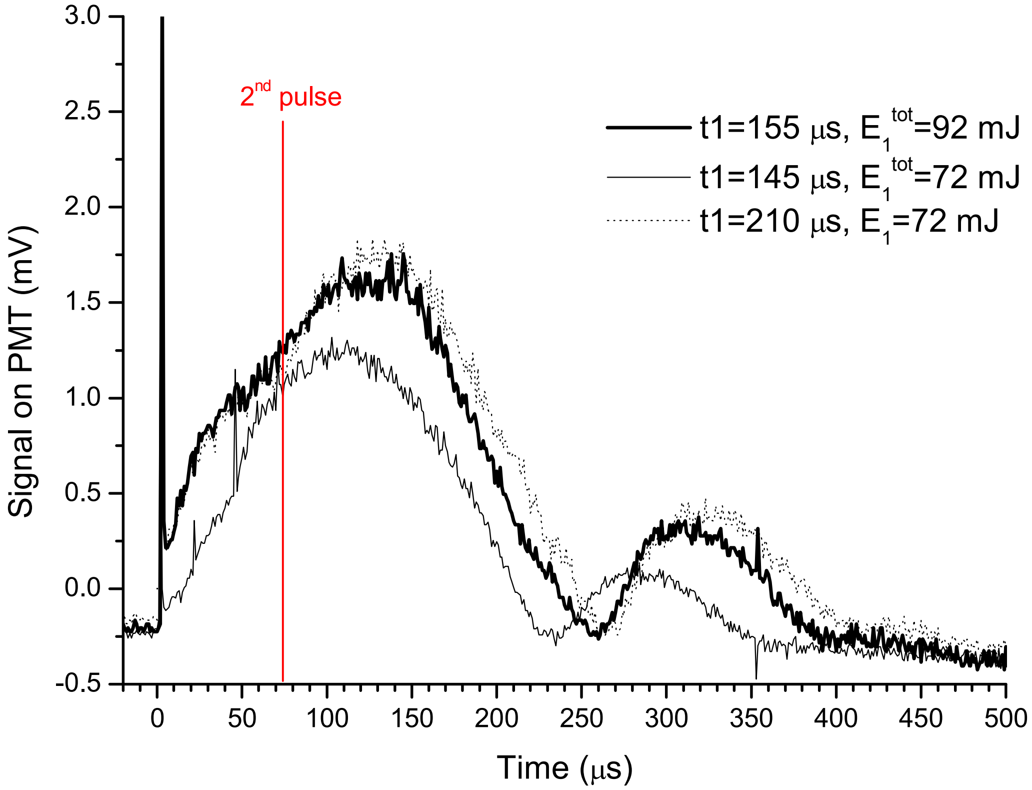

Figure 8.6: Scattered signal after the first laser pulse sequence for two settings used in LIBS measurements, and comparative signal measured in presence of single pulse (t_1=210 μs) with equivalent energy.

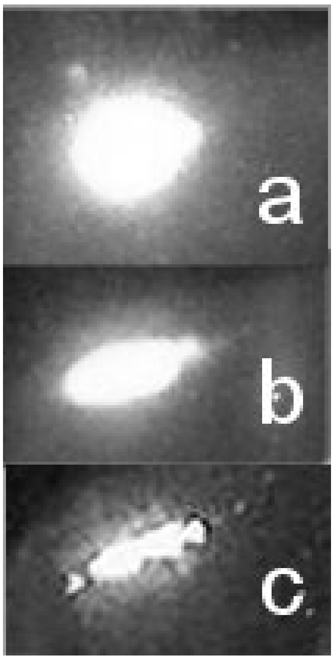

Figure 8.7: Plasma shape photographed by a digital camera (laser from the right): a) t_1=145 μs, Δt=80 μs, 5 pre-pulses, E_1^{Tot}=72 mJ, E_2=140 mJ; b) t_1=155 μs, Δt=80 μs, 2 pre-pulses; E_1^{Tot}=110 mJ, E_2=123 mJ; c) t_1=165 μs, Δt=80 μs, 1 pre-pulse, E_1=181 mJ, E_2=57 mJ

Presence of multiple plasma sites after the second pulse was also photographed by the ICCD camera, triggered contemporary with the second laser pulse and using acquisition gate of 10 μs. In Fig. 8.8a the secondary plasma produced after low energy multi-pulse sequence followed by the energetic pulse, has a spherical shape with a relatively high intensity. Increasing the pre-pulse energy closely spaced spherical plasmas are produced (Fig. 8.8b) after the second shot, but they loose in intensity and in volume. Further increase of the pre-pulse energy causes multi-bubble formation along the laser path at large distances from the focal point. Then, after the second (probing) pulse, the distance between new formed plasma sites might increase (Fig. 8.8c) and intensity of the plasma formed farther from the focusing lens is consequently reduced. An excessive energy of the first pulse causes not only the strong plasma elongation but also its shift towards the focusing lens (Fig. 8.8d). The secondary plasmas are again formed in multiple sites but they are no more symmetrical and have weak intensities.

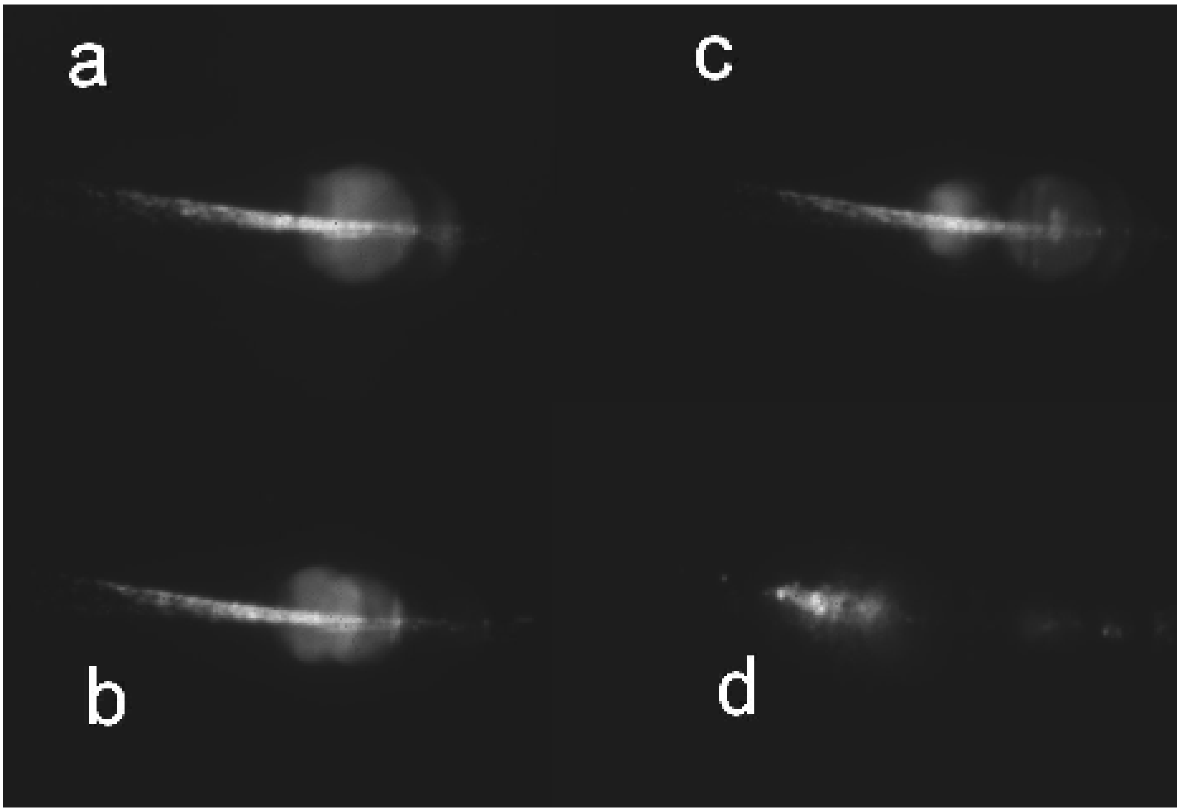

Figure 8.8: Plasma images taken by the ICCD after the second laser pulse, with integration time 10 μs. The energy of the first laser pulse (multi-pulse) is progressively increased from (a) to (d). Data for the pulse energies are not available.

8.6 Role of the timing between the laser pulses

If we look the LIBS signal and laser pulse energy, measured as a function of the interpulse delay (Fig. 8.9), the steep increase of the LIBS signal accumulated over 200 laser shots, is caused by the laser pulse instabilities present for Δt<68 μs. Above this value of interpulse delay, initially both the line and plasma continuum emission follow the energy oscillations caused by the current switching through the flash lamp (period about 8 μs). However, increasing the interpulse delay, and in this way also the interval from the last pre-pulse, the plasma emission decreases faster than the second pulse energy although the bubble radius before the second pulse arrival still increases (Fig. 8.6). The latter should lead to the LIBS signal improvements [1]. This indicates that a relatively short timing between the last pre-pulse and the second laser pulse might be a reason for an additional LIBS signal enhancement.

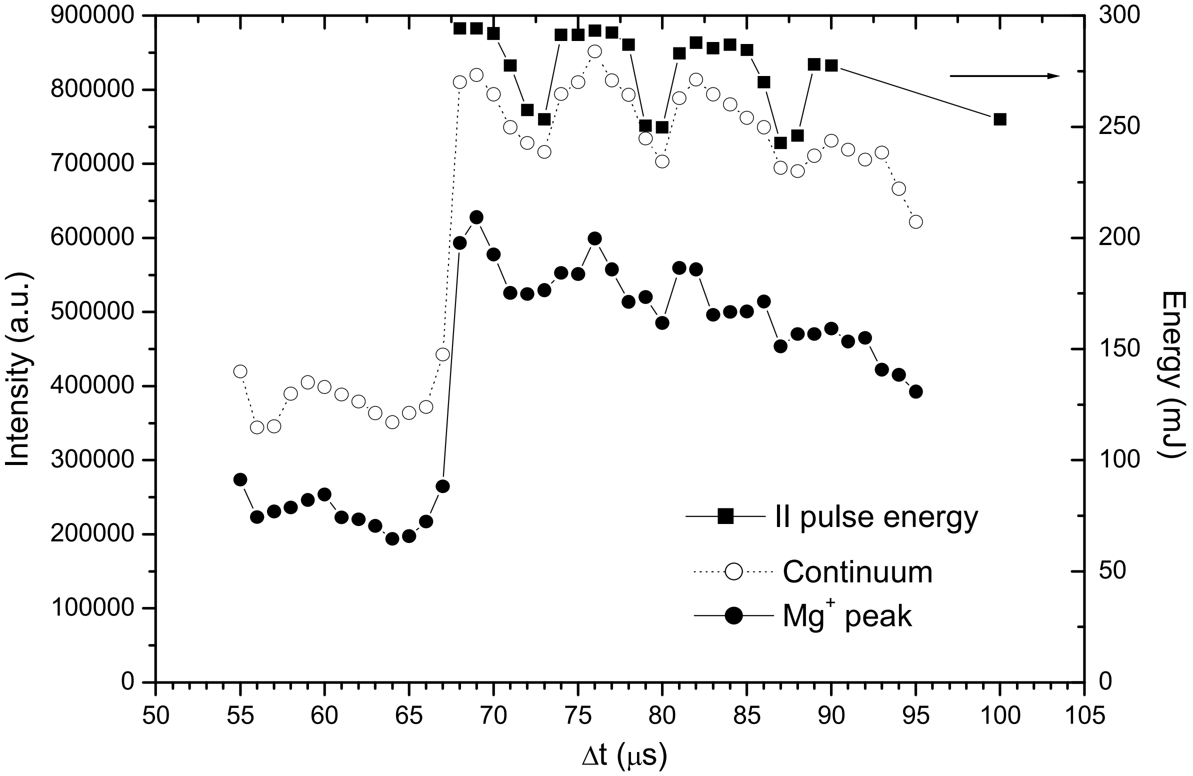

Figure 8.9: Plasma continuum and Mg^+ (279 nm) peak emission multiplied 2x (left), and second laser pulse energy (right) a function of the interpulse delay. The first QS trigger delay is t_1=145 μs.

In a pioneering work relative to DP LIBS underwater [11], two Nd:YAG lasers at 1064 nm were used with similar energies (E_1=30-76 mJ, E_2=125 mJ) and in analogue focusing conditions as in here discussed experiment. The measured LIBS signal as a function of interpulse delay had a maximum for Δt=18 μs and this can not be attributed to the maximum bubble expansion caused by the first laser pulse, which generally occurs after more than 100 μs (in our measurements – after 120-160 μs). For interpulse delay in order of 100 μs, the measured signal was more than 6 times lower with respect to the optimal delay (Δt=18 μs). Also in a recent publication [1], the LIBS signal intensity obtained after the second laser pulse when using two laser sources at 532 nm, does not follow the gas bubble radius for small interpulse delays, but starts to increase with shortening Δt bellow 40 μs (Fig. 3. 4). All this indicates that a relatively short timing between two pulses, in the present case obtained by a sequence of the pre-pulses, may be another reason for observed plasma emission enhancement after lowering the laser pulse energies.

In here discussed experiment, using single laser source, it was not possible to vary the interpulse delay independently from the laser energy. However, by reducing the current through the flash lamp for the first QS trigger delay t_1=155 μs, where a weak secondary pre-pulse is present, and helped by the laser energy oscillations due the current switching, for Δt=73 μs, it was possible to find the same set of the total pre-pulse and the probing pulse energies as in the case of t_1=145 μs, Δt=74 μs. In the latter case, much stronger LIBS signal (Fig. 8.10) could be attributed only to the presence of multi-pulse sequence shown in Fig. 8.5 as the differences in the bubble expansion could be neglected in correspondence of the probing pulse arrival (Fig. 8.6). Moreover, Figure 8.10 shows an increased continuum emission, thus indicating LIBS plasma having a density higher than that observed in case of a simple DP excitation. It could be hypothesized that the observed, almost tenfold increase of SNR (Fig. 8.10a) is due to increased absorption coefficient of the vapour bubble after the laser excitation by the last pre-pulse, i.e. in a presence of the plasma inside the bubble. Consequently, it could be deduced that in presence of a pre-pulse sufficiently close to the probing one (here the distance between the last pre-pulse and the probing one was about 5 μs) maintains the plasma inside the bubble. Then, the last laser pulse is coupled better with the bubble and a much stronger plasma emission i.e. LIBS signal, is so obtained.

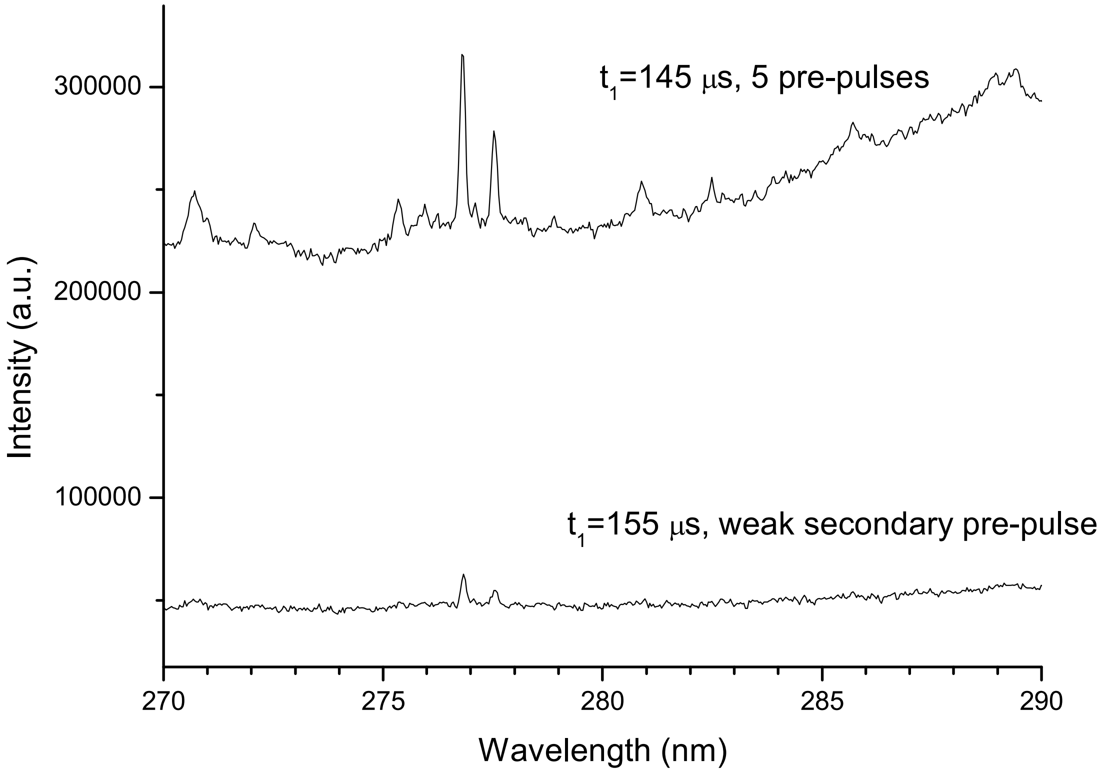

Figure 8.10: LIBS signal accumulated over 100 shots for gate delay zero from the probing pulse and gate width 10 μs. The pre-pulse and the second pulse energies are equal (E_1=72 mJ, E_2=128 mJ) in both cases (t_1=145 μs and t_1=155 μs). Mg concentration is about 5 ppm in tap water.

8.7 Conclusions

In this chapter, the causes for a tenfold LIBS signal improvement underwater, obtained by lowering the laser pulse energies, were examined. These studies were performed by analyzing LIBS signals, laser pulse energies and shapes, then by applying scattering measurements to study the gas bubble dynamics and by taking photographs of the plasma.

Laser produced plasma underwater exhibits elongation above a certain energy threshold, which in this experiment was at about 65 mJ. This energy also represents a limiting value for the maximum lateral gas bubble expansion. Above this limit, the plasma is elongated and generates the gas bubbles in multiple sites and with smaller radius. Hitting the laser bubble with an appropriately timed second laser pulse produces a relatively strong LIBS signal. This signal is maximal if the primary plasma (i.e. the gas bubble) was produced in a single site and with the laser energy corresponding to the maximum lateral bubble expansion. In such case, the secondary plasma formed on the seeding bubble, is strongly symmetric and intense. Further increase of the first laser pulse energy leads to the formation of spherical secondary plasmas in multiple sites, seeded on the previously formed bubbles, as observed by the fast photography technique.

The overall secondary plasma emission is then reduced as the plasma formed closer to the focusing lens partially absorb the second laser pulse, thus reducing the optical coupling to the largest bubble present in the focal point. Excessive first laser pulse energy leads to an intense breakdown before the focal point and to a number of very small bubbles, so the second laser pulse cannot be coupled in proximity of the focal point both due to the light absorption and to scattering by the bubbles formed closer to the focusing lens. The resulting secondary micro-plasmas are very weak and asymmetrical and the LIBS signal is very weak or even absent.

Besides keeping the first laser pulse energy close to the plasma elongation limit, an appropriate splitting of the first laser pulse into multi-pulse sequence, here obtained by inducing the relaxation oscillations after the first QS aperture, could further improve the LIBS signal. The first, most intense pulse of the sequence produces well-localized gas bubble, which radius is further expanded by the successive pulses of the sequence. In this way, still keeping the bubble expansion high, the plasma elongation is avoided and the second pulse is well coupled in the focal point.

It was also demonstrated that a relatively short timing between the last pulse of the sequence and the second, probing pulse, also contributes to a manifold enhancement of the secondary plasma emission. As an analogue experimental observation had been reported previously [11], it could be hypothesized that some kind of resonant laser absorption by an excited bubble appears shortly after the laser pulse arrival. The enhanced laser absorption by a small pre-pulse might have also in optical switching and in intraocular surgery where it is important to prevent damage of retina.

For optimized laser excitation by low-energy multi-pulses, the LIBS detection limits for bulk liquids are lowered up to one order of magnitude, thus obtaining 034 ppm for Mg, 0.38 ppm for Mn and 0.92 ppm for Cr. These detection limits could be further improved by using two separate laser sources, the first one operating in a multi-pulse regime, in order to hit the gas bubble by the second laser when it reaches the expansion maximum. The latter occurs at (120-160) μs from the first pulse according to here performed scattering measurements.

Strong improvement of underwater LIBS signal by limiting the laser pulse energies has also an importance in the system miniaturization in view of real in-situ analyses.

Further research should address the influence of the second laser pulse energy on the LIBS signal by employing of two independent laser sources. Studies of the increased, resonant-like laser absorption by weak plasma inside the gas bubble, here excited by low energy intermediate pulses, should be also performed.

8.8 References

[1] A. Casavola, A. De Giacomo, M. Dell'Aglio, F. Taccagna, G. Colonna, O. De Pascale, S. Longo, Experimental investigation an modeling of double pulse laser induced plasma spectroscopy under water, Spectrochim. Acta Part B, 60 (2005) 975-985.

[2] A. Vogel, J. Noack, K. Nahen, D. Theisen, S. Busch, U. Parlitz, D. X. Hammer, G. D. Noojin, B. A. Rockwell, R. Birngruber, Energy balance of optical breakdown in water at nanosecond to femtosecond time scales, Appl. Phys. B, 68 (1999) 271-280.

[3] R. G. Holt, L. A. Crum, Mie scattering used to determine spherical bubble oscillations, Appl. Optics 29 (1990) 4182-4191.

[4] W. J. Lentz, A. A. Atcheley, D. F. Gaitan, Mie scattering from a sonoluminescing ait bubble in water, Appl. Opt., 34 (1995) 2648-2654.

[5] P. K. Kennedy, D. X. Hammer, B. A. Rockwell, Laser-induced breakdown in aqueous media, Prog. Quant. Electr. 21, (1997) 155-248.

[6] M. Kerker, The scattering of light and other electromagnetic radiation, Academic (1969), New York.

[7] A. De Giacomo, M. Dell'Aglio, F. Colao, R. Fantoni, V. Lazic. Double-Pulse LIBS in water bulk and on submerged bronze samples, Appl. Surf. Sci., 247 (2005) 157-162.

[8] A. De Giacomo, M. Dell'Aglio, O. De Pascale, M. Capitelli, From single pulse to double pulse ns-Laser Induced Breakdown Spectroscopy under water: elemental analysis of aqueous solutions and submerged solid samples, Spectrochimica Acta Part B 62 (2007) 721-738.

[9] B. P. Barber, S. J. Putterman, Light scattering measurements of repetitive supersonic implosion of a sonoluminescing bubble, Phys. Rev. Letters, 69 (1992) 3839-3842.

[10] P. Hubert, K. Jöchle, J. Debus, Influence of shock wave pressure amplitude and pulse repetition frequency on the lifespan, size and number of transient cavities in the field of an electromagnetic lithotripter, Phys. Med. Biol. 43 (1998) 3113-3128.

[11] D. A. Cremers, L. J. Radziemski, T. R. Loree, Spectrochemical analyses of liquids using the laser spark, Appl. Spectrosc., 38 (1984) 721-729.

Summary

In this dissertation, double-pulse laser excitation (at 1064 nm, pulse duration 8 ns) was applied for LIBS analyses of different solid materials immersed in seawater. The materials analyzed correspond to those that can be found in marine archaeological parks, in view of LIBS application for in-situ recognition of materials/objects valuable for extraction or in-situ restoring. Here obtained results demonstrate that both precious alloys and copper-based alloys, such as bronzes, can be clearly identified by LIBS and distinguished from other common materials such as iron, the latter tested also in highly oxidized state. On the submerged bronze samples, also quantitative analysis were obtained, allowing for the approximate object dating as the composition of these alloys varied along the manufacturing age. Furthermore, it was possible to distinguish by LIBS marble materials from not valuable, common calcareous rocks.

In order to improve LIBS signal from inhomogeneous and rough sample surfaces, as they can be found in nature, a procedure for multi-shot signal acquisition and processing was developed, here called spectral filtering. This procedure allowed to increase Signal-to-Noise Ratio up to a factor 4 on the immersed solids, and thus to extend a range of the detectable elements from the samples. The studied modality of the LIBS signal detection has also importance in application in other surroundings (gas, vacuum) whenever there is a source of important shot-to-shot signal variations such as the sample in-homogeneity and roughness, then development of a crater, or not controllable aerosol formation above the sample surface.

In following, LIBS was applied for analyses of immersed sediments, and this represents a pioneering work on underwater LIBS analyses of soft materials. In such a case, the laser-induced shock waves creates a more or less dense particle cloud above the analyzed soft material, which scatter the incoming laser and outgoing plasma radiation, and sometimes induce the breakdown formation above the analyzed surface. By applying the above mentioned procedure for the spectral filtering, it was possible to detect also some trace elements from the sediments. However, due to strong shot-to-shot variations of the plasma location and properties, quantitative analyses were obtained only after developing an additional data filtering procedure. The latter regards automatic selection and summing only the spectra with similar plasma properties, identified through spectral distribution of the plasma continuum. An importance of this work is related to a possibility to measure in-situ the composition of top sediment layers, interesting for sub-glacial lake exploration and pollution detection of sea or river bottoms.

The last step in underwater LIBS analyses regards liquid impurities, where three elements were considered: Mg, Mn and Cr. The first elements is normally present in waters, the second one is also related to a bio-productivity in waters, while Cr is related to pollution. Initially, the detection limit

for Mg in pure water when applying the low laser energy set, was of 2.5 ppm and this one was reduced for about 7 times (to 0.33 ppm) after applying the previously mentioned spectral filtering. At the highest laser pulse energies used, the same filtering procedure improves the sensibility for about factor 3, allowing detecting Mg down to 0.21 ppm. However, in the successive experiment, it was observed beyond the expectations, that for mid laser pulse energies a tenfold reduction of the LIBS detection limits occurs, corresponding to 33 ppb for Mg, 390 ppb for Mn and 920 ppb for Cr. Here, the first trigger delay was reduced with respect to the first measurements. The influence of the matrix effect, i.e. liquid impurities and water salinity on the LIBS signal was also studied. It was found that any solute addition to pure water progressively elongates the plasma and this effect causes the reduction of the laser radiation coupled to the focal point. As a consequence, calibration curves show fast saturation with the solute concentration and the detection limits increase with the water salinity.

In the final part of this dissertation, the reasons for the LIBS signal improvement at mid laser pulse energies were investigated. The underwater plasma and bubble formation was studied by Mie scattering on laser-induced bubbles, by a fast and conventional photography, as well as from the spectral (LIBS) analyses. Contemporary, the pulse energies and shape were always monitored and it was observed that at low first pulse energies, obtained by reducing delay of the first Q-switch trigger, a multi-pulse sequence was present. The most important here obtained results can be summarized in the following: efficient; localized plasma and gas bubble formation in water (and other liquids) has an upper laser energy limit; higher energy pulses lead to the plasma elongation and formation of multiple spherical bubbles along the beam path, which scatter the incoming radiation from the successive laser pulse; by using a sequence of low-energy multi-pulses before the last laser pulse, both the plasma and gas bubble remain well localized and the bubble highly expanded; presence of a small pulse before the last one (analytical pulse for LIBS) is responsible for a tenfold increase in its coupling to the bubble, thus to an extremely intense secondary plasma emission.

In all the experimentations here reported, a single laser source was used by applying two external Q-Switch triggers to produce two laser pulses during a single lamp flashing. Multi-pulse sequence was obtained by reducing the first Q-Switch trigger delay to operate close to the population inversion where the relaxation oscillations occur. These oscillations are transformed into a pulse sequence through a piezovoltaic effect of the KDP* crystal employed in the Q-Switch, where periodically incomplete closing appears.

List of figures

List of tables

Acronyms

ASW	Artificial SeaWater
ASW30	Mixture 30% of ASW and 70% of pure water
CCD	Charge Coupled Device
CF	Calibration Free method
DLS	Distance Lens to Sample
DP	Double Pulse
HR	High Resolution
ICCD	Intensified CCD
LIB	Laser Induced Breakdown
LIBS	Laser Induced Breakdown Spectroscopy
LOD	Limit Of Detection
LR	Low Resolution
LTE	Local Thermal Equilibrium
PDA	PhotoDiode Array
PMT	Photomultiplier
PW	Pure milli-Q Water
QS	Q-Switch
RSD	Relative Standard Deviation
SD	Standard Deviation
SNR	Signal-to-Noise Ratio
SP	Single Pulse

Acknowledgments

I am grateful to my supervisor, Prof. Maria Richetta and to Prof. Carlo Belecci from University Tor Vergata (Rome) for all the support given.

Responsible of FIS-LAS department at ENEA, Roberta Fantoni, is gratefully acknowledged for involvement in all my works relative to LIBS, and for conceding me a large autonomy in here presented research.

Special thank are addressed to my colleague and great friend, Sonja Jovicevic from Institute of Physics, Belgrade (Serbia) for deep involvement in the later works presented in this dissertation, including the most useful scientific discussions.

I thank Prof. Alessandro de Giacomo from University of Bari for important discussions relative to underwater laser-induced plasma, and to Milivoje Ivkovic from Institute of Physics, Belgrade (Serbia) for the suggested corrections relative to the first chapters of this dissertation.

I am grateful to my other colleagues from ENEA Frascati, especially to:

- Valeria Spizzicchino (ENEA fellowship) for participation in most of the experiments here reported
- Francesco Colao, who performed the fast plasma photography and supplied his assistance with the laboratory equipment
- Antonio Palucci, Roberto Giovagnoli, Luca Fiorani, Luigi De Dominicis and Antonella Lai, who on different ways, helped my work

The research relative to underwater material recognition has been conducted within the project TECSIS (Diagnostic TEChnologies and Intelligent Systems for the development of archaeological parks in Southern Italy), funded by Italian Ministry for Education, University and Research (MIUR).

Other here presented researches have been also funded by MIUR through the projects MIAO (sensor microsystems for application in hostile environments), and PANDORA (sub-glacial lakes exploration). The latter project belongs to the Technology Sector of PNRA (Italian National Program of Researches in Antarctica).